1992

# Determination of secondary sources in noise cancellation with boundary element method

Guang-Hann Chen
*Iowa State University*

Order Number 9234798

# Determination of secondary sources in noise cancellation with boundary element method

Chen, Guang-Hann, Ph.D.

Iowa State University, 1992

U·M·I
300 N. Zeeb Rd.
Ann Arbor, MI 48106

# Determination of secondary sources in noise cancellation with boundary element method

by

Guang-Hann Chen

A Dissertation Submitted to the

Graduate Faculty in Partial Fulfillment of the

Requirements for the Degree of

DOCTOR OF PHILOSOPHY

Department: Aerospace Engineering and Engineering Mechanics
Major: Engineering Mechanics

Approved:

Signature was redacted for privacy.

In Charge of Major Work

Signature was redacted for privacy.

For the Major Department

Signature was redacted for privacy.

For the Graduate College

Iowa State University
Ames, Iowa
1992

# TABLE OF CONTENTS

# LIST OF TABLES

## LIST OF FIGURES

# ACKNOWLEDGMENTS

I would like to express my sincere gratitude to Dr. Anna L. Pate and Dr. Ambar K. Mitra for their constant help during this research. They were always on hand when I needed help. Without their assistance, this work would not have been accomplished.

Special thanks are for Dr. Frank Rizzo for allowing me to modify his computer programs when I needed to. Extended thanks are also to Dr. David K. Holger, Dr. Jerry L. Hall and Dr. Jennifer Davidson for their encouragement and support.

I would also like to thank my wife and my parents for their constant support.

# 1. INTRODUCTION

## 1.1 Overview

Noise cancellation is often an important subject in acoustics. Generally speaking, there are two types of noise cancellation, namely, active and passive. The research described in this thesis deals with active noise control which cancels the acoustic sound wave produced by an arbitrary noise source. This is achieved through the addition of an inverted sound wave from well-controlled sources. The acoustic pressure being a scalar quantity, the acoustic sound wave can be destructively interfered by another properly controlled sound wave. Although active noise control is conceptually easy, its application is difficult to implement, because it requires exact match of acoustic sound waves at every point along the propagation path. Since, the acoustic pressure is a function of time and spatial location, the generation of the proper destructive sound wave at the proper location and at the right time becomes the main task in active noise control.

The theory of active noise control has long been understood. However, it was not formally applied until Lueg [1] filed a patent in 1933. Young stated that an acoustical propagation wave could be canceled by the addition of an inverse wave. Huygen [2] extended the concept to a wider area of noise reduction. Huygen claimed that the sound field inside a closed domain produced by a sound source outside the domain

could be inverted exactly by a properly distributed array of secondary sources over the surface of the domain. This principle has a great advantage in that the sound field inside the domain of interest can be reduced, regardless of the type of sound wave generated by the noise source outside the domain. In spite of the theoretical progress mentioned above, the implementation of active noise control was rather slow, because Huygen's principle suffered from the requirement of an infinite number of perfect point sources distributed along the boundary of the Huygen's surface. It was not until the 1980s that active noise control became more practical. The recent advancement in digital computers improved sound measurement techniques, fast Fourier transform, data acquisition, and processing systems. Such developments provided useful tools for active noise control. Consequently, more practical models and better noise cancellation techniques in the field of active noise control were achievable.

The complexity of sound wave propagation as well as the uniqueness of radiation patterns from an individual sound source have limited the research of active noise control in the past. As a brief review of the history of active noise control, the application of the technique began with duct noise reduction [3, 4]. Due to the fact that the sound wave below the cutoff frequency of a duct can be considered as a plane wave, the duct behaves like a one-dimensional waveguide. Consequently, the complexity of the system is reduced. Numerous reports on duct noise reduction can be found in the literature [5, 6, 7, 8] including various topics, e.g., radiation power, energy conservation, adaptive control.

Active noise control was also applied to the noise reduction of cylinders, aircraft fuselages, fans, and transformers [9, 10, 11, 12, 13]. These researches did provide en-

couraging results. However, more complicated analysis and larger costs were required as the complexity of the system increased.

For three-dimensional noise reduction, the implementation becomes even more difficult. Adaptive control system [14, 15, 16] and Wiener filters [17, 18] are the most commonly used approaches nowadays. Nevertheless, the noise attenuation is limited to certain field points. Otherwise very advanced equipment and a large signal processing time are required for silencing an area. On the other hand, the filtering technique requires a priori information about the noise in order to have satisfactory noise reduction over a specified area. In spite of the difficulties mentioned above, active noise control is superior to the traditional passive noise control in many respects. Therefore, active noise control, especially in three dimension, still remains one of the interesting topics of acoustic engineering.

## 1.2 Objective

The objective of this research is to investigate the feasibility of designing an inexpensive setup to accomplish active noise cancellation over a desired region in a free field half space bounded by an infinite plane of uniform finite impedance. The acoustic field within the half space is generated by an arbitrary shaped, stationary, and single frequency time-harmonic noise source. A number of well-controlled secondary sources are introduced to reduce the noise level over a pre-selected region. A practical example of the problem considered here might be a noisy machine installed on the ground in an open space near a residential area. The purpose of this research is to provide a technique suitable for noise level reduction over the residential area. Specifically, this technique provides the location as well as the driving

function for each individual secondary source in order to achieve noise reduction in a least square sense. Huygen's principle is used to apply the technique of active noise control. Speakers are used as practical secondary sources. This technique is shown to give satisfactory noise reduction over a prescribed area by a number of experiments performed inside an anechoic chamber for several frequencies. In addition, the application of this technique on non-steady as well as band limited frequency noise cancellation are discussed. Finally, the feasibility of using this technique to provide initial conditions for an adaptive noise control system is also briefly discussed.

### 1.3 Application of boundary element method in Acoustics

Before noise cancellation can be done, the acoustic radiation pattern from any arbitrary noise source should be identified. Various analytical and numerical methods exist to achieve this goal. The analytical methods can only be applied to problems involving sources with simple geometric shapes, e.g., spherical, cylindrical, etc. Among the numerical methods, finite-element and finite-difference methods require the discretization of the entire domain. However, for problems with domains of infinite extent, such discretization leads to a numerical system with a very large degree of freedom. In BEM, the boundary value problem of interest is transformed into an integral equation involving only surface integrals. As a result, the domain need not to be discretized, and the computation time is substantially reduced.

It will be shown in Chapter 2 that the BEM gives accurate sound radiation patterns for any arbitrary source as long as the location, shape, and boundary condition on the source are known. The BEM is also applicable to noise sources with complex shapes and non-accessible surfaces where the boundary conditions are difficult

to specify. In such cases an imaginary surface (which is called a source monitoring surface) enclosing the noise source is created as a substitute for the actual source.

Based on the sound radiation pattern calculated by BEM, two methods, namely, iterative control, and coupled equation methods, are developed in Chapter 3 to achieve noise cancellation over a prescribed region in a least square sense. The theory and the numerical simulations of these two methods are presented in Chapter 4 where BEM is used intensively. The numerical simulations were verified by a set of experiments performed inside an anechoic chamber. A speaker and a ribbed rectangular aluminum plate were used to simulate noise sources with different distribution of surface velocities. In addition, a practical and inexpensive model of secondary sources consisting of four speakers was developed to achieve noise cancellation in a desired region. Experimental results are discussed in detail in Chapter 5. The feasibility of using BEM to achieve noise cancellation is discussed in Chapter 6. Furthermore, future research on noise reduction of non-stationary as well as band limited frequency noise sources is described in Chapter 6.

# 2. BEM APPLIED TO HALF SPACE ACOUSTIC RADIATION PROBLEMS

In this chapter, the time-harmonic acoustic radiation problem, governed by Helmholtz equation is transformed into a surface integral formulation by using the reciprocal theorem. This surface integral formulation, also known as the boundary integral formulation, is applicable for any closed, connected domain. However, for the problem of acoustic radiation in half space, a mixed boundary condition is imposed over the infinite plane surface. A fundamental solution satisfying this boundary condition is derived. This fundamental solution is used in the integral formulation as the kernel function. The validity of the fundamental solution as well as the integral formulation are established by comparing the present simulations with published solutions. In addition, experimental results are used to compare with the results from BEM for cases without theoretical solutions.

## 2.1 Derivation of Boundary Integral Formulation

In order to evaluate the acoustic radiation problem, consider an arbitrary, finite source with surface $S_1$ as shown in Figure 2.1. The sound source radiates acoustic sound waves into an arbitrary, source-free space V which is filled with homogeneous, inviscid and compressible fluid. The linear acoustic field inside the domain V is

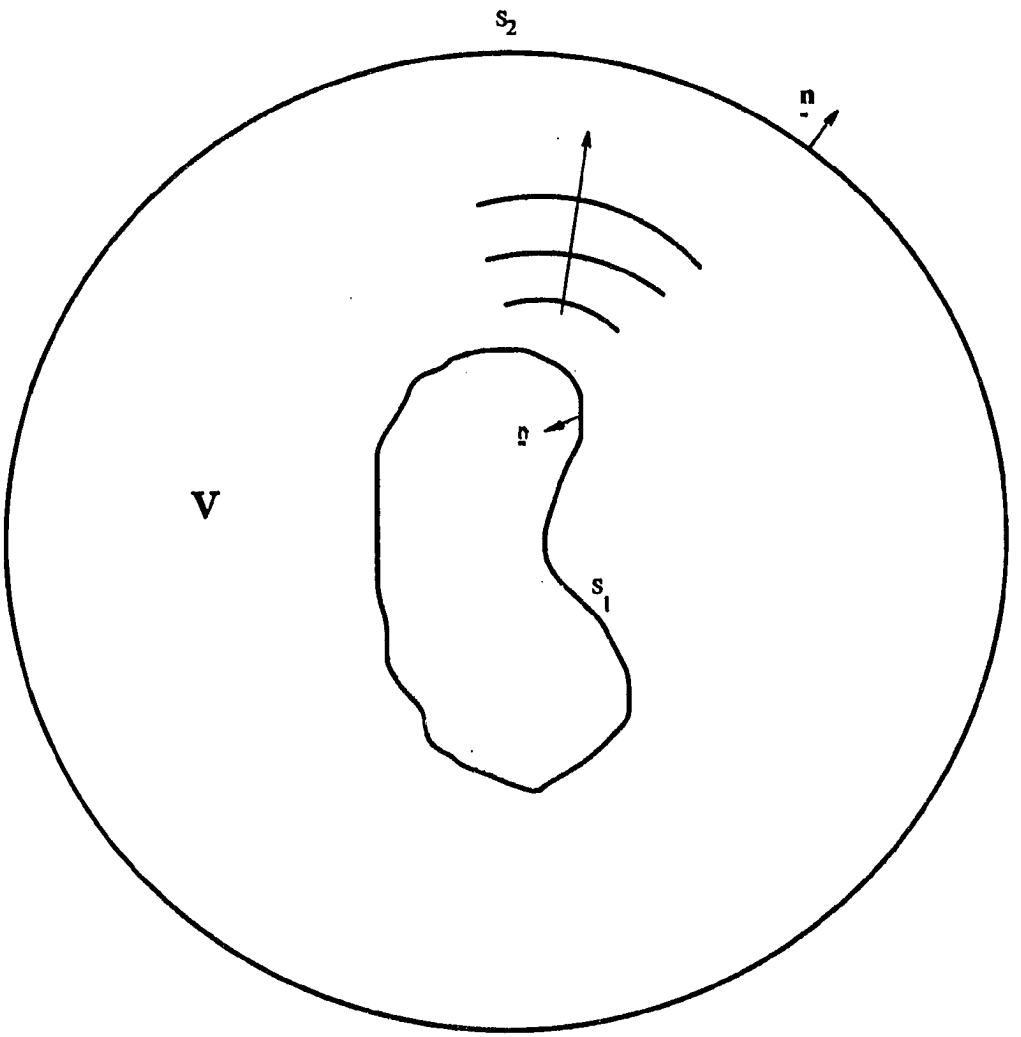


Figure 2.1: Arbitrary sound source in 3-D domain

governed by the wave equation

$$\nabla^2 \hat{\phi} - \frac{1}{c^2} \frac{\partial^2 \hat{\phi}}{\partial t^2} = -\hat{F} \tag{2.1}$$

where $\hat{\phi}$ is the velocity potential, c is the speed the the sound propagation, $\hat{F}$ is the external driving function, and t is time. The particle velocity $\vec{u}$ and acoustic pressure $\hat{p}$ are given as

$$\vec{u} = \nabla \hat{\phi} \tag{2.2}$$

$$\hat{p} = -\rho_0 \frac{\partial \hat{\phi}}{\partial t} \tag{2.3}$$

where $\rho_0$ is the density of the medium.

When time-harmonic functions are considered, that is $\hat{\phi} = \phi e^{-i\omega t}$ and $\hat{F} = f e^{-i\omega t}$, equation (2.1) reduces to the Helmholtz equation

$$\nabla^2 \phi + k^2 \phi = -f \tag{2.4}$$

where

$$\omega = kc \tag{2.5}$$

$\omega$ is the angular frequency, and k is the wave number.

Consider $\phi_1$ which satisfies

$$\nabla^2 \phi_1 + k^2 \phi_1 = -f_1 \tag{2.6}$$

and $\phi_2$ which satisfies

$$\nabla^2 \phi_2 + k^2 \phi_2 = -f_2 \tag{2.7}$$

Now consider

$$\begin{aligned} &\int_V (\phi_1 f_2 - \phi_2 f_1)\, dV \\ &= \int_V \left[ -\phi_1 \left( \nabla^2 \phi_2 + k^2 \phi_2 \right) + \phi_2 \left( \nabla^2 \phi_1 + k^2 \phi_1 \right) \right] dV \\ &= \int_V \left[ \phi_2 \nabla^2 \phi_1 - \phi_1 \nabla^2 \phi_2 \right] dV \end{aligned} \tag{2.8}$$

By Green's second identity which states that

$$\int_V \left(b \bigtriangledown^2 a - a \bigtriangledown^2 b\right) dV = \int_S \left(b\frac{da}{dn} - a\frac{db}{dn}\right) dS \tag{2.9}$$

equation (2.8) becomes

$$\int_V (\phi_1 f_2 - \phi_2 f_1)\, dV = \int_S \left[\phi_2 \frac{\partial \phi_1}{\partial n} - \phi_1 \frac{\partial \phi_2}{\partial n}\right] dS \tag{2.10}$$

or

$$\int_V \phi_1 f_2\, dV + \int_S \phi_1 \frac{\partial \phi_2}{\partial n}\, dS = \int_V \phi_2 f_1\, dV + \int_S \phi_2 \frac{\partial \phi_1}{\partial n}\, dS \tag{2.11}$$

where $S = S_1 + S_2$ is the boundary of the domain as shown in Figure 2.1, n is the unit outward normal to S.

Considering a harmonic wave generated by a point source at $\mathbf{x} = \mathbf{x_0}$. The Helmholtz equation reduces to

$$\left(\bigtriangledown^2 + k^2\right) \phi(\mathbf{x}|\mathbf{x_0}) = -\delta(\mathbf{x} - \mathbf{x_0}) \tag{2.12}$$

The solution of this equation is called the fundamental solution, and is denoted by $G(\mathbf{x}|\mathbf{x_0})$. The Dirac Delta function $\delta(\mathbf{x} - \mathbf{x_0})$ has the following sifting property

$$\int_V f(\mathbf{x_0})\, \delta(\mathbf{x} - \mathbf{x_0})\, dV(\mathbf{x_0}) = \begin{cases} f(\mathbf{x}) & \mathbf{x} \text{ in V} \\ \frac{1}{2} f(\mathbf{x}) & \mathbf{x} \text{ on S and S is smooth} \\ 0 & \mathbf{x} \text{ outside V} \end{cases} \tag{2.13}$$

Substituting $\phi_2 = \phi(\mathbf{x})$, $\phi_1 = G(\mathbf{x}|\mathbf{x_0})$, $\frac{\partial \phi_2}{\partial n} = \frac{\partial \phi(\mathbf{x})}{\partial n}$, $\frac{\partial \phi_1}{\partial n} = \frac{\partial G(\mathbf{x}|\mathbf{x_0})}{\partial n}$, $f_2 = f(\mathbf{x})$, and $f_1 = \delta(\mathbf{x} - \mathbf{x_0})$ in equation (2.11), it is found

$$\begin{aligned} &\int_V G(\mathbf{x}|\mathbf{x_0})\, f(\mathbf{x})\, dV(\mathbf{x}) + \int_S G(\mathbf{x}|\mathbf{x_0}) \frac{\partial \phi(\mathbf{x})}{\partial n}\, dS(\mathbf{x}) \\ &= \int_V \phi(\mathbf{x})\, \delta(\mathbf{x} - \mathbf{x_0})\, dV(\mathbf{x}) + \int_S \phi(\mathbf{x}) \frac{\partial G(\mathbf{x}|\mathbf{x_0})}{\partial n}\, dS(\mathbf{x}) \end{aligned} \tag{2.14}$$

From equation (2.13)

$$\int_V \phi(\mathbf{x})\,\delta(\mathbf{x}-\mathbf{x_0})\,dV(\mathbf{x}) = \eta(\mathbf{x_0})\,\phi(\mathbf{x_0})$$

where

$$\eta(\mathbf{x_0}) = \begin{cases} 1 & x_0 \text{ in V} \\ \frac{1}{2} & x_0 \text{ on S and S is smooth} \\ 0 & x_0 \text{ outside V} \end{cases} \tag{2.15}$$

Finally, the boundary integral equation becomes

$$\begin{aligned} &\eta(\mathbf{x_0})\,\phi(\mathbf{x_0}) \\ &= \int_S \left[ G(\mathbf{x}|\mathbf{x_0})\,\frac{\partial\phi(\mathbf{x})}{\partial n} - \phi(\mathbf{x})\,\frac{\partial G(\mathbf{x}|\mathbf{x_0})}{\partial n} \right] dS(\mathbf{x}) + \\ &\int_V G(\mathbf{x}|\mathbf{x_0})\,f(\mathbf{x})\,dV(\mathbf{x}) \end{aligned} \tag{2.16}$$

Furthermore, if the domain of interest is source-free, the forcing function $f(\mathbf{x})$ varnishes, and equation (2.16) becomes

$$\eta(\mathbf{x_0})\,\phi(\mathbf{x_0}) = \int_S \left[ G(\mathbf{x}|\mathbf{x_0})\,\frac{\partial\phi(\mathbf{x})}{\partial n} - \phi(\mathbf{x})\,\frac{\partial G(\mathbf{x}|\mathbf{x_0})}{\partial n} \right] dS(\mathbf{x}) \tag{2.17}$$

where S is the boundary of the domain, that is $S = S_1 + S_2$ in Figure 2.1. It can be seen in equation (2.17) that the boundary value problem has been expressed into surface integral form in terms of known boundary conditions ($\phi$ or $\frac{\partial\phi}{\partial n}$ ) and the kernel functions G and $\frac{\partial G}{\partial n}$.

Equation (2.17) is applied to the half space domain in this research as shown in Figure 2.2. The integration surface S becomes $S = S_1 + S_\infty$, where $S_\infty$ is the surface bounding the domain at infinity. The Sommerfeld radiation condition [19] which is applicable on $S_\infty$ states

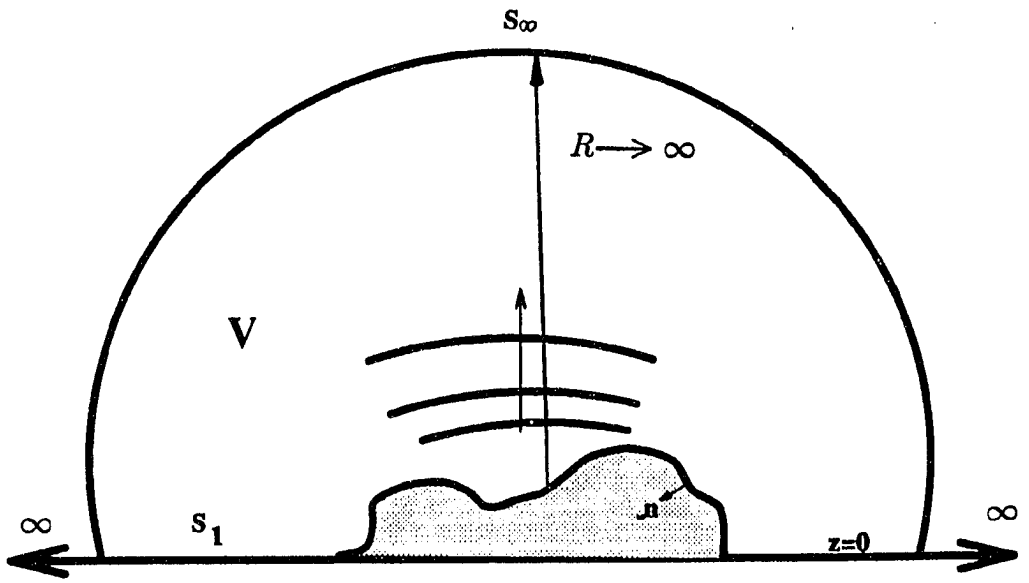


Figure 2.2: Arbitrary sound source in half space

$$\lim_{r \to \infty} \left[ r \left( p - \rho_0 c v_r \right) \right] = 0$$

or

$$\lim_{r \to \infty} \left[ r \left( \frac{\partial \phi}{\partial r} - ik\phi \right) \right] = 0 \tag{2.18}$$

where $v_r$ is the radial velocity. That is p and $v_r$ go to zero faster than $\frac{1}{r}$ as r approaches infinity. Therefore, equation (2.17) becomes

$$\begin{aligned} \eta(\mathbf{x_0})\,\phi(\mathbf{x_0}) &= \int_{S_1+S_\infty} \left[ G(\mathbf{x}|\mathbf{x_0}) \frac{\partial \phi(\mathbf{x})}{\partial n} - \phi(\mathbf{x}) \frac{\partial G(\mathbf{x}|\mathbf{x_0})}{\partial n} \right] dS(\mathbf{x}) \\ &= \int_{S_1} \left[ G(\mathbf{x}|\mathbf{x_0}) \frac{\partial \phi(\mathbf{x})}{\partial n} - \phi(\mathbf{x}) \frac{\partial G(\mathbf{x}|\mathbf{x_0})}{\partial n} \right] dS_1(\mathbf{x}) + \\ &\quad \int_{S_\infty} \left[ G(\mathbf{x}|\mathbf{x_0}) \frac{\partial \phi(\mathbf{x})}{\partial n} - \phi(\mathbf{x}) \frac{\partial G(\mathbf{x}|\mathbf{x_0})}{\partial n} \right] dS_\infty(\mathbf{x}) \\ &= \int_{S_1} \left[ G(\mathbf{x}|\mathbf{x_0}) \frac{\partial \phi(\mathbf{x})}{\partial n} - \phi(\mathbf{x}) \frac{\partial G(\mathbf{x}|\mathbf{x_0})}{\partial n} \right] dS_1(\mathbf{x}) \end{aligned} \tag{2.19}$$

Equation (2.19) gives great advantage because the integration is to be performed only on surface $S_1$. In addition, the velocity potential at any point inside the domain or on the boundary of the domain can be evaluated by equation (2.19) for any arbitrary source as long as the source location, shape, and boundary conditions are known.

## 2.2 Derivation of Half Space Green's Function

Although boundary integral equation formulation in equation (2.16) is mathematically valid for any arbitrary source in a closed, connected domain, the analytical solution is not always achievable. Therefore, the numerical scheme, BEM, is the most convenient tool to solve the equation. Nevertheless, BEM requires the discretization of the boundary of the domain. In this research the domain of interest is a half space,

and the boundary of the domain extends to infinity. Even though the Sommerfeld radiation condition can be applied to $S_\infty$ in Figure 2.2, the discretization over $S_1$, which is also extended to infinity, is inevitable. It is impractical to implement an infinite surface by using digital computer. Therefore, a fundamental solution G that not only satisfies the governing equation, but also satisfies certain boundary conditions, is necessary to reduce the complexity in applying the BEM to equation (2.19) in this research. In general, the surface $S_1$ in Figure 2.2 is of finite impedance. Therefore, a mixed boundary condition

$$\phi + c_\zeta \frac{\partial \phi}{\partial n} = 0 \tag{2.20}$$

is imposed on $S_1$. Here $c_\zeta$ is a constant related to the impedance of the surface, and uniform impedance over the surface is assumed. The method of image sources is used in order to obtain the desired fundamental solution (also known as Green's function).

Consider a time harmonic point source acting at $\mathbf{x_0}$ in the half space as shown in Figure 2.3. An image source of proper strength and phase angle acting on the opposite side of the surface can be found. Due to the linearity of the acoustic field, the finite impedance surface is relaxed. Consequently, the problem is equivalent to two point sources with different strengths and phase angles acting in the free space with the constraint of source locations. However, only the upper half of the free space is the domain of interest. The fundamental solution for Helmholtz equation in free space is

$$G_f(k,r) = \frac{e^{ikr}}{4\pi r}$$

where k is wave number and r is the distance between source point and point of interest. The half space Green's function is then expressed as

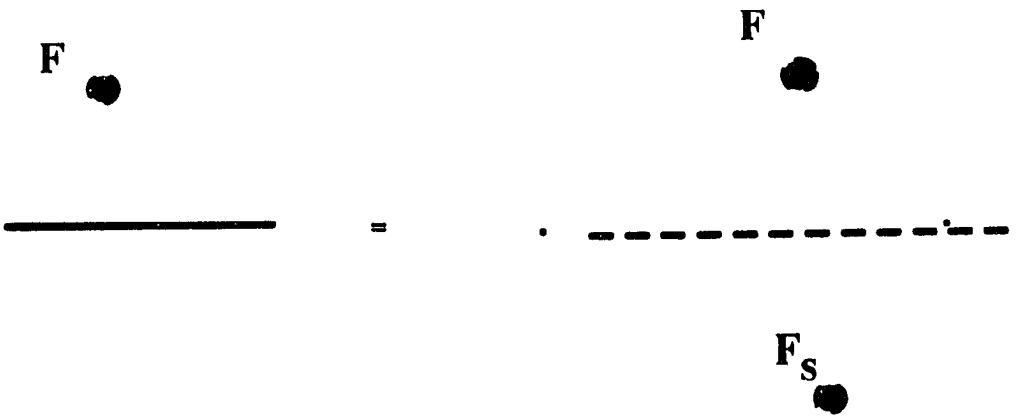


Figure 2.3: Method of image source

$$G_h(\mathbf{x}|\mathbf{x_0},\mathrm{k}) = \frac{e^{ikr_1}}{4\pi r_1} + F_s\frac{e^{ikr_2}}{4\pi r_2} \tag{2.21}$$

where

$$\mathbf{x_0} = (\mathrm{x_0},\mathrm{y_0},\mathrm{z_0}) \quad \text{and} \quad \mathbf{x} = (\mathrm{x},\mathrm{y},\mathrm{z})$$

$$r_1 = \sqrt{(x-x_0)^2+(y-y_0)^2+(z-z_0)^2}$$

and

$$r_2 = \sqrt{(x-x_0)^2+(y-y_0)^2+(z+z_0)^2}$$

and $F_s$ is a complex quantity related to the strength and phase angle of the image source. The half space Green's function is forced to satisfy the mixed boundary condition. That is

$$G_h(k|r) + c_\zeta\frac{\partial G_h(k|r)}{\partial n} = 0 \text{ at } z = 0 \tag{2.22}$$

From the chain rule of differentiation

$$\begin{aligned}\frac{\partial G_h(\mathbf{x}|\mathbf{x_0},\mathrm{k})}{\partial n} &= \frac{\partial\left(\frac{e^{ikr_1}}{4\pi r_1}\right)}{\partial r_1}\frac{\partial r_1}{\partial n} + \frac{\partial\left(\frac{F_s e^{ikr_2}}{4\pi r_2}\right)}{\partial r_2}\frac{\partial r_2}{\partial n} \\ &= \frac{-1+ikr_1}{4\pi r_1}\frac{e^{ikr_1}}{r_1}\frac{\partial r_1}{\partial n} + F_s\frac{-1+ikr_2}{4\pi r_2}\frac{e^{ikr_2}}{r_2}\frac{\partial r_2}{\partial n}\end{aligned}$$

That is

$$\begin{aligned}&G_h(\mathbf{x}|\mathbf{x_0},\mathrm{k}) + c_\zeta\frac{\partial G_h(\mathbf{x}|\mathbf{x_0},\mathrm{k})}{\partial n} \\ =\ &\frac{e^{ikr_1}}{4\pi r_1} + \frac{F_s e^{ikr_2}}{4\pi r_2} \\ &+c_\zeta\left[\frac{-1+ikr_1}{4\pi r_1}\frac{e^{ikr_1}}{r_1}\frac{\partial r_1}{\partial n} + F_s\frac{-1+ikr_2}{4\pi r_2}\frac{e^{ikr_2}}{r_2}\frac{\partial r_2}{\partial n}\right]\end{aligned} \tag{2.23}$$

As the source point approaches the $z = 0$ plane (finite impedance plane), so does the image source. Consequently, $r_1 = r_2 = r = \sqrt{(x-x_0)^2 + (y-y_0)^2 + (z)^2}$. Equation (2.23) becomes

$$\begin{aligned} & G_h\left(\mathbf{x}|\mathbf{x_0}, \mathrm{k}\right) + c_\zeta \frac{\partial G_h\left(\mathbf{x}|\mathbf{x_0}, \mathrm{k}\right)}{\partial n} \\ & = \frac{e^{ikr_1}}{4\pi r_1} + \frac{F_s e^{ikr_2}}{4\pi r_2} + c_\zeta \left[ \frac{-1+ikr_1}{4\pi r_1} \frac{e^{ikr_1}}{r_1} \frac{\partial r_1}{\partial n} + F_s \frac{-1+ikr_2}{4\pi r_2} \frac{e^{ikr_2}}{r_2} \frac{\partial r_2}{\partial n} \right] \\ & = 0 \text{ at } z = 0 \end{aligned} \tag{2.24}$$

Moreover,

$$\frac{\partial r_1}{\partial n} = -\frac{\partial r_2}{\partial n} \quad and \quad \frac{\partial r_2}{\partial n} = \cos\theta \ at z = 0$$

where $\theta$ is the angle between $\vec{r}$ and $\vec{n}$.

Equation (2.24) can be reduced to

$$1 + F_s - c_\zeta \cos\theta \left( \frac{-1+ikr}{r} \right) + F_s c_\zeta \cos\theta \left( \frac{-1+ikr}{r} \right) = 0 \tag{2.25}$$

Consequently,

$$F_s = \frac{c_\zeta \cos\theta \left( \frac{-1+ikr}{r} \right) - 1}{c_\zeta \cos\theta \left( \frac{-1+ikr}{r} \right) + 1} \tag{2.26}$$

Finally, the half space Green's function is expressed as

$$G_h\left(\mathbf{x}|\mathbf{x_0}, \mathrm{k}\right) = \frac{e^{ikr_1}}{4\pi r_1} + \frac{c_\zeta \cos\theta \left( \frac{-1+ikr}{r} \right) - 1}{c_\zeta \cos\theta \left( \frac{-1+ikr}{r} \right) + 1} \frac{e^{ikr_2}}{4\pi r_2} \tag{2.27}$$

There are two important limiting cases for equation (2.27). First, if the $z = 0$ surface is rigid which means $\frac{\partial \phi}{\partial n} = 0$ and $c_\zeta = \infty$, the half space Green's function reduces to

$$G_h r\left(\mathbf{x}|\mathbf{x_0}, \mathrm{k}\right) = \frac{e^{ikr_1}}{4\pi r_1} + \frac{e^{ikr_2}}{4\pi r_2} \tag{2.28}$$

which agrees with the Green's function used in Rayleigh integral. Secondly, if the $z = 0$ surface is pressure released, which means $\phi = 0$ and $c_\zeta = 0$, the half space Green's function reduces to

$$G_h p(\mathbf{x}|\mathbf{x_0}, \mathrm{k}) = \frac{e^{ikr_1}}{4\pi r_1} - \frac{e^{ikr_2}}{4\pi r_2} \tag{2.29}$$

which is also well-known in acoustics.

With the insertion of the derived Green's function satisfying the boundary condition (2.27), the integration surface in equation (2.19) is reduced to the surface of the source only. Consider the integration surface $S_1$ in Figure 2.2. The surface $S_1$ is broken into the combination of two surfaces, the surface of the source,$S_s$, and the surface of the plane boundary,$S_p$. That is

$$S_1 = S_s + S_p$$

Equation (2.19) can be expressed as

$$\begin{aligned} & \eta(\mathbf{x_0})\,\phi(\mathbf{x_0}) \\ = & \int_{S_s} \left[ G_h(\mathbf{x}|\mathbf{x_0}) \frac{\partial \phi(\mathbf{x})}{\partial n} - \phi(\mathbf{x}) \frac{\partial G_h(\mathbf{x}|\mathbf{x_0})}{\partial n} \right] dS_s(\mathbf{x}) + \\ & \int_{S_p} \left[ G_h(\mathbf{x}|\mathbf{x_0}) \frac{\partial \phi(\mathbf{x})}{\partial n} - \phi(\mathbf{x}) \frac{\partial G_h(\mathbf{x}|\mathbf{x_0})}{\partial n} \right] dS_p(\mathbf{x}) \end{aligned} \tag{2.30}$$

However,

$$G_h(\mathbf{x}|\mathbf{x_0}, \mathrm{k}) + c_\zeta \frac{\partial G_h(\mathbf{x}|\mathbf{x_0}, \mathrm{k})}{\partial n} = 0 \text{ on } S_p$$

The second integral term in equation (2.30) becomes

$$\begin{aligned} & \int_{S_p} \left[ G_h(\mathbf{x}|\mathbf{x_0}) \frac{\partial \phi(\mathbf{x})}{\partial n} - \phi(\mathbf{x}) \frac{\partial G_h(\mathbf{x}|\mathbf{x_0})}{\partial n} \right] dS_p(\mathbf{x}) \\ = & \int_{S_p} \left[ G_h(\mathbf{x}|\mathbf{x_0}) \frac{\partial \phi(\mathbf{x})}{\partial n} - \phi(\mathbf{x}) \left( -\frac{G_h(\mathbf{x}|\mathbf{x_0})}{c_\zeta} \right) \right] dS_p(\mathbf{x}) \end{aligned}$$

$$= \int_{S_p} G_h(\mathbf{x}|\mathbf{x_0}) \left[ \frac{\partial \phi(\mathbf{x})}{\partial n} + \frac{\phi(\mathbf{x})}{c_\zeta} \right] dS_p(\mathbf{x})$$
$$= 0 \tag{2.31}$$

because of the mixed boundary condition

$$\phi + c_\zeta \frac{\partial \phi}{\partial n} = 0 \text{ on } S_p.$$

Consequently, equation (2.30) becomes

$$\eta(\mathbf{x_0})\,\phi(\mathbf{x_0}) = \int_{S_s} \left[ G_h(\mathbf{x}|\mathbf{x_0}) \frac{\partial \phi(\mathbf{x})}{\partial n} - \phi(\mathbf{x}) \frac{\partial G_h(\mathbf{x}|\mathbf{x_0})}{\partial n} \right] dS_s(\mathbf{x}) \tag{2.32}$$

Equation (2.32) is more practical to be applied to the BIE formulation. Specifically, the magnitude of discretization is significantly reduced, and that leads to less equations and less unknowns. Consequently, computation cost is dramatically reduced.

Equation (2.32) shows that full knowledge,i.e., both $\phi$ and $\frac{\partial \phi}{\partial n}$ of every nodal point on the surface of the source is required in order to evaluate the velocity potential at any point inside the domain. However, $\phi$ and $\frac{\partial \phi}{\partial n}$ can not be specified independently as the boundary condition at the same time. The problem can be circumvented by taking the point of interest to the boundary. That is taking $\mathbf{x} \rightarrow \mathbf{x_0} \in \mathbf{S_s}$. This limiting process reduces equation (2.32) to a boundary integral equation. The full knowledge of any point on the boundary is known when one of them or the linear relationship between them is specified. It should be noted that $G_h(\mathbf{x}|\mathbf{x_0})$ is $O\left(\frac{1}{r}\right)$ and $\frac{\partial G_h(\mathbf{x}|\mathbf{x_0})}{\partial n}$ is $O\left(\frac{1}{r^2}\right)$. Consequently, the limiting process will lead to singularity due to r approaching zero. However, both $G_h(\mathbf{x}|\mathbf{x_0})$ and $\frac{\partial G_h(\mathbf{x}|\mathbf{x_0})}{\partial n}$ are weakly singular. The integration of BIE can be evaluated numerically with the help of the regularization technique to both singular terms.

In order to numerically evaluate the integral equation shown in equation (2.32), BEM starts with discretizing the surface of the source into surface elements. The surface elements used in this research are either 8-node curvilinear quadrilateral or 6-node triangular elements, which map to squares or equilateral triangles respectively. The numbering of those nodes in each surface element is chosen such that the connectivity of the surface element gives the desired normal direction (see Figure 2.4). Consequently, the surface of the source is discretized into m surface elements with n total nodal points on it. The geometry of the surface elements and the unknown variables are approximated by using quadratic isoparametric shape functions [20] such that the continuous functions of unknown variables can be evaluated at discrete nodal points. The variable $\phi$ over each element is approximated by

$$\phi(\zeta) = \sum_{j=1}^{n_p} N_j(\zeta)\,\phi_j \tag{2.33}$$

where $\zeta_i$ is the local coordinates of each element, $n_p$ is the number of nodal points of each element, $N_j(\zeta)$ are the quadratic shape functions , and $\phi_j$ are the nodal values of $\phi$.

Similarly, the surface geometry of each element is also approximated by the same quadratic shape function in a similar manner through each node on the element.

$$\mathbf{x} = \sum_{\mathbf{j}=1}^{\mathbf{n_p}} \mathbf{N_j}(\zeta)\,\mathbf{x_j} \tag{2.34}$$

where $\mathbf{x_j}$ is the coordinates of the $j^{th}$ node, $\mathbf{x}$ is the global cartesian coordinate of any point on the element.

The integral equation in equation (2.32) is now ready to be evaluated numerically.

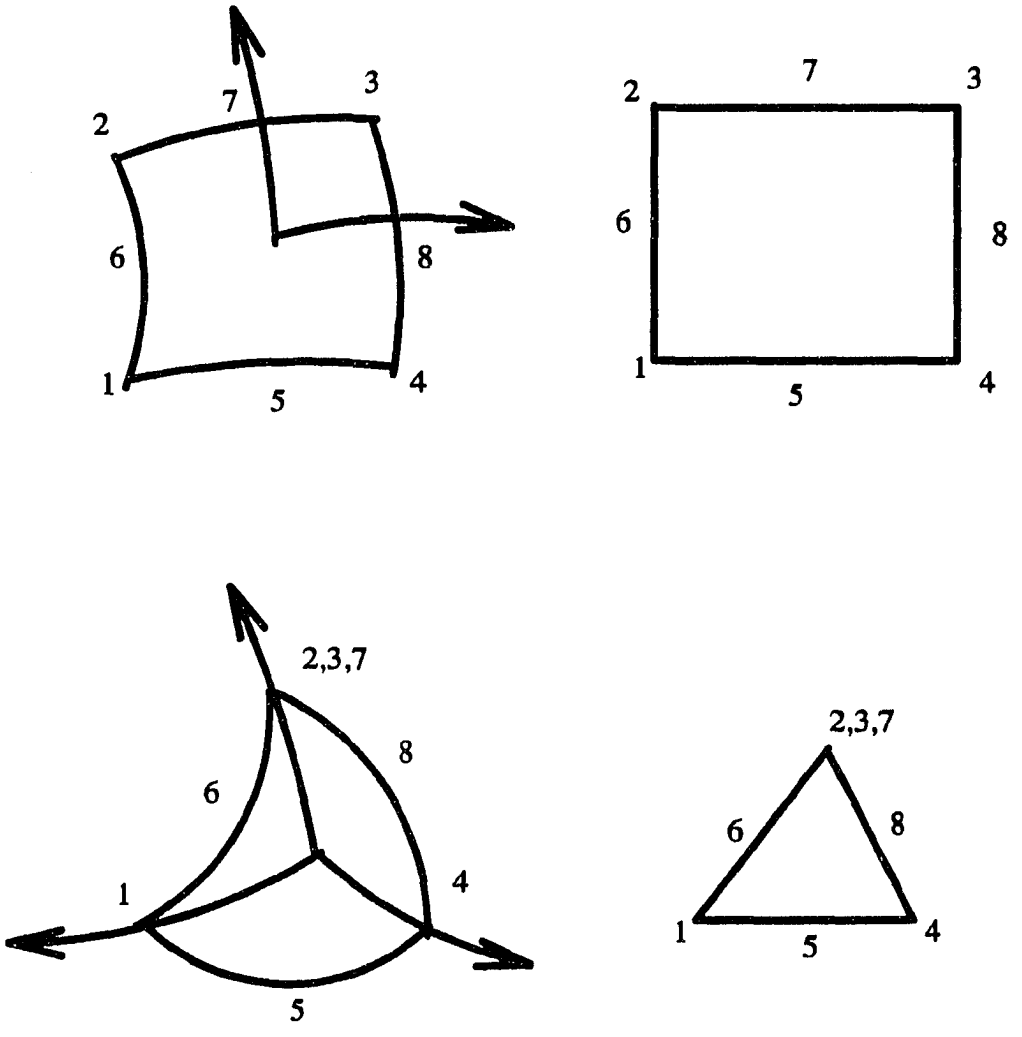


Figure 2.4: Surface elements and connectivity

Note that the integral equation has the generic form

$$I(\mathbf{x}) = \int_S \psi(\mathbf{x_0})\, K(\mathbf{x}|\mathbf{x_0})\, dS(\mathbf{x_0}) \tag{2.35}$$

where I is the field variable of interest, $\psi$ is the variable on the boundary, K is the integration kernel.

Equation (2.35) can be approximated as

$$I = \sum_{i=1}^{m} \sum_{j=1}^{n_p} \psi_{ij} \left[ \int_{S_e} N_j(\zeta)\, K(\mathbf{x}|\zeta)\, J(\zeta)\, dS_e(\zeta) \right] \tag{2.36}$$

where m is total number of elements, $n_p$ is the number of nodal points on each element, J is the Jacobian of transformation, $\psi_{ij}$ is the discrete value of $\psi$ at the $j^{th}$ node on $i^{th}$ element, and $S_e$ is the area of each element. In terms of local coordinates $\zeta_1$ and $\zeta_2$ one can write

$$dS_e(\zeta) = J(\zeta_1, \zeta_2)\, d\zeta_1 d\zeta_2.$$

The integration on each element is evaluated by Gaussian quadrature [20] with proper choice of Gaussian integration points. It should be noted that the integral will be singular when BIE is considered. However, the singular kernel in the integral equation is transformed into non-singular integration by dividing the element into two or three triangles and corresponding coordinates change from Cartesian to polar coordinates. Details of the evaluation of the singular integration are discussed in Appendix A. The integral equation is then approximated by a set of linear algebraic equations involving complex quantities. The system of equations is expressed in matrix form at n nodal points as follows

For BIE

$$[\mathbf{A} - \eta\mathbf{I}]_{n*n} \{\phi(\mathbf{x})\}_{n*1} + [\mathbf{B}]_{n*n} \left\{ \frac{\partial \phi(\mathbf{x})}{\partial n} \right\}_{n*1} = \{\mathbf{0}\}_{n*1} \tag{2.37}$$

where $n * n$ in the subscript indicates that the rank of the matrix is n by n.
The system of equations can be solved when the boundary conditions are imposed.

The variable $\phi$ at any point $\mathbf{x_0}$ inside the domain is calculated from

$$\{\phi(\mathbf{x_0})\}_{1*1} = [\mathbf{a}]_{1*n} \{\phi(\mathbf{x})\}_{n*1} + [\mathbf{b}]_{1*n} \left\{ \frac{\partial \phi(\mathbf{x})}{\partial n} \right\}_{n*1} \tag{2.38}$$

Consequently, the boundary value problem is solved numerically.

## 2.3 Numerical Test Cases

A set of numerical simulations for various source conditions are tested here to verify the validity of BIE formulation and the half space Green's function. The test cases are:

- point source above a finite impedance plane,
- baffled piston,
- baffled beam,
- baffled plate,
- pressure released piston,
- pulsating sphere in a free field,
- two spheres in a free field.

In addition, the accuracy of using a source monitoring surface to predict acoustic radiation patterns is investigated. A baffled piston source was used as an actual source. Imaginary cylindrical as well as hemi-spherical source monitoring surfaces enclosing

the piston were used to predict the acoustic field outside the source monitoring surface.

The simulation results were compared with analytical solutions to verify the BIE formulation and BEM technique. Experimental data were used to compare with BEM simulations whenever the analytical solutions were not available. It should be noted that the far field acoustic radiation was investigated in most cases. However, it does not mean that the BEM technique cannot be applied to near field acoustic radiation. In fact, the prediction of near field acoustic radiation by the BEM technique gives good accuracy which will be shown in the baffled piston case.

### 2.3.1 Point source above a finite impedance plane

The half space Green's function was the first to be verified. The acoustic pressure from point source above the finite impedance plane [21] is expressed as

$$p = \frac{e^{ikr_1}}{kr_1}\left\{1 + \frac{r_1}{r_2} Q exp\left[ikr_1\left(\frac{r_2}{r_1} - 1\right)\right]\right\} \tag{2.39}$$

where

$$\begin{aligned} Q &= R_0 + (1 - R_0)\,\rho^{\frac{1}{4}} e^{\frac{\rho}{2}} W_{\frac{-1}{4},\frac{1}{4}}(\rho) \\ &= R_0 + (1 - R_0)\left\{1 - (\pi\rho)^{\frac{1}{2}} e^{\rho}\left[1 - \Phi(\rho)^{\frac{1}{2}}\right]\right\} \end{aligned} \tag{2.40}$$

$$\rho = \frac{ikr_2(\gamma_0 + \beta)^2}{2(1 + \gamma_0\beta)}$$

$$R_0 = \frac{\cos\theta_0 - \beta}{\cos\theta_0 + \beta}$$

$$\gamma_0 = \cos\theta_0$$

$$\beta = \frac{\rho_0 c}{\zeta}$$

$\zeta$ is the impedance of the infinite plane, W is Whittaker function, $r_1$ is the distance between field point and the actual source, $r_2$ is the distance between field point and the imaginary source, $\theta_0$ is the angle between incident wave from the actual source and the normal direction of the finite impedance plane, $\rho_0$ is the density of the medium, and $\Phi$ is the error function.

Comparison of the pressure from equation (2.39) with the pressure obtained from half space Green's function in equation (2.32) showed very good agreement. Three different impedance values for $\beta = 10$, 1, and 0.1 for k=1 were tested when the point source was placed on the finite impedance surface. The acoustic pressure pattern for these three cases are shown in Figures 2.5 through 2.7.

In addition, two different impedance values for $\beta = 10$ and 1 were tested when the point source was above the finite impedance plane at a distance $kh = 5$, where h is the distance above the finite impedance plane, and $k = 1$. Figures 2.8 and 2.9 indicate that the match for the pressure distribution is perfect. However, it was not possible to evaluate the case for $\beta = 0.1$ and $kh = 5$ because $\Phi(\rho)^{\frac{1}{2}}$ in equation (2.39) was beyond the tabulated range. From the cases tested above, one can conclude that the half space Green's function is valid for the mixed boundary condition in this research.

### 2.3.2 Baffled piston

Consider a flat piston mounted in a rigid baffle as shown in Figure 2.10. The theoretical pressure field along the acoustic axis (the z axis) of the baffled piston [22] is

$$p(r,0) = 2\rho_0 c U_0 \left| \sin\left\{ \frac{1}{2} kr \left[ \sqrt{1 + \left(\frac{a}{r}\right)^2} - 1 \right] \right\} \right| \qquad (2.41)$$

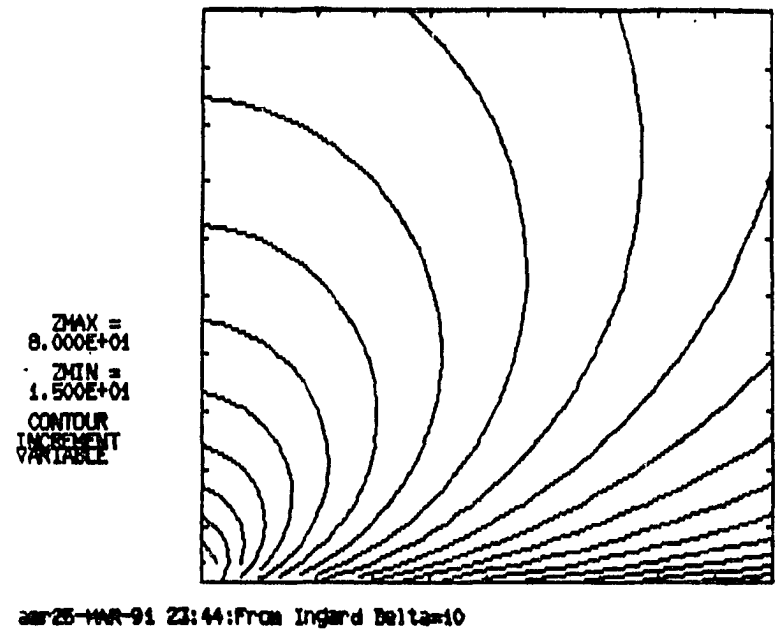


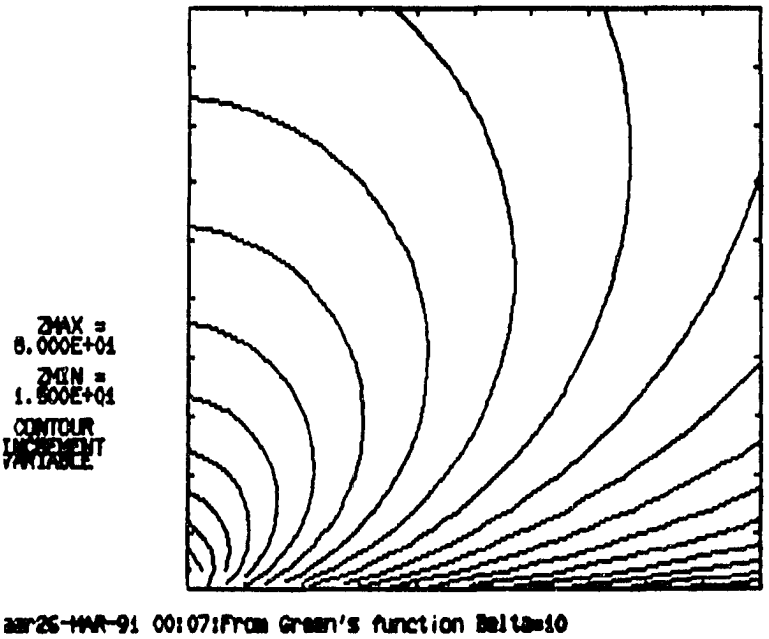


Figure 2.5: Pressure magnitude on yz-plane with point source on finite impedance plate with $\beta = 10$. top: published data [21], bottom: half space Green's function

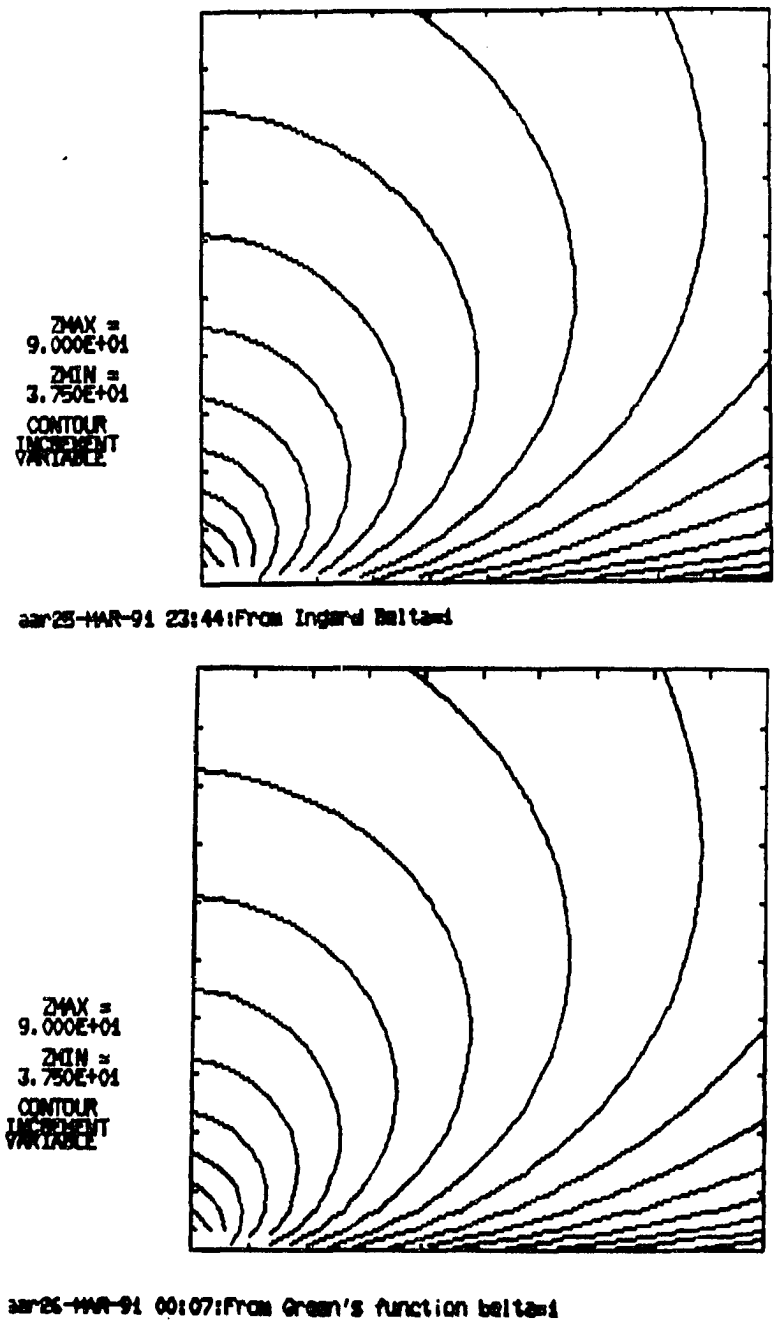


Figure 2.6: Pressure magnitude on yz-plane with point source on finite impedance plate with $\beta = 1$. top: published data [21], bottom: half space Green's function

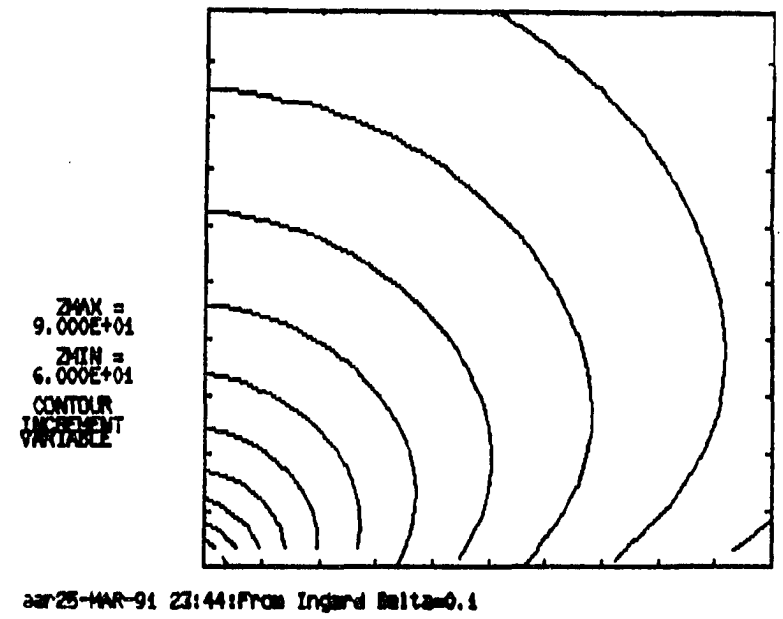


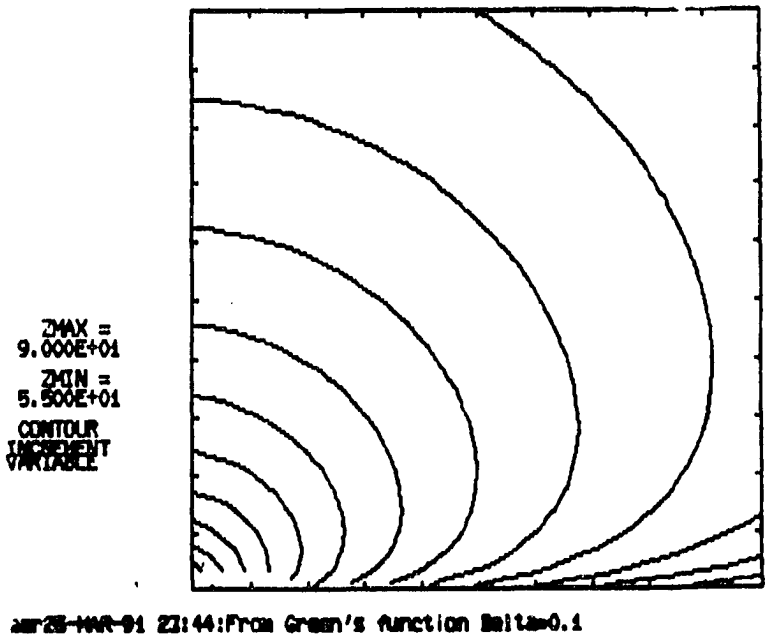


Figure 2.7: Pressure magnitude on yz-plane with point source on finite impedance plate with $\beta = 0.1$. top: published data [21], bottom: half space Green's function

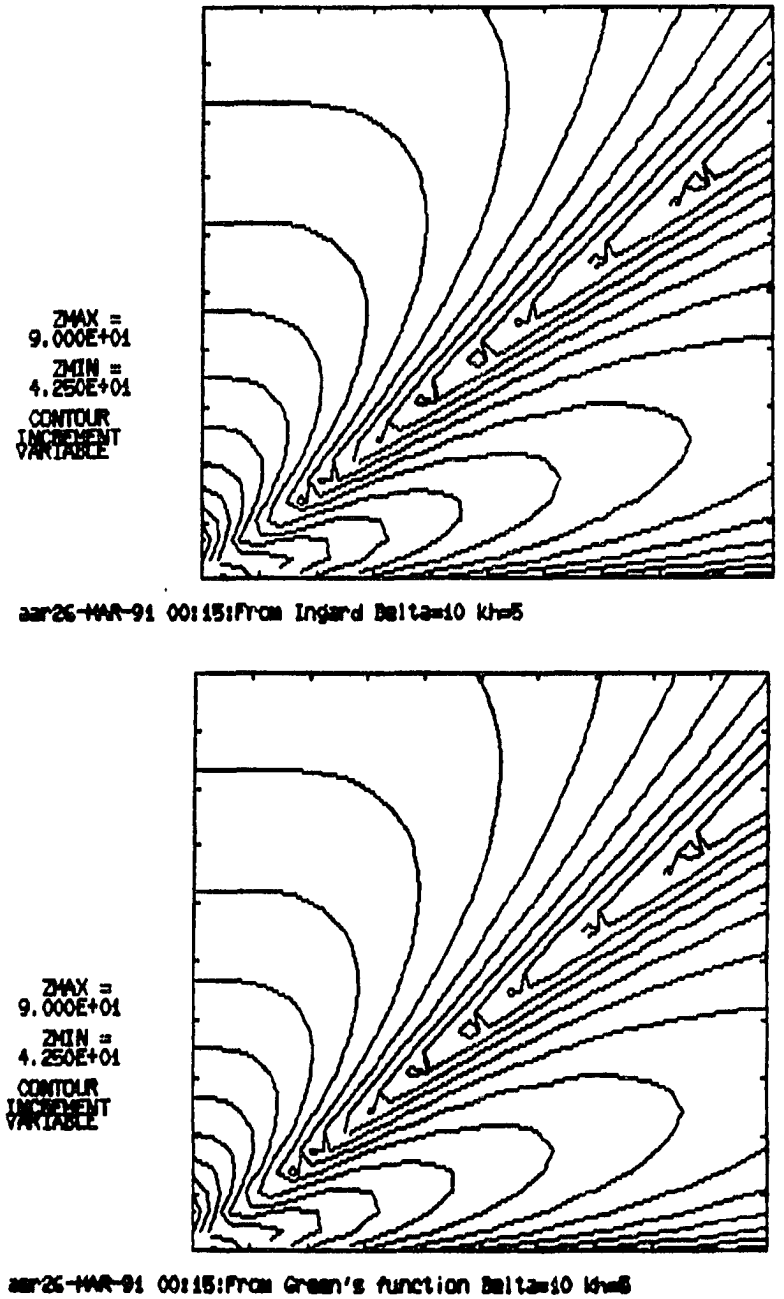


Figure 2.8: Pressure magnitude on yz-plane with point source above finite impedance plate at $kh = 5$ with $\beta = 10$. top: published data [21], bottom: half space Green's function

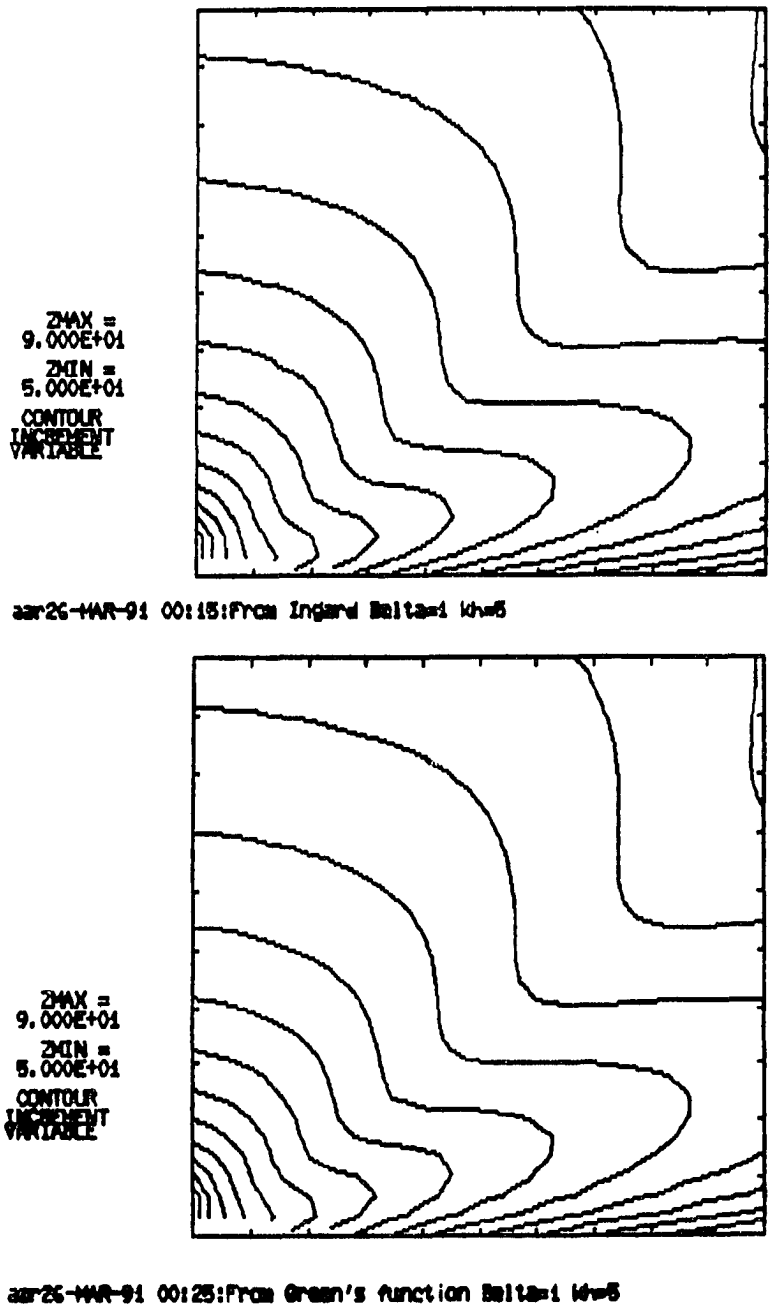


Figure 2.9: Pressure magnitude on yz-plane with point source above finite impedance plate at $kh = 5$ with $\beta = 1$. top: published data [21], bottom: half space Green's function

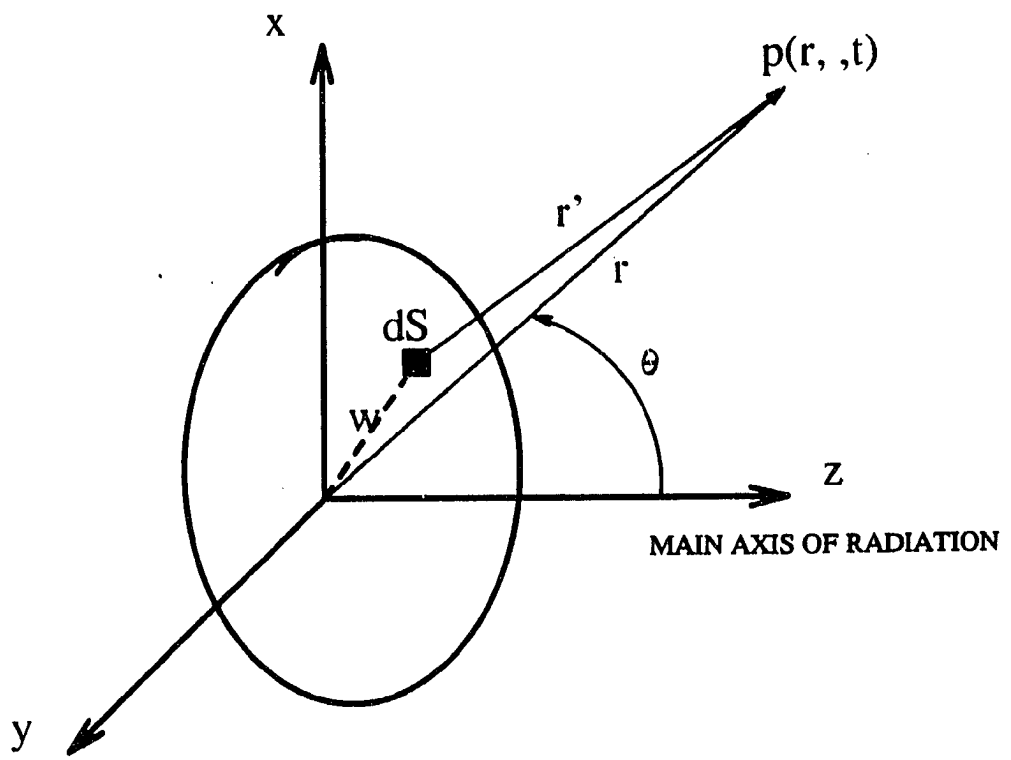


Figure 2.10: Configuration for baffle piston

where $\rho_0$ is the density of the medium, c is the wave speed, $U_0$ is the uniform velocity over the surface of the piston, k is the wave number, a is the radius of the piston, and r is the distance from a field point to the center of the piston.

The surface of the piston was discretized into 97 nodes and 32 elements. The on-axis pressure obtained by BEM simulations were compared with the theoretical solution in equation (2.41) for $ka = 5$ (Figure 2.11) and $ka = 30$ (Figure 2.12). The comparison shows that the results from BEM are almost identical to the analytical solutions in either the near or far acoustic field. In addition, the far field acoustic radiation pattern (including points away from the main axis ) for a baffled piston was calculated. Consider a baffled piston with the configuration shown in Figure 2.10. The analytical far field acoustic pressure was approximated by [22]

$$p(r,\theta) = i\frac{\rho_0 c}{2} U_0 \frac{a}{r} kae^{-ikr}\left[\frac{2J_1(ka\sin\theta)}{ka\sin\theta}\right] \tag{2.42}$$

where $J_1$ is the Bessel function of first kind.

The numerical result in Figure 2.13 shows excellent comparison with Equation (2.42). However, the analytical solution for the near field acoustic radiation pattern is not available for the baffled piston source. Therefore, an approximation of near field acoustic pressure obtained by Bennink [23] was used to compare with the BEM simulations. Figures 2.14 and 2.15 indicated very good agreements between BEM and approximated solution for near field acoustic radiation.

A speaker was mounted in a $8' \times 8'$ plywood to simulate the baffled piston source for experimental verification of the validity of BEM. Two different speakers of 6" and 10" diameter were tested. The experiments were done inside the anechoic chamber at 100 Hz, 1000 Hz and 2000 Hz frequencies. The input voltage to the speaker was measured as an estimate of the normalized surface velocity of the speaker with the as-

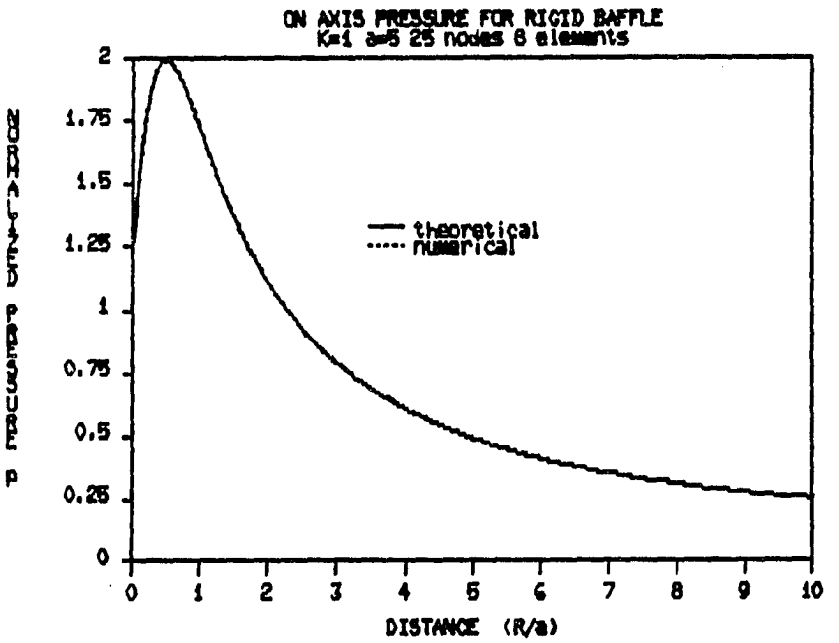


Figure 2.11: On axis pressure magnitude of baffled piston at $ka = 5$

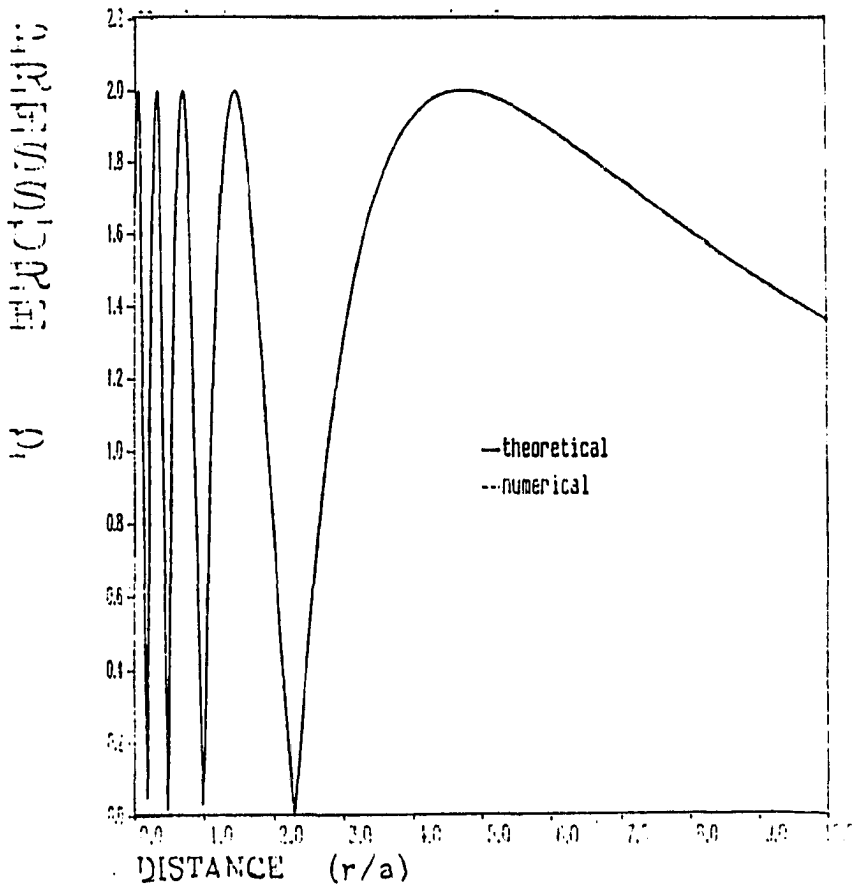


Figure 2.12: On axis pressure magnitude of baffled piston at $ka = 30$

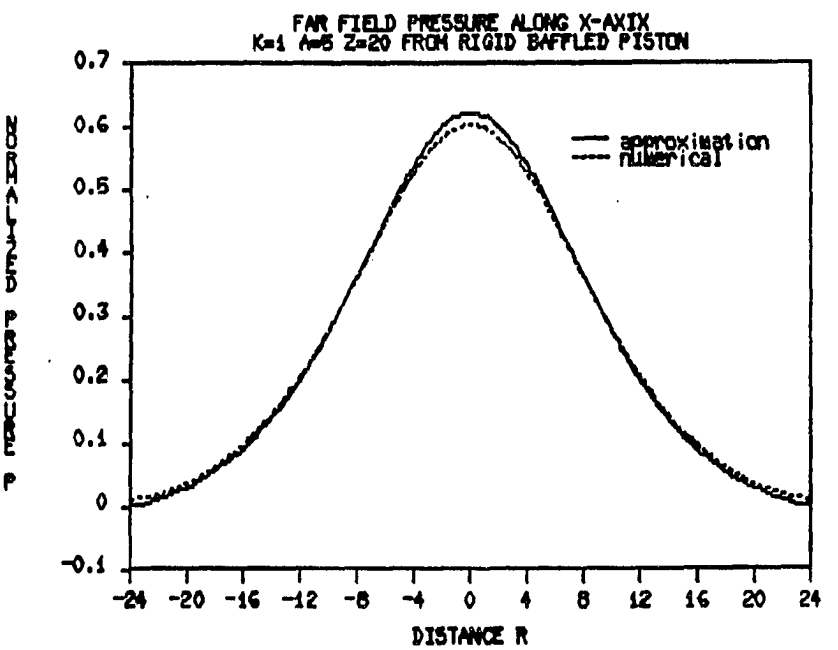


Figure 2.13: Far field pressure magnitude along x-axis from baffled piston source $z = 20$

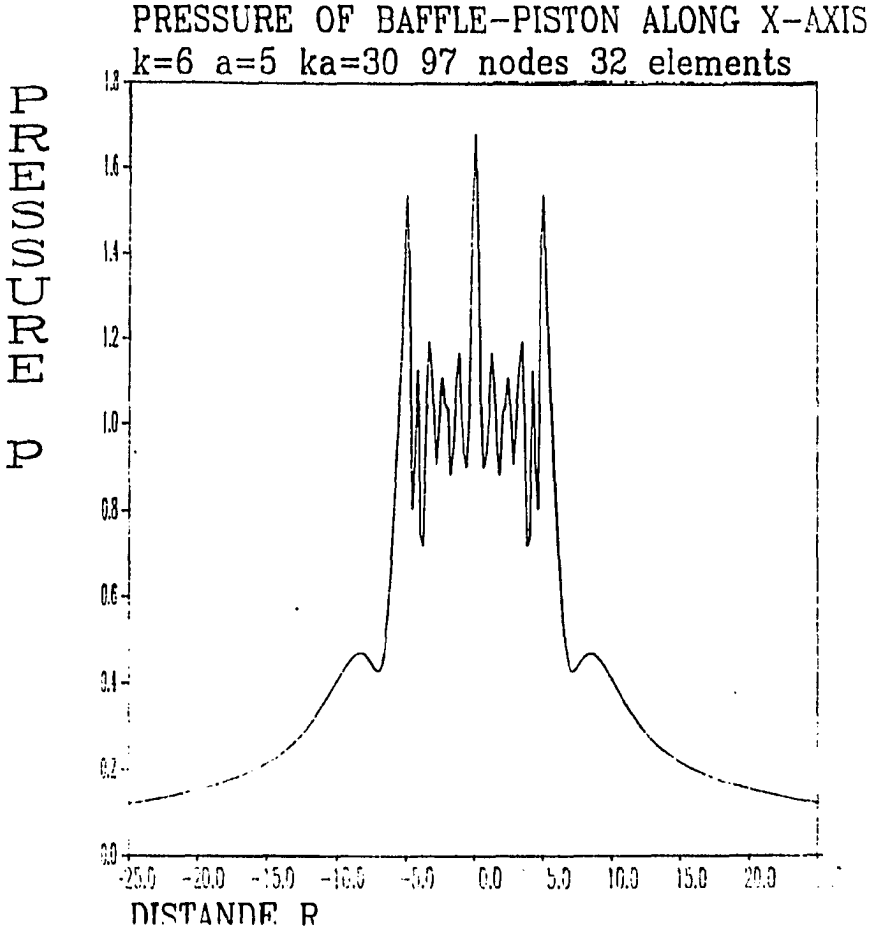


Figure 2.14: Near field pressure magnitude along x-axis from baffled piston source $z = 0.1$

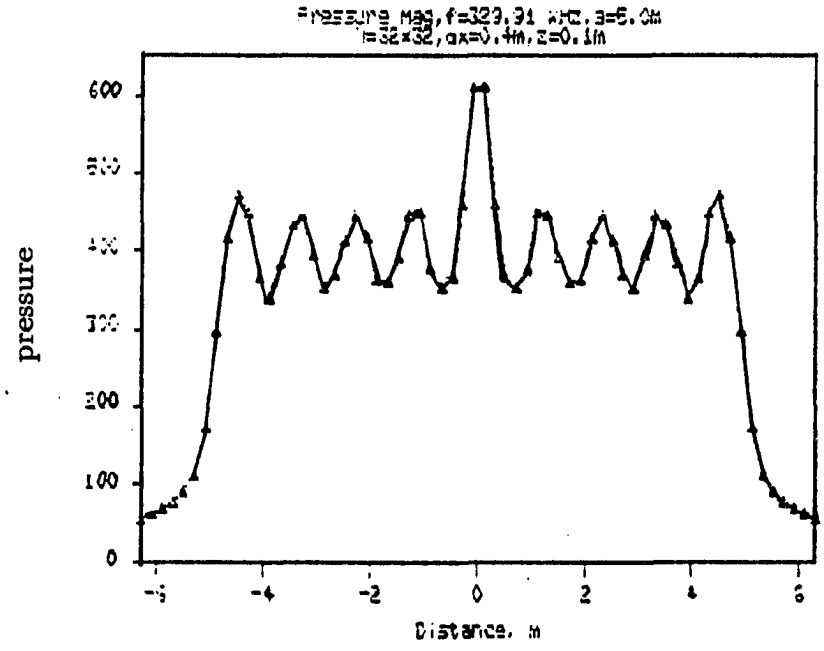


Figure 2.15: Approximated near field pressure magnitude along x-axis from baffled piston

sumption of the linear response of the speaker. In addition, the surface of the speaker was cone shaped instead of a flat plane which was assumed in theoretical derivations for baffled piston source. Despite the discrepancies in assumptions, the experimental results show satisfactory agreement with the BEM simulations as presented in Figures 2.16 and 2.17 when the transfer function between the input voltage and the surface velocity of the speaker is accounted for. Therefore, it has been confirmed that the BEM technique gives very accurate predictions of the acoustic radiation from a baffled piston source in both near and far field.

### 2.3.3 Baffled beam

A $61cm \times 5.08cm \times 0.3175cm$ aluminum beam was chosen to be the noise source as shown in Fig. 2.18. The beam was baffled and driven by a shaker with sine wave excitation at 21.88 Hz ($k = 0.400805m^{-1}$), which was the first mode of the homogeneous hinged beam. The surface of the beam was discretized into 43 nodes and 8 elements. The numerical simulation of acoustic radiation over a plane three times the length and width of the beam at 2 cm above the baffle surface is shown in Figure 2.19. In addition, the acoustic pressure over the same plane was experimentally measured by a quarter-inch microphone. It is clearly seen that the the radiation pattern agrees well with the numerical result from the BEM. In addition, the far field directivity of the baffled beam was also tested and compared with approximation data. An excellent match can be found in Figure 2.20.

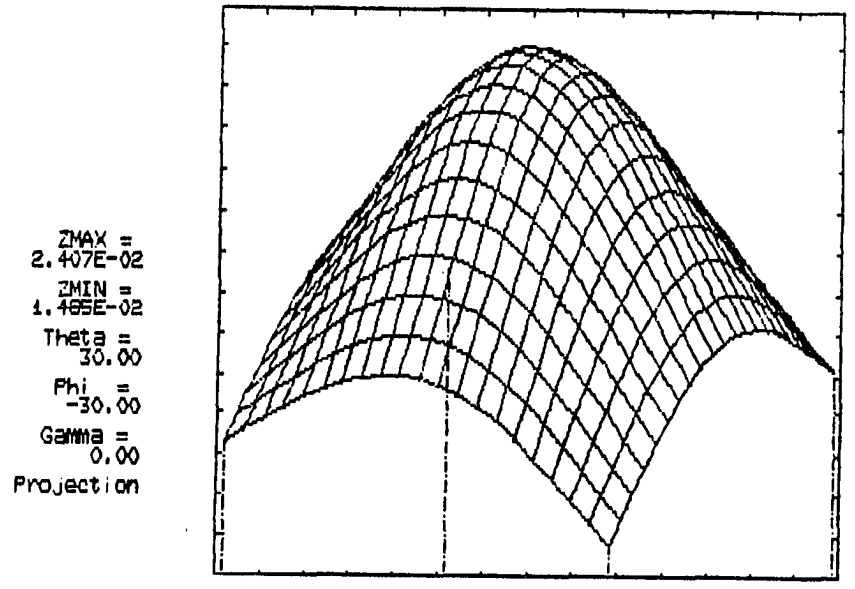


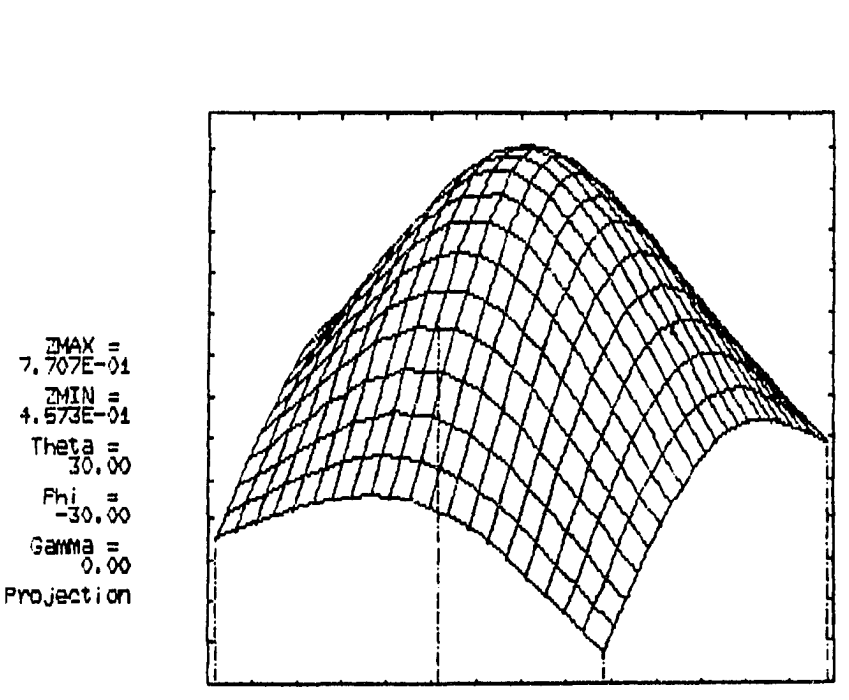


Figure 2.16: Theoretical and experimental pressures magnitude from baffled piston at $f = 100Hz, a = 6.5", z = 20cm$. top: theoretical pressure, bottom: experimental pressure

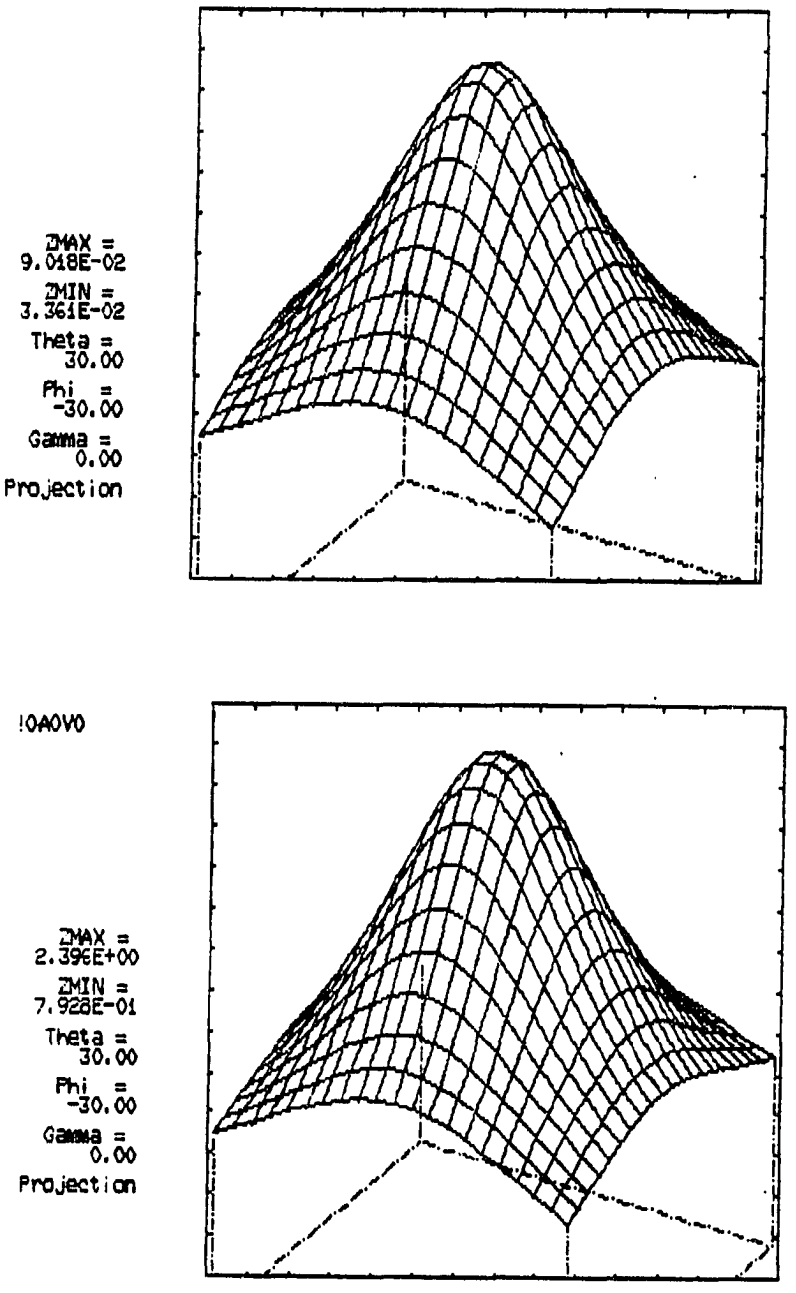


Figure 2.17: Theoretical and experimental pressures magnitude from baffled piston at $f = 100Hz, a = 10", z = 20cm$. top: theoretical pressure, bottom: experimental pressure

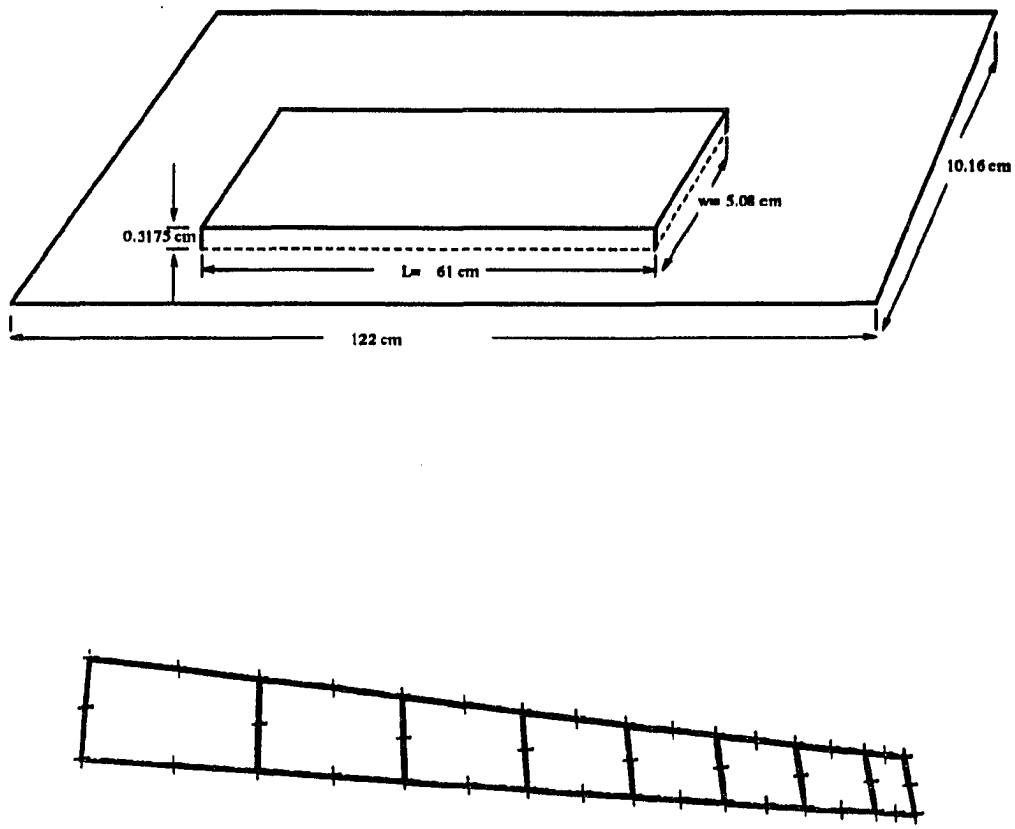


Figure 2.18: Baffled beam. top:configuration of baffled beam, bottom: discretization of beam

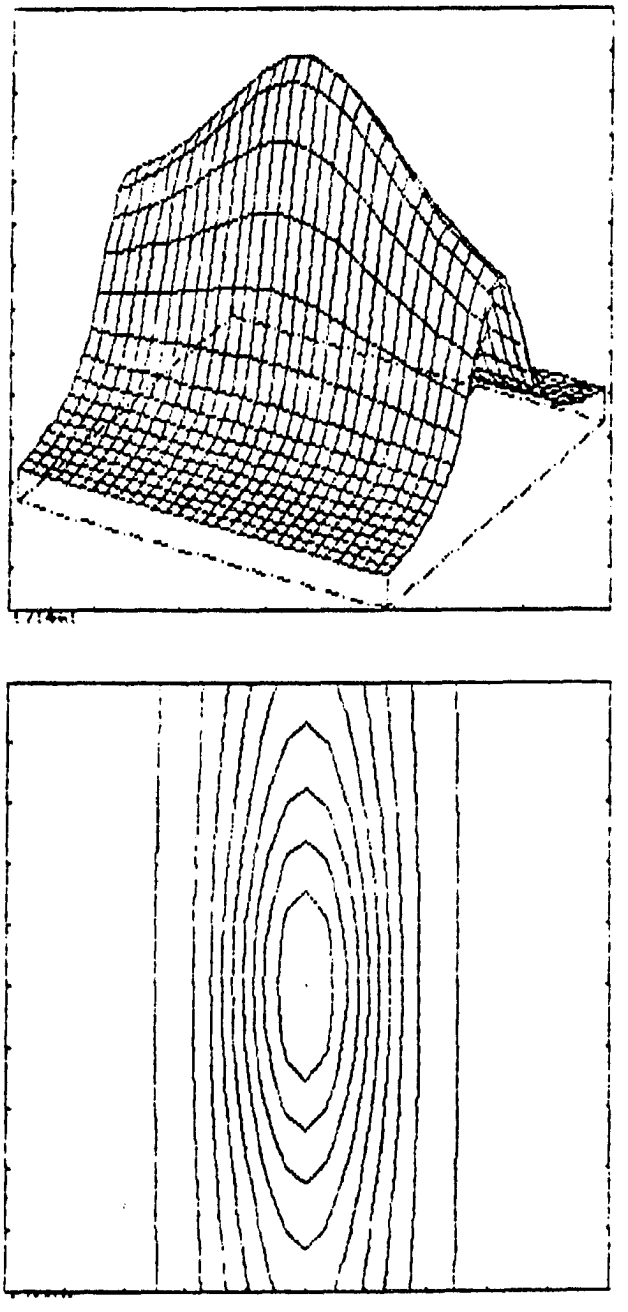

Figure 2.19: Pressure from baffle beam over $3L \times 3W$ plane at 2 cm above the beam surface

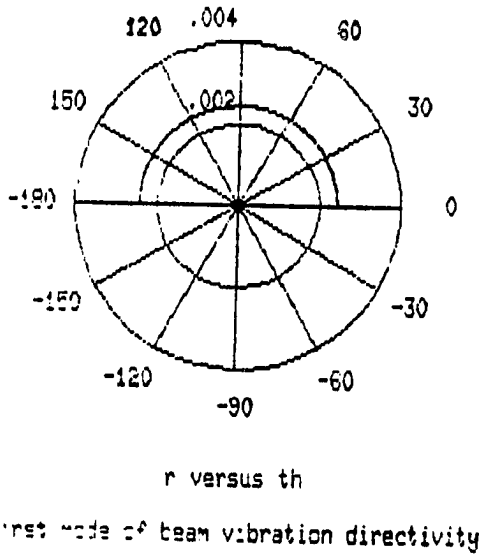


Figure 2.20: Far field directivity of baffled beam vibrating in a first mode (Beam has $L = 0.61m, W = 0.0508m, R = 1m$)

### 2.3.4 Baffled plate

A ribbed aluminum plate with dimensions $71.12cm \times 60cm \times 0.3175cm$ was used as a noise source as shown in Figure 2.21. The plate was baffled and driven by a shaker with time harmonic function at 83 Hz ($k = 1.520421m^{-1}$). There is no analytical solution for acoustic radiation from the ribbed plate so that the experimental measurement of acoustic pressure over a $128cm \times 128cm$ plane at 2cm above the baffle and the plate was used to compare with the numerical calculations from BEM. The acoustic pressure was measured with a quarter-inch microphone which was mounted on a 2-D scanner. The scanner was controlled by a micro-vax I computer. The measured signal was processed by a FFT frequency analyzer, and thus transferred via IEEE 488 interface bus to computer for post-processing. Only 21 nodes and 4 elements were used for the BEM scheme. The numerical results give satisfactory prediction for the acoustic pressure as shown in Figure 2.22. It is clear that BEM gives good accuracy in predicting the acoustic radiation for baffled sources regardless the type of source being used.

### 2.3.5 Pressure released piston

The pressure released boundary condition, which corresponds to impedance $\zeta = 0$, is considered on the surface of the baffle. The analytical solution for acoustic radiation along the z-axis for the piston in a pressure released baffle is

$$p(r,0) = rp_0 \left[ \frac{e^{ik\sqrt{r^2+a^2}}}{\sqrt{r^2+a^2}} - \frac{e^{ikr}}{r} \right] \tag{2.43}$$

where r is the distance from a field point to the center of the piston, a is the radius of the piston, k is the wave number, and $p_0$ is the uniform pressure over the surface

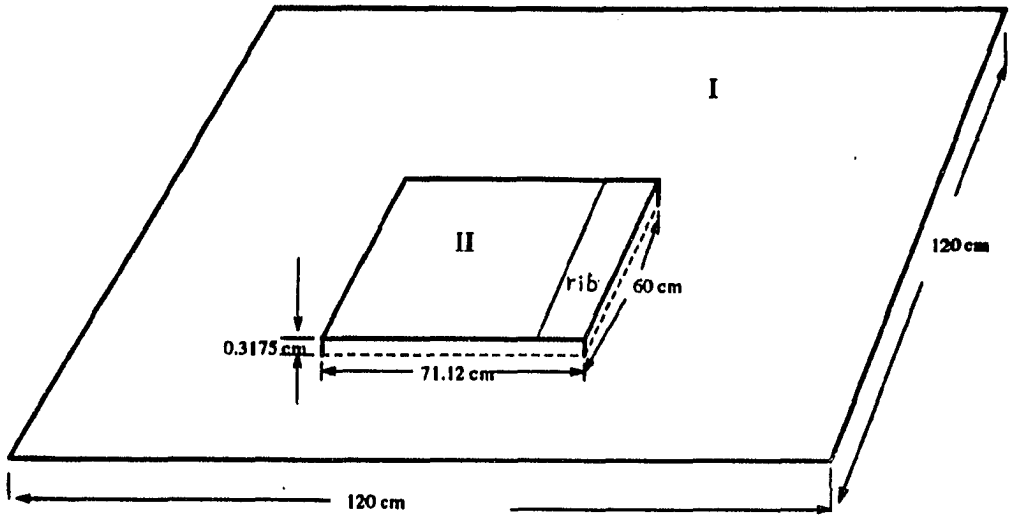


**I - baffle**

**II - plate**

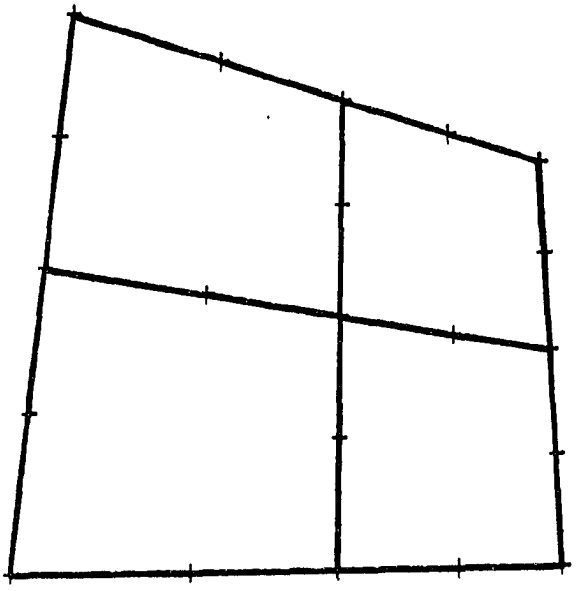

Figure 2.21: Baffled plate. top: geometric configuration, bottom: discretization

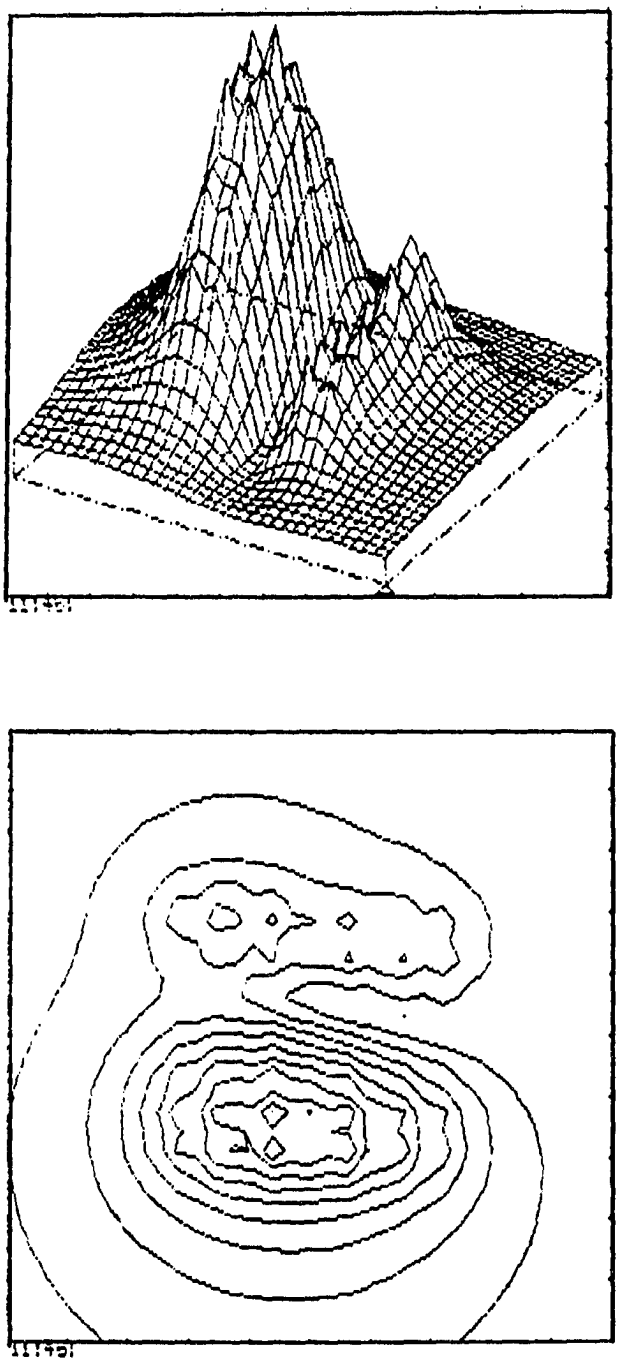

Figure 2.22: Pressure magnitude from baffled plate over $128cm \times 128cm$ plane at $z = 2cm$

of the piston. The detailed derivation of (2.43) is shown in Appendix B.

The surface of the piston was discretized into 97 nodes and 32 elements. The same configuration as in Figure 2.10 was used except the boundary condition was changed to a pressure released case. Figures 2.23 and 2.24 show the comparison between the BEM calculations and analytical solutions for $ka = 5$ and $ka = 30$, respectively. Almost identical results were found in both cases for the near and far field acoustic radiation along the z-axis. It is noted that BEM scheme can also be applied to off axis acoustic radiation for the pressure released piston. Since the analytical solution is not available, the results for off axis acoustic radiation from a pressure released piston are not presented here.

### 2.3.6 Pulsating sphere in a free field

Another example investigated here is a pulsating sphere in a free field with uniform boundary conditions. However, a hemisphere was used in BEM simulation because of the symmetry. The discretization of the hemisphere was shown in Figure 2.25. The hemisphere of unit radius was discretized into 73 nodes and 24 elements.

The theoretical solution for acoustic pressure outside the sphere in free field [19] is

$$\frac{p}{\rho_0 c} = \frac{-ika^2 v_s}{r(1-ika)} e^{ikr} \tag{2.44}$$

where $\rho_0$ is the density of the medium, c is the wave speed, k is the wave number, a is the radius of the sphere, $v_s$ is the surface velocity of the sphere, and r is the distance from point of interest to the center of the sphere.

Either pressure or velocity on the surface of the sphere were specified as boundary conditions to investigate the acoustic pressure along the x-axis at a distance twice

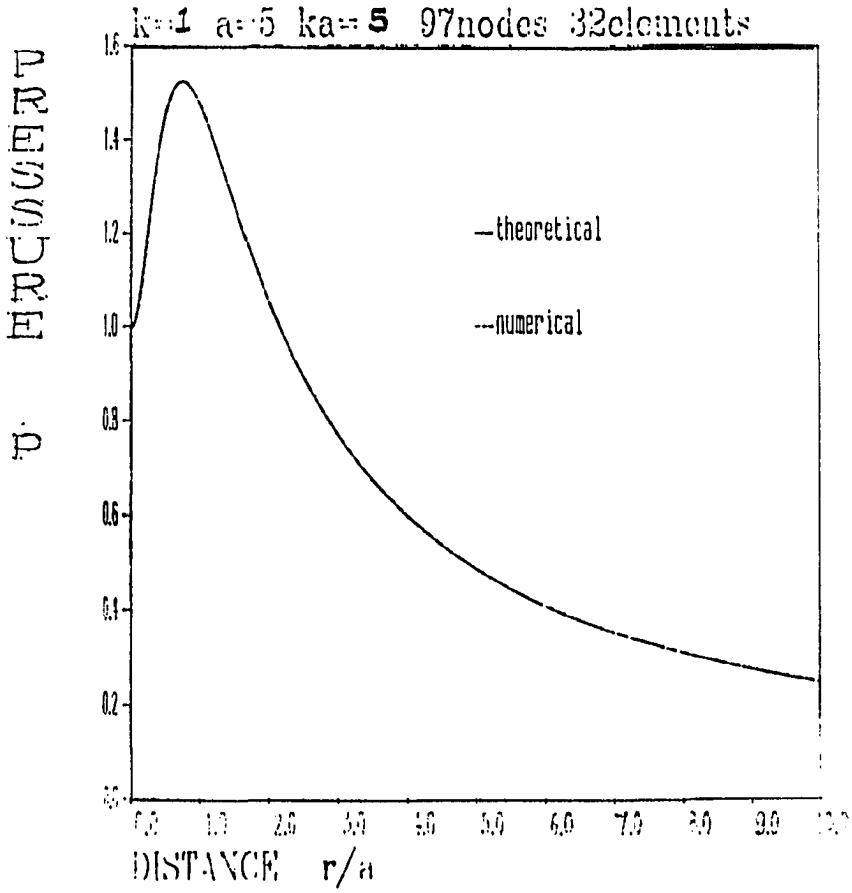


Figure 2.23: On axis pressure magnitude for piston in pressure released baffle at $ka = 5$

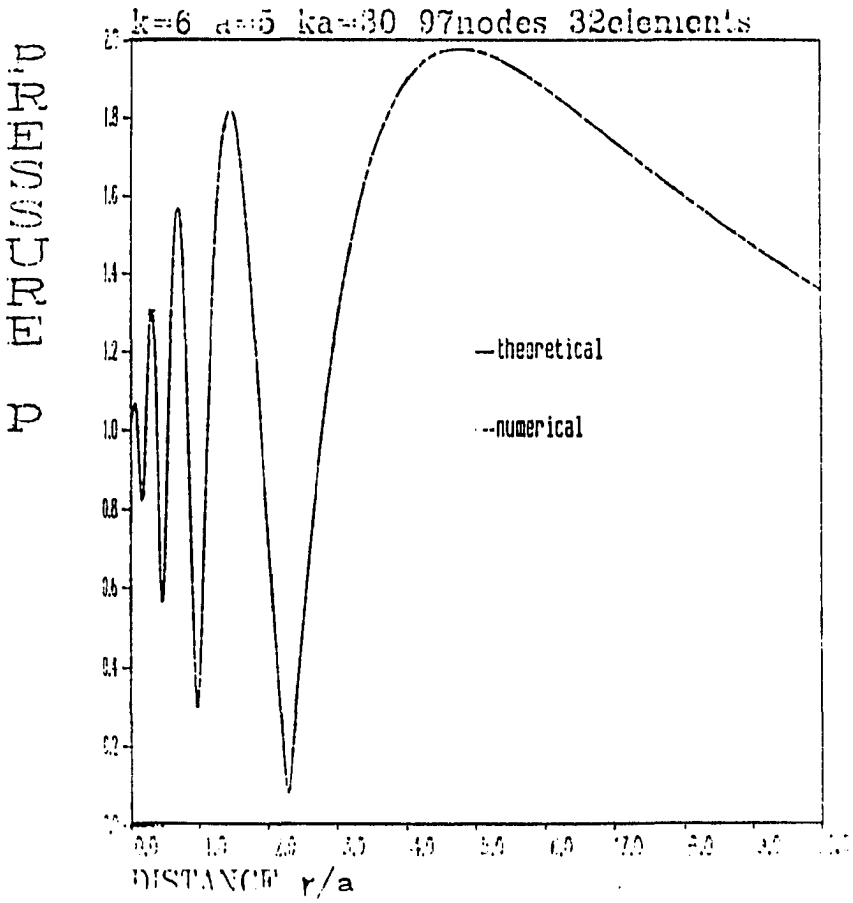


Figure 2.24: On axis pressure magnitude from piston in pressure released baffle at $ka = 30$

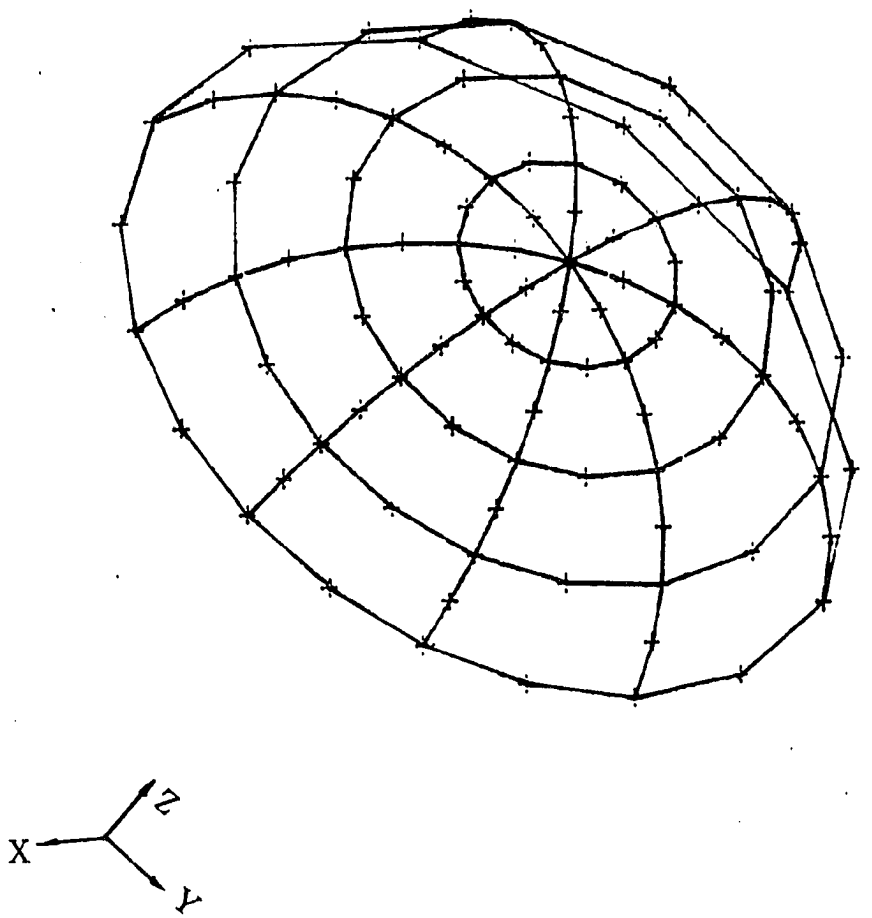


Figure 2.25: Discretization of a hemi-sphere of radius a

the radius above the center of the sphere. Figure 2.26 shows the pressure with $ka = 1$, and Figure 2.27 shows the pressure for the same configuration with $ka = 5$. Both cases show good accuracy in predicting the acoustic radiation for a pulsating sphere in a free field with either surface pressure or velocity of the sphere specified.

### 2.3.7 Two spheres in a free field

Two small spheres oscillating radially in an unbounded space were included as another test case. Due to the symmetry, two hemispheres with unit radius were discretized as shown in Figure 2.28 to simulate the spheres. Each hemisphere had 25 nodes and 8 elements. The distance between the center of the two spheres was three times the radius of the sphere. The analytical solution for acoustic pressure at any point in the space [19] is

$$p(r,\theta) = \frac{A}{r} e^{-i\left(kr+\frac{\gamma}{2}\right)} \left[2\cos\left(\frac{kd}{2}\sin\theta - \frac{\gamma}{2}\right)\right] \quad . \tag{2.45}$$

where A is the amplitude of the surface pressure on both spheres, r is the distance from the point of interest to the center between the two spheres, $\gamma$ is the phase difference between the surface pressure of the two spheres, d is the distance between the center of the two spheres, and $\theta$ is the angle between $\vec{r}$ and $\vec{z}$.

The pressure at 121 points distributed over a half circle with radius 5 times the radius of the spheres was calculated and compared with theoretical solutions. Figure 2.29 shows both the numerical and theoretical results when the pressure on the surface of the two spheres were in phase, while Figure 2.30 shows the same results when the surface pressures were out of phase. It can be seen in these figures that the agreement between theoretical solutions and BEM calculations were extremely good for both

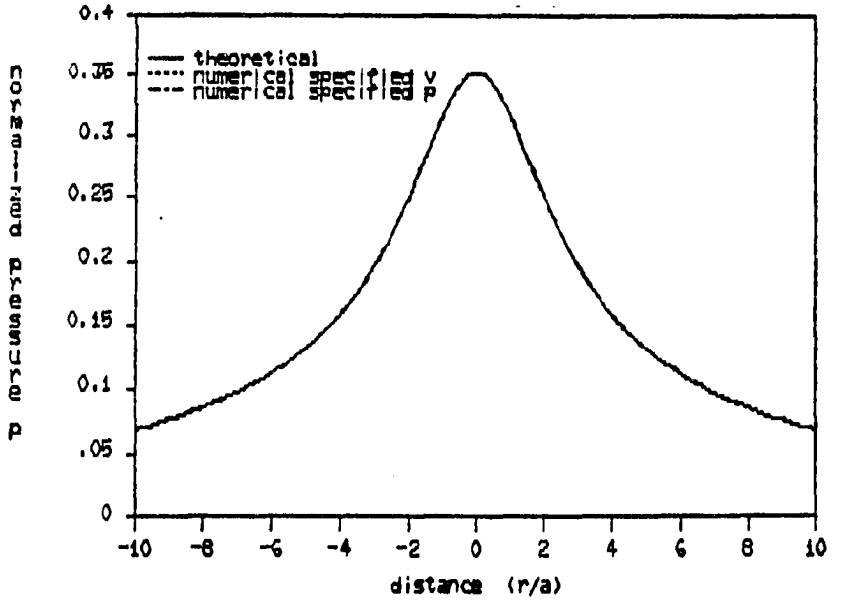


Figure 2.26: Pressure magnitude along x-axis ($z = 2a$) for pulsating sphere at $ka = 1$

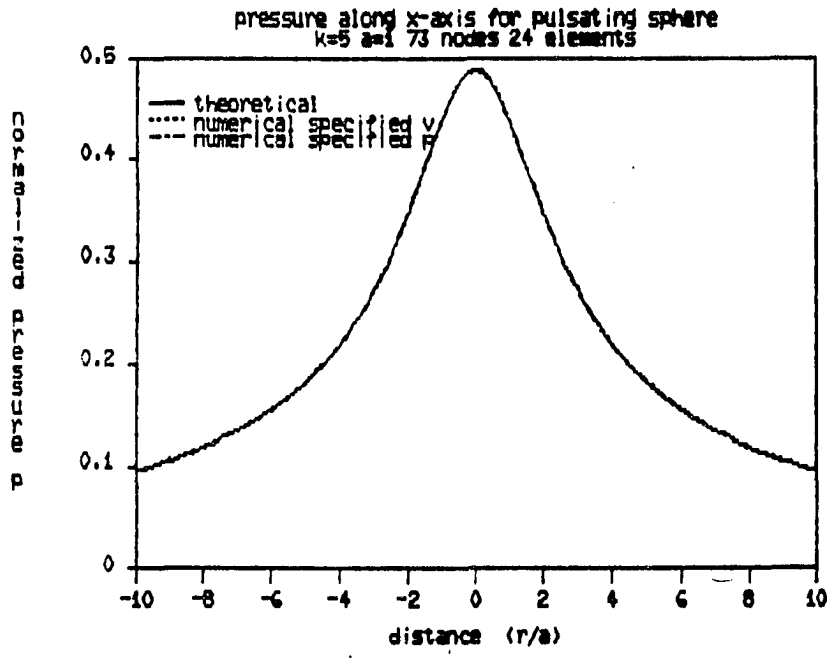


Figure 2.27: Pressure magnitude along x-axis ($z = 2a$) for pulsating sphere at $ka = 5$

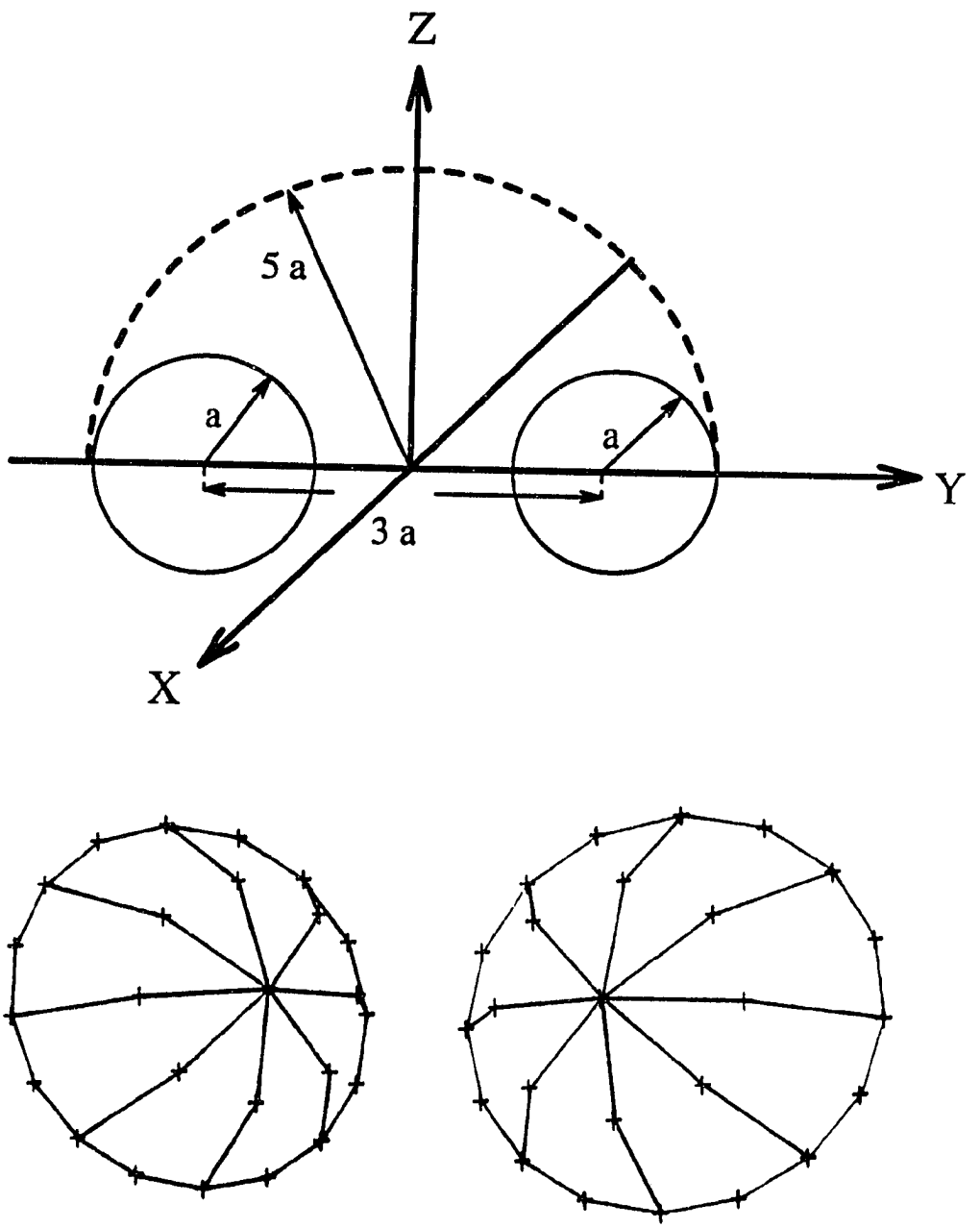


Figure 2.28: Two pulsating spheres. top: configuration of two spheres, bottom: discretization of two hemi-spheres

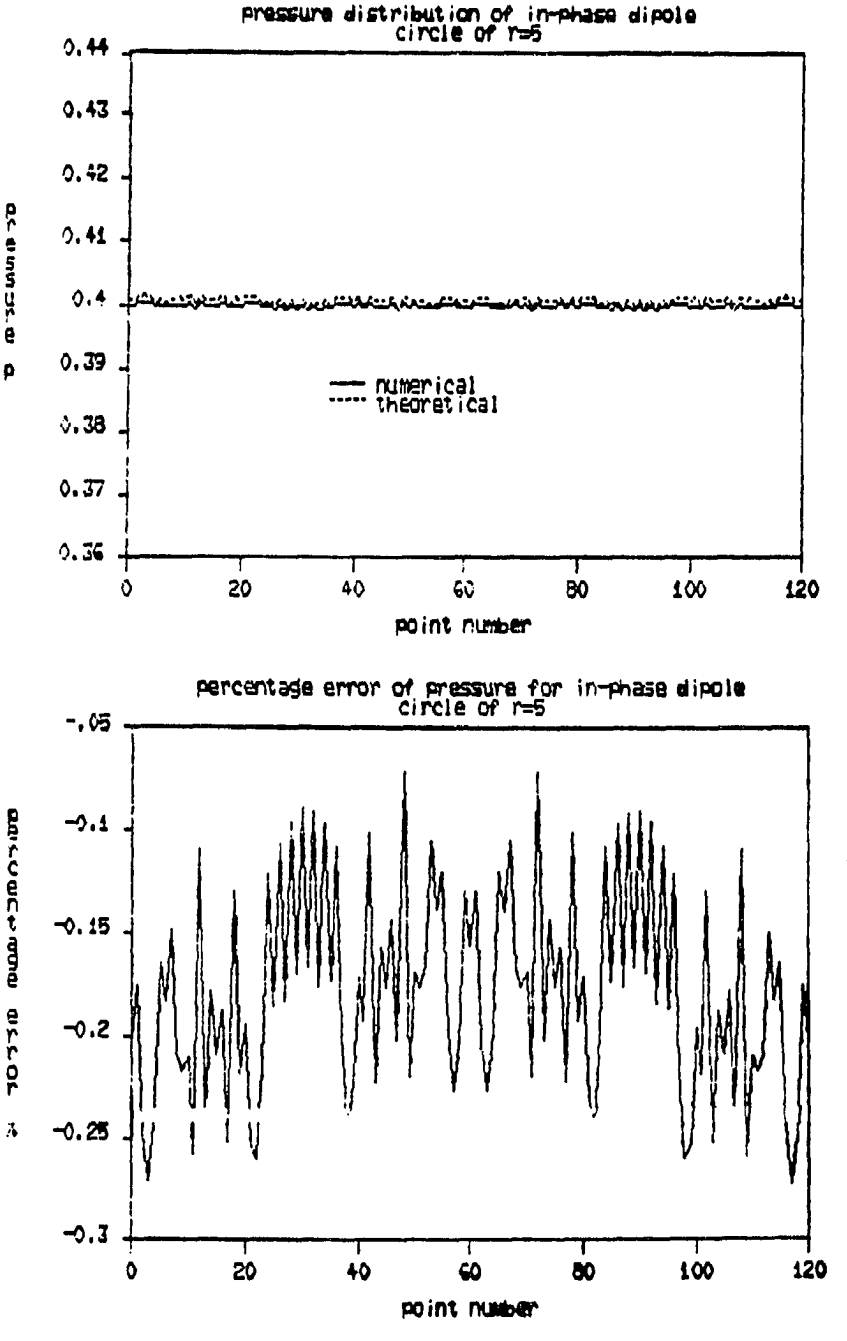


Figure 2.29: Pressure along half circle of $r = 5a$ on yz-plane from two in-phase spheres. top: pressure magnitude distribution, bottom: percentage error

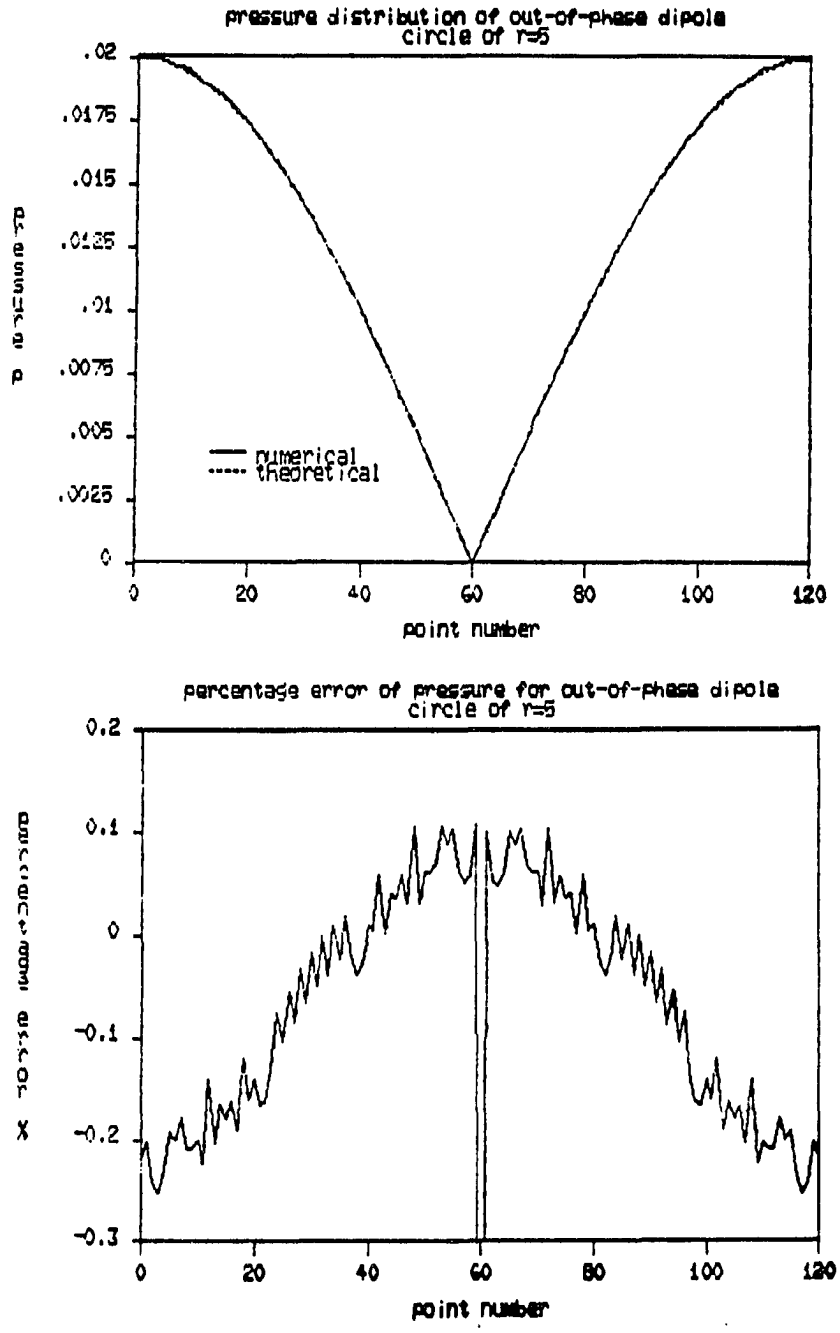


Figure 2.30: Pressure along half circle of $r = 5a$ on yz-plane from two out-of-phase spheres. top: pressure magnitude distribution, bottom: percentage error

cases. No more than 3 % of error is observed. Thus, it is concluded that the BEM simulation predicts the acoustic radiation accurately in all cases shown above regardless of whether the domain of interest is a free or half space.

### 2.3.8 Source monitoring surface

Besides the numerical test cases mentioned above, the validity of using a source monitoring surface to substitute for the actual source (e.g., useful for non-accessible source surface) was also investigated. A baffled piston was used as the actual source because the analytical solution was obtained in the previous section. The configuration of this numerical test was shown in Figure 2.31. The idea behind this test was to use a fictitious source in representing the actual source radiation. This approach might be useful when a source surface is not easily accessible or boundary conditions are difficult to identify. The procedure for this test was as follows:

1. Use a baffled piston with uniform surface velocity to predict the acoustic pressure or normal velocity over the surface of the fictitious source which enclosed the piston.

2. Take the fictitious source to be the sound radiating source with the boundary condition calculated in previous step.

3. Calculate the acoustic field at any point outside the fictitious source surface.

4. Compare the acoustic field calculated in step (3) with the theoretical solution at the same locations.

Two surfaces, a cylinder and a hemisphere, were used as source monitoring surfaces in this numerical test as shown in Figure 2.31. Figures 2.32 and 2.33 show

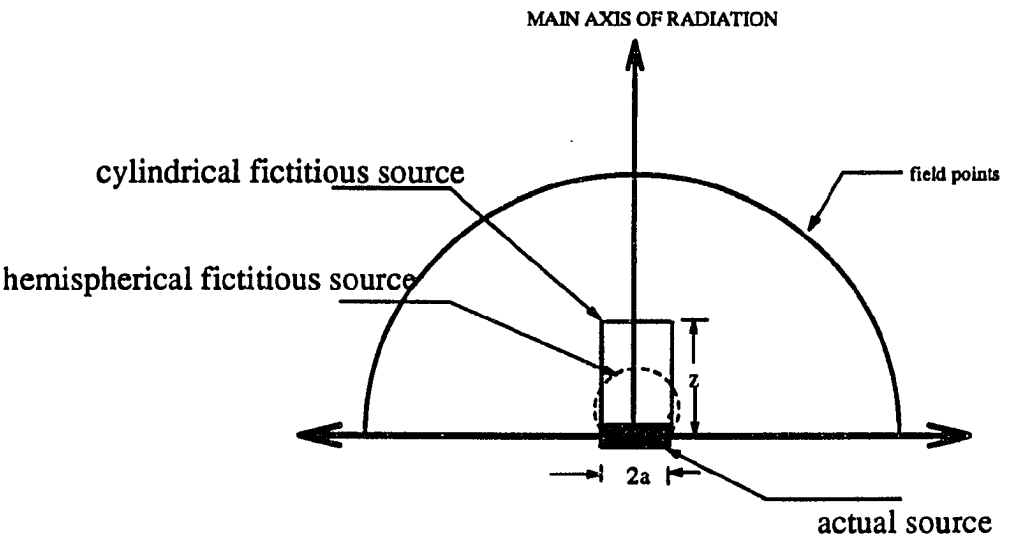


Figure 2.31: Configuration of actual and fictitious sources

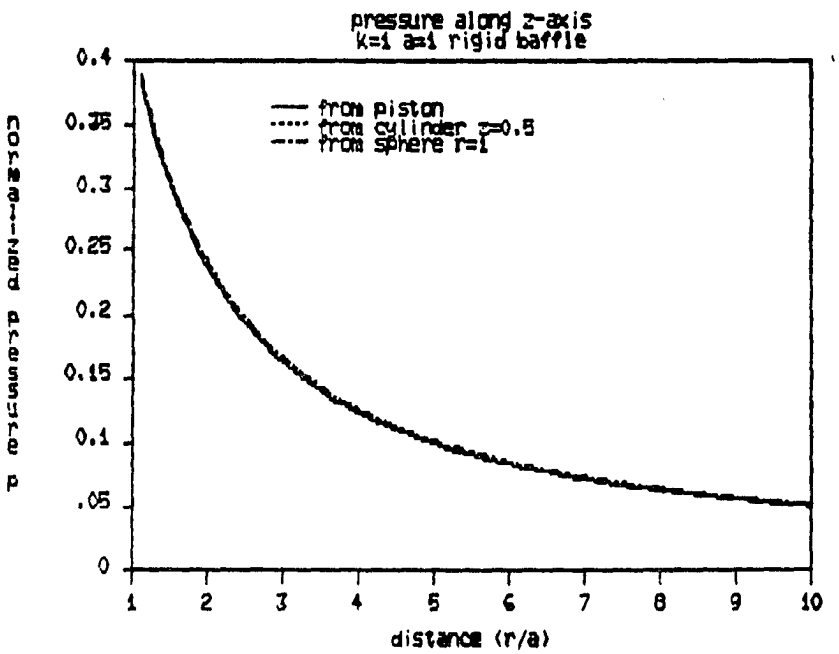


Figure 2.32: On axis pressure magnitude from actual and fictitious sources at $ka = 1$

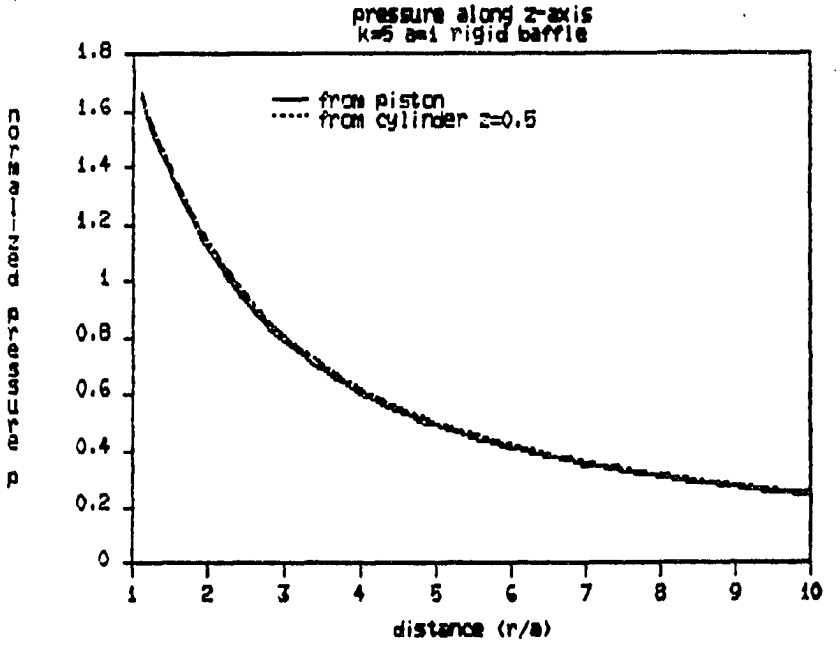


Figure 2.33: On axis pressure magnitude from actual and fictitious sources at $ka = 5$

the theoretical results along the z-axis for cylindrical and hemi-spherical fictitious sources for $ka = 1$ and $ka = 5$ ,respectively. Almost identical results were found for the three sources for both cases. Figures 2.34 and 2.35 present the acoustic pressure for the same configuration along the x-axis. Excellent agreement is observed among the results for the theoretical and fictitious sources except a few minor discrepancies occur when a hemi-spherical surface is used. It can then be concluded that the source monitoring surface performs satisfactorily in predicting the acoustic radiation from the actual source regardless the geometry of the fictitious source being used.

The effect of the size of the fictitious source was investigated as well. The baffled piston was used again as the actual source. The cylinders enclosed the piston with various height from $z = 0.2$ to $z = 2.0$ being tested. Figure 2.36 indicates the acoustic pressure magnitude along the z-axis for various configurations. It was found in Figure 2.37 that the error is no more than $\pm 1.5\%$ for different sizes of cylinders when compared with theoretical solution.

According to the results shown above, an inspiring conclusion can be drawn that the fictitious source can be used with confidence when either the surface of the actual source is not accessible or the boundary conditions on the source surface are difficult to determine. In addition, the fictitious source predicts the acoustic radiation accurately regardless the geometry and size of the fictitious source being used.

## 2.4 Discussion

The BIE formulation as well as BEM numerical scheme were developed and tested in this Chapter for various acoustic radiation problems. In addition, a half space Green's function satisfying mixed boundary condition of finite impedance was

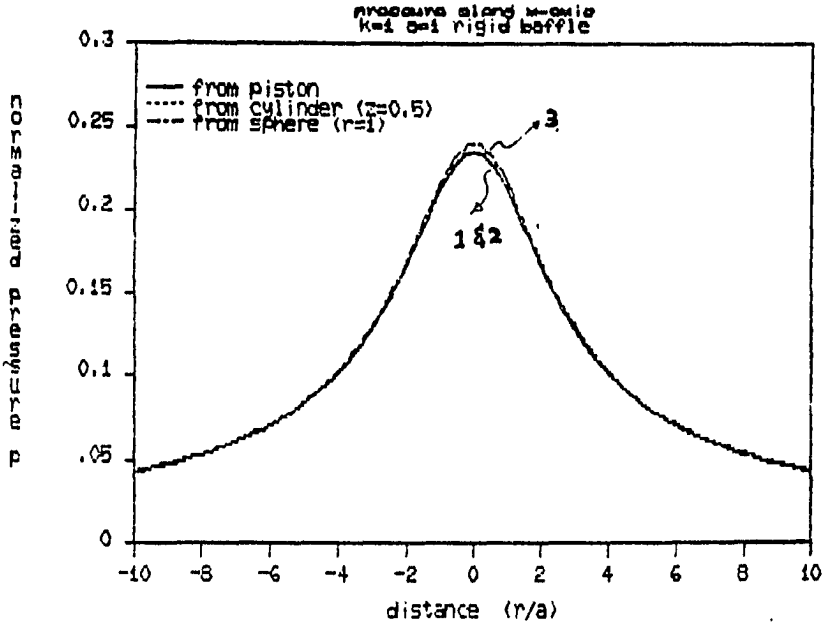


Figure 2.34: Off axis pressure magnitude from actual and fictitious sources at $ka = 1$

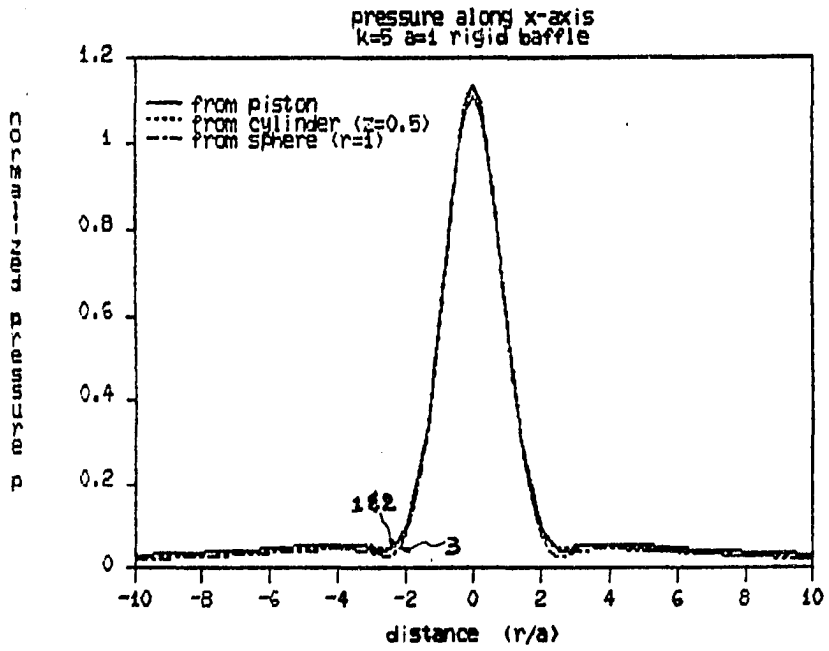


Figure 2.35: Off axis pressure magnitude for actual and fictitious sources at $ka = 5$

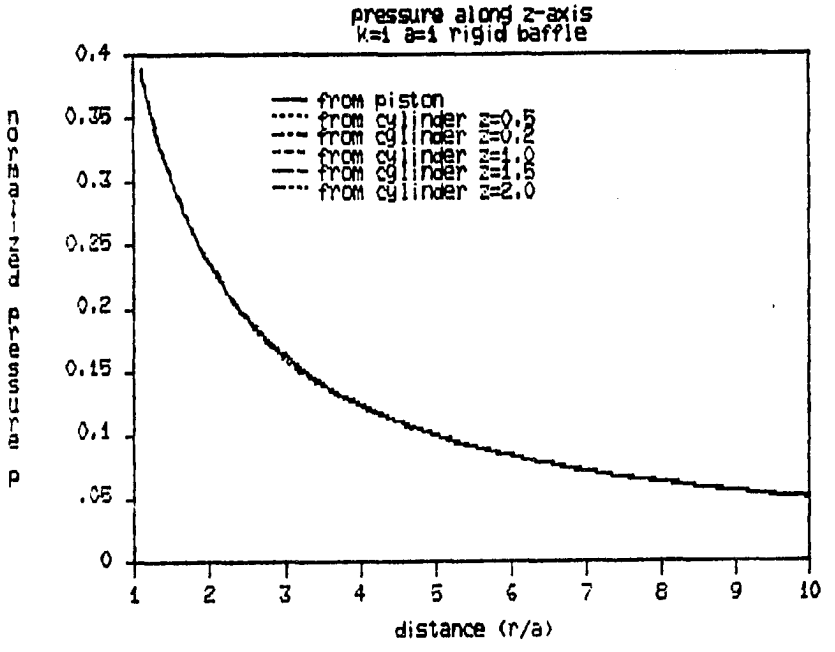


Figure 2.36: On axis pressure magnitude from fictitious sources with various sizes of cylinders

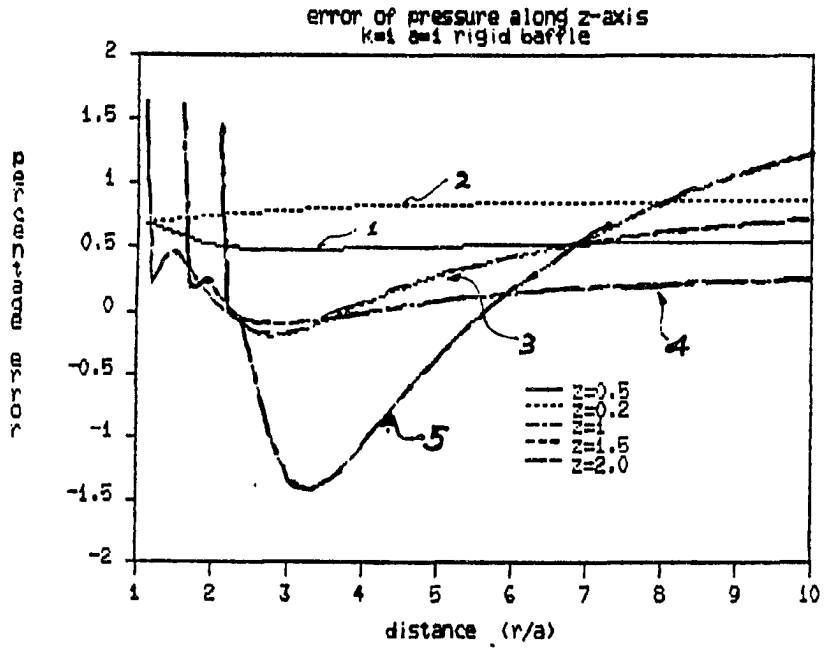


Figure 2.37: Percentage error for on axis pressure magnitude from fictitious sources with various sizes of cylinders

derived and implemented in BEM calculations of acoustic problems of interest. The surface integral was transformed into a set of complex algebraic equations via discretizing the surface of the source into surface elements. The matrix form of the set of the equations was solved by LINPACK [24] routines.

A set of numerical test cases were performed to verify the BIE formulation as well as the half space Green's function. It is proven that the BEM scheme gave accurate predictions for acoustic radiation patterns for various source geometries and boundary conditions in both free and half space. The validity of fictitious source was also justified for hard-to-reach surface of sound source. Therefore, the application of BIE/BEM formulation to acoustic radiation problems is verified.

# 3. NOISE CANCELLATION BY BEM IN HALF SPACE

Noise cancellation in a region of interest is attempted after the acoustic radiation pattern from the noise source inside the domain is identified. A number of secondary sources are added inside the domain such that the inverse of the sound wave from the primary source is produced. Consequently, the acoustic field will ideally be silenced inside the region. However, according to Huygen's principle, an infinite number of perfect point sources have to be used along Huygen's surface. This ideal assumption is not only impractical to implement on a digital computer but also impossible to apply in the real world. Therefore, a compromise has to be made. The best approach is to use the minimum number of practical secondary sources placed at the best locations such that optimal noise cancellation over a pre-selected region can be obtained. In this chapter, one must also calculate proper excitation functions of the secondary sources.

The BEM technique is applied to accomplish this goal. The addition of secondary sources results in a multi-connected domain, but that does not cause any potential difficulty for BEM. However, there are too many parameters involved in active noise cancellation. For example, the acoustic field inside the domain depends on the number of secondary sources being added, the locations and sizes of the secondary sources, the excitation functions for each individual secondary source, the size and location of the

region where noise reduction is required, and the maximum noise reduction required over the region. Some of the parameters will lead to solving nonlinear equations which is beyond the scope of this research. Therefore, the effort is focused on the relationship among these parameters without going into the nonlinear nature of the boundary value problems when BEM is applied. In order to achieve this goal, the surface velocity of the secondary sources are kept uniform and their size is specified. Directivity tests were performed to determine the minimum number of secondary sources required for optimal noise reduction over a specified area. The locations of the secondary sources and the region of noise cancellation serve as variables for each numerical simulation. Consequently, the BEM scheme gives the driving functions, which is the uniform surface velocity, for each secondary sources, the best region of noise cancellation and the maximum noise cancellation for the configuration specified. A data bank is thus established for quick reference when noise reduction is required in certain areas. It should be noted that the noise cancellation technique is based on single frequency excitation. The data bank will have to be set up for different frequencies if it is desired.

## 3.1 Iterative Control Method

The secondary sources are placed inside the domain of interest to achieve noise reduction over a prescribed region. The number, size and locations of secondary sources are fixed. The integration surface now includes both the surfaces of primary and secondary sources and all of these surfaces are discretized. The BEM scheme described in the previous chapter is then applied to achieve noise reduction over a desired region.

Suppose that the primary source is discretized into $n_p$ nodes and $m_p$ surface elements, and the secondary sources are discretized into $n_s$ nodes and $m_s$ surface elements. Following the numerical approximation for BEM scheme, a set of complex algebraic equations are obtained. The matrix form of the BIE becomes

$$[a]_{n*n}\{\phi\}_{n*1} + [b]_{n*n}\left\{\frac{\partial\phi}{\partial n}\right\}_{n*1} = \{0\}_{n*1} \tag{3.1}$$

where $n = n_p + n_s$.

In addition, suppose that the region of noise cancellation is represented by $n_f$ points outside the sources. The BIE formulation for these field points will be

$$[A]_{n_f*n}\{\phi\}_{n*1} + [B]_{n_f*n}\left\{\frac{\partial\phi}{\partial n}\right\}_{n*1} = \{y\}_{n_f*1} \tag{3.2}$$

where $\{y\}$ are the acoustic velocity potential at the field points.
Ideally, $\{y\}$ should be a null vector if perfect noise cancellation is achieved. However, it is impossible to obtain ideal cancellation when a finite number of secondary sources are used. Therefore, it is desired that $\{y\}$ be minimized. It is noted that matrices [a], [b], [A] and [B] remain unchanged as long as the discretization and numerical approximation of both primary and secondary sources are kept unchanged. In addition, part of $\{\phi\}$ and/or $\left\{\frac{\partial\phi}{\partial n}\right\}$ are known from the boundary condition of the primary source. Therefore, the task of noise cancellation becomes the determination of $\{\phi\}$ and $\left\{\frac{\partial\phi}{\partial n}\right\}$ for secondary sources which will minimize $\{y\}$.

As an example, suppose that $\left\{\frac{\partial\phi}{\partial n}\right\}$ is specified over the primary source. Consequently, the first $n_p$ terms in $\left\{\frac{\partial\phi}{\partial n}\right\}_{n*1}$ are known. However, the remaining part of $\left\{\frac{\partial\phi}{\partial n}\right\}$, namely, $\left\{\frac{\partial\phi}{\partial n}\right\}_{n_s*1}$ and $\{\phi\}_{n*1}$ are still unknown. It is known from equation (3.1) that

$$[a]_{n*n}\{\phi\}_{n*1} = -[b]_{n*n}\left\{\frac{\partial\phi}{\partial n}\right\}_{n*1}$$

or

$$\{\phi\}_{n*1} = -[a]^{-1}_{n*n}[b]_{n*n}\left\{\frac{\partial\phi}{\partial n}\right\}_{n*1} \tag{3.3}$$

Furthermore, the four geometry matrices $[a]$, $[b]$, $[A]$ and $[B]$, and the vectors $\{\phi\}$ and $\left\{\frac{\partial\phi}{\partial n}\right\}$ are partitioned in the following manner.

$$[a]_{n*n} = \left[[a_1]_{n*n_p} \quad [a_2]_{n*n_s}\right]$$

$$[b]_{n*n} = \left[[b_1]_{n*n_p} \quad [b_2]_{n*n_s}\right]$$

$$[A]_{n_f*n} = \left[[A_1]_{n_f*n_p} \quad [A_2]_{n_f*n_s}\right]$$

$$[B]_{n_f*n} = \left[[B_1]_{n_f*n_p} \quad [B_2]_{n_f*n_s}\right]$$

$$\{\phi\}_{n*1} = \left\{\begin{array}{c}\{\phi_1\}_{n_p*1}\\ \{\phi_2\}_{n_s*1}\end{array}\right\}$$

$$\left\{\frac{\partial\phi}{\partial n}\right\}_{n*1} = \left\{\begin{array}{c}\left\{\frac{\partial\phi_1}{\partial n}\right\}_{n_p*1}\\ \left\{\frac{\partial\phi_2}{\partial n}\right\}_{n_s*1}\end{array}\right\}$$

Therefore, the BIE becomes

$$[[a_1] \quad [a_2]]\left\{\begin{array}{c}\{\phi_1\}\\ \{\phi_2\}\end{array}\right\} + [[b_1] \quad [b_2]]\left\{\begin{array}{c}\left\{\frac{\partial\phi_1}{\partial n}\right\}\\ \left\{\frac{\partial\phi_2}{\partial n}\right\}\end{array}\right\} = \{0\}$$

or

$$\left\{\begin{array}{c}\{\phi_1\}\\ \{\phi_2\}\end{array}\right\} = -[[a_1] \quad [a_2]]^{-1}[[b_1] \quad [b_2]]\left\{\begin{array}{c}\left\{\frac{\partial\phi_1}{\partial n}\right\}\\ \left\{\frac{\partial\phi_2}{\partial n}\right\}\end{array}\right\} \tag{3.4}$$

For simplicity, equation (3.4) is expressed in matrix form as follows.

$$\left\{\begin{array}{c}\{\phi_1\}\\ \{\phi_2\}\end{array}\right\} = \left[\begin{array}{cc}[G_1] & [G_2]\\ [G_3] & [G_4]\end{array}\right]\left\{\begin{array}{c}\left\{\frac{\partial\phi_1}{\partial n}\right\}\\ \left\{\frac{\partial\phi_2}{\partial n}\right\}\end{array}\right\} \tag{3.5}$$

Similarly, the field equation is expressed into sub-matrix form which separates the variables corresponding to the field points on primary and secondary sources.

$$[[A_1] \quad [A_2]] \begin{Bmatrix} \{\phi_1\} \\ \{\phi_2\} \end{Bmatrix} + [[B_1] \quad [B_2]] \begin{Bmatrix} \left\{\frac{\partial \phi_1}{\partial n}\right\} \\ \left\{\frac{\partial \phi_2}{\partial n}\right\} \end{Bmatrix} = \{y\} \tag{3.6}$$

The expression of $\begin{Bmatrix} \{\phi_1\} \\ \{\phi_2\} \end{Bmatrix}$ from equation (3.5) is substituted into equation (3.6).

Therefore, the field velocity potential $\{y\}$ is expressed in terms of $\begin{Bmatrix} \left\{\frac{\partial \phi_1}{\partial n}\right\} \\ \left\{\frac{\partial \phi_2}{\partial n}\right\} \end{Bmatrix}$ as

$$\{y\} = [[A_1] \quad [A_2]] \begin{bmatrix} [G_1] & [G_2] \\ [G_3] & [G_4] \end{bmatrix} \begin{Bmatrix} \left\{\frac{\partial \phi_1}{\partial n}\right\} \\ \left\{\frac{\partial \phi_2}{\partial n}\right\} \end{Bmatrix} + [[B_1] \quad [B_2]] \begin{Bmatrix} \left\{\frac{\partial \phi_1}{\partial n}\right\} \\ \left\{\frac{\partial \phi_2}{\partial n}\right\} \end{Bmatrix}$$

$$= [[A_1G_1 + A_2G_3 + B_1] \quad [A_1G_2 + A_2G_4 + B_2]] \begin{Bmatrix} \left\{\frac{\partial \phi_1}{\partial n}\right\} \\ \left\{\frac{\partial \phi_2}{\partial n}\right\} \end{Bmatrix} \tag{3.7}$$

That is to say

$$\{y\}_{n_f * 1} = [A_1G_1 + A_2G_3 + B_1]_{n_f * n_p} \left\{\frac{\partial \phi_1}{\partial n}\right\}_{n_p * 1}$$

$$+ [A_1G_2 + A_2G_4 + B_2]_{n_f * n_s} \left\{\frac{\partial \phi_2}{\partial n}\right\}_{n_s * 1} \tag{3.8}$$

It is noted that $\left\{\frac{\partial \phi_1}{\partial n}\right\}$ are known boundary conditions from the primary source. Therefore, it is desired to choose $\left\{\frac{\partial \phi_2}{\partial n}\right\}$ properly such that the field velocity potential $\{y\}$ is minimized.

The iterative control block diagram for the minimization process is shown in

Figure 3.1. It is noticed that the substitution of

$$-\left[[a_1] \quad [a_2]\right]^{-1}\left[[b_1] \quad [b_2]\right] = \begin{bmatrix} [G_1] & [G_2] \\ [G_3] & [G_4] \end{bmatrix}$$

is used in the diagram. The transfer functions $G_1$, $G_2$, $G_3$, $G_4$, $A_1$, $A_2$, $B_1$, and $B_2$ are geometry dependent and remain unaffected. In addition, $\left\{\frac{\partial \phi_1}{\partial n}\right\}$ are known. Therefore, the output $\{y\}$ is fed back through the feed-back transfer function S to modify the variable $\left\{\frac{\partial \phi_2}{\partial n}\right\}$ in order to minimize $\{y\}$. From the block diagram, the iterative representation of $\left\{\frac{\partial \phi_2}{\partial n}\right\}$ is

$$\left\{\frac{\partial \phi_2}{\partial n}\right\}_{k+1} = \left\{\frac{\partial \phi_2}{\partial n}\right\}_k + S\left(y_{ref} - y_k\right). \tag{3.9}$$

It is clear in the diagram that

$$d_k = \left\{\frac{\partial \phi_2}{\partial n}\right\}_k - S y_k,$$

and

$$y_k = \left(A_1 G_1 + A_2 G_3 + B_1\right)\left\{\frac{\partial \phi_1}{\partial n}\right\}_k + \left(A_1 G_2 + A_2 G_4 + B_2\right) d_k.$$

Therefore,

$$d_k = \frac{\left[y_k - \left(A_1 G_1 + A_2 G_3 + B_1\right)\left\{\frac{\partial \phi_1}{\partial n}\right\}_k\right]}{\left(A_1 G_2 + A_2 G_4 + B_2\right)}$$

and

$$\begin{aligned}\left\{y_k\right\} = & \frac{\left(A_1 G_1 + A_2 G_3 + B_1\right)}{1 + S\left(A_1 G_2 + A_2 G_4 + B_2\right)}\left\{\frac{\partial \phi_1}{\partial n}\right\}_k \\ & + \frac{\left(A_1 G_2 + A_2 G_4 + B_2\right)}{1 + S\left(A_1 G_2 + A_2 G_4 + B_2\right)}\left\{\frac{\partial \phi_2}{\partial n}\right\}_k\end{aligned} \tag{3.10}$$

Consequently, if the feed-back transfer function S is so chosen that

$$S = \left[A_1 G_2 + A_2 G_4 + B_2\right]^{-1}.$$

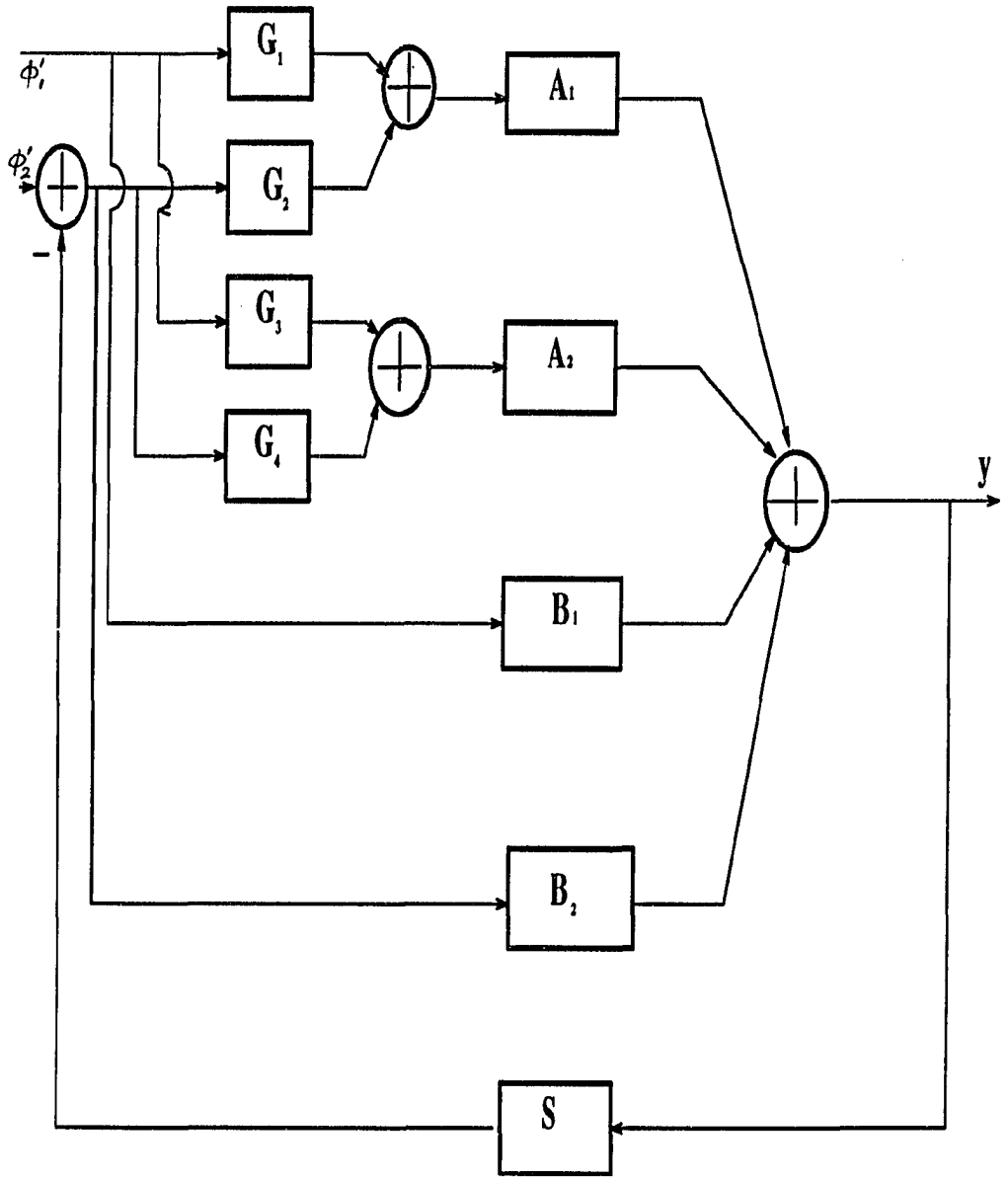


Figure 3.1: Closed loop feed back diagram for iterative control method

The output of each iteration will be

$$y_{k+1} = y_k + \frac{1}{2}\left(y_{ref} - y_k\right) = \frac{1}{2}\left(y_{ref} + y_k\right).$$

From the above equation it is obvious that the output from this iterative control system will be cut to half of its original value after each iteration. That is, after n iterations

$$y_{n+1} = \frac{1}{2^n} y_1.$$

It should be noted that $\{y\}$ is an $n_f * 1$ complex array. Therefore, the $l_2$ norm of $\{y\}_{n_f * 1}$ is calculated and minimized. That is the velocity potentials at the $n_f$ field points are minimized all together instead of considering one field point at a time.

Ideally, even though the output $\{y\}$ can be mathematically minimized to an infinitesimally small value after a sufficiently large number of iterations, the numerical and truncation errors from the digital computer interfere with the process. Consequently, an absolute silence inside the designated region cannot be achieved, and an error bound should be set beforehand such that the feed back mechanism will not step into an infinite loop operation in the numerical simulations.

## 3.2 Coupled Equation Method

Following the procedures described in previous section, the BEM scheme comes up with two system of equations: BIE (equation (3.1))and field equation (equation (3.2)). It is clearly that the field velocity potential $\{y\}$ depends totally on nodal values of $\{\phi\}$ and $\left\{\frac{\partial \phi}{\partial n}\right\}$ which are determined by BIE equation. Therefore, the two system of equations are coupled to each other. In addition, the field velocity potentials in equation (3.2) are forced to be zero over the specified field points (which

indicates perfect noise cancellation everywhere). Those two system of equations are thus combined into a single set of complex algebraic equations which corresponds to perfect noise cancellation within the region of interest.

It is again assumed that the normal derivative of velocity potential $\left\{\frac{\partial\phi_1}{\partial n}\right\}$ is specified over the surface of the primary source. The four coefficient matrices obtained from the geometry of both primary and secondary sources in BIE and field equations are partitioned with the same manner described in the previous section. Consequently, equations (3.5) and (3.6) are obtained. It should be noted that $\{y\}$ is forced to be zero in this case. Upon imposing the boundary condition, $\left\{\frac{\partial\phi_1}{\partial n}\right\}$ on the primary source is a known array. Nevertheless, there exist three unknown arrays $\left\{\frac{\partial\phi_2}{\partial n}\right\}$ on secondary sources and $\{\phi\}$ on both primary and secondary sources. It is shown in equation (3.5) that the unknowns $\{\phi\}$ on both primary and secondary sources can be expressed in terms of $\left\{\frac{\partial\phi}{\partial n}\right\}$ on the sources via BIE. Consequently, the field equation is simplified into one unknown array $\left\{\frac{\partial\phi_2}{\partial n}\right\}$ on the secondary sources with a set of complex algebraic equations when the field velocity potential $\{y\}$ is forced to be zero. That is

$$\{y\}_{nf*1} = \begin{bmatrix} [A_1G_1 + A_2G_3 + B_1]_{nf*np} \\ [A_1G_2 + A_2G_4 + B_2]_{nf*ns} \end{bmatrix}^T \begin{Bmatrix} \left\{\frac{\partial\phi_1}{\partial n}\right\}_{np*1} \\ \left\{\frac{\partial\phi_2}{\partial n}\right\}_{ns*1} \end{Bmatrix}$$

$$= \begin{bmatrix} [E_1]_{nf*np} & [E_2]_{nf*ns} \end{bmatrix} \begin{Bmatrix} \left\{\frac{\partial\phi_1}{\partial n}\right\}_{np*1} \\ \left\{\frac{\partial\phi_2}{\partial n}\right\}_{ns*1} \end{Bmatrix} = \{0\}_{nf*1} \qquad (3.11)$$

Therefore, the field equation becomes

$$[E_1]\left\{\frac{\partial\phi_1}{\partial n}\right\} + [E_2]\left\{\frac{\partial\phi_2}{\partial n}\right\} = \{0\}$$

or

$$[E_2]\left\{\frac{\partial\phi_2}{\partial n}\right\} = -[E_1]\left\{\frac{\partial\phi_1}{\partial n}\right\} \tag{3.12}$$

It is noticed that $[E_1]$ and $[E_2]$ are determined from the geometry of primary and secondary sources which remain unchanged as long as the discretization and approximation of nodal coordinates in BEM are accomplished. In addition, $\left\{\frac{\partial\phi_1}{\partial n}\right\}$ is known from the boundary condition on the primary source. Therefore, the field equation is further simplified to a set of linear complex algebraic equations in the well-known form of $Ax = b$. In this case $A = [E_2]$, $x = \left\{\frac{\partial\phi_2}{\partial n}\right\}$, and $b = -[E_1]\left\{\frac{\partial\phi_1}{\partial n}\right\}$ which is a known array.

A number of routines exist for the solution of the simultaneous linear equations. However, LINPACK [24] routines are used to complete the work. Ideally, the solution of the above equation should return zero field velocity potentials at the field points specified in field equation. However, it should be realized that complete cancellation at discrete nodal points in a zone does not necessarily imply complete silence in the zone. Furthermore, ideal noise cancellation is impossible to achieve due to numerical as well as truncation errors in the computation of the solution when a digital computer is used. Therefore, minimization of the errors in the solution is necessary.

Suppose the true solution for the system of equation is x, and the solution returned by the digital computer is $\hat{x}$. Therefore

$$x = \hat{x} + \varepsilon. \tag{3.13}$$

where $\varepsilon$ is the error array.

Consequently, the field equation becomes

$$A(\hat{x} + \varepsilon) = b \tag{3.14}$$

and

$$A\varepsilon = b - A\hat{x} = R \tag{3.15}$$

where R is the residue array. A closed loop feedback system is set up as shown in the block diagram of Figure 3.2. It is clear that the residue array can be minimized mathematically if the feed back transfer function is properly chosen. A choice of the feed back transfer function S will be $S = A^{-1}$. The residue array then becomes

$$R_{i+1} = \frac{b - A\hat{x}}{1 + SA} = \frac{1}{2}R_i. \tag{3.16}$$

This equation indicates that the residue array will become half of its original value after each iteration. Therefore, the error array $\varepsilon$ will become negligibly small after a sufficiently large number of iterations.

## 3.3 Numerical Evaluation of Noise Cancellation Technique

Although the noise cancellation techniques described in the previous two sections perform well mathematically, two major difficulties appear when numerical simulation of the technique is implemented. First of all, ill-conditioned matrices are encountered due to the specification of field points. Secondly, both techniques are almost impossible to apply to real world situations without proper modifications. These difficulties are discussed in detail in this section. Numerical implementations to avoid these difficulties are described as well.

### 3.3.1 Ill-conditioned matrices

The condition number of a matrix is an index to indicate whether the matrix is a well-conditioned matrix or not. In fact, the condition number is a quantity which

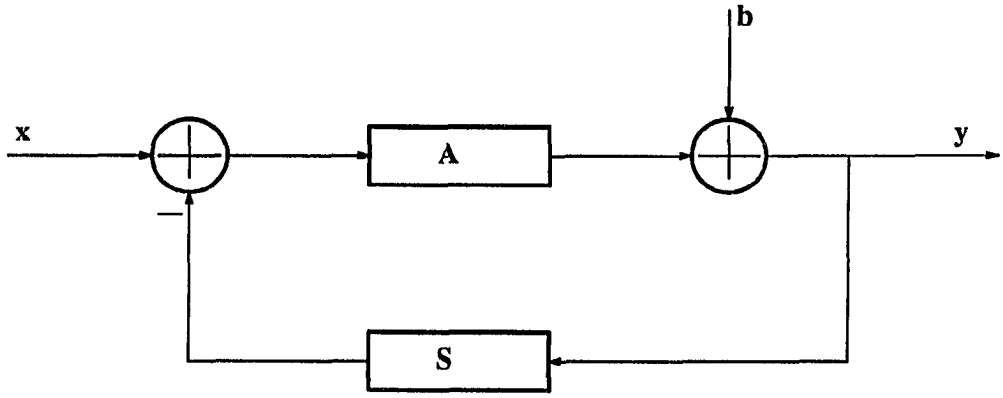


Figure 3.2: Closed loop feed back diagram for coupled equation method

measures the sensitivity of the solution $\mathbf{x}$ to errors in the elements of matrix $\mathbf{A}$ and the array $\mathbf{b}$ on the right hand side of the equation $\mathbf{Ax} = \mathbf{b}$. If the relative error in $\mathbf{A}$ is of size $\epsilon$, the resulting relative error in solution $\mathbf{x}$ can be as large as $\kappa(A)\,\epsilon$, where $\kappa(A)$ is the condition number of matrix $\mathbf{A}$ . If the condition number of matrix $\mathbf{A}$ is approximately on the order of $10^d$, the elements of solution $\mathbf{x}$ is expected to have d fewer significant figures of accuracy than the elements of matrix $\mathbf{A}$ . Consequently, if the condition number is too large, the solution may have no significant figure at all. That is to say that the solution is not reliable. Therefore, the condition number of matrix $\mathbf{A}$ is desired to be as small as possible. The definition of condition number [25] is

$$\kappa(A) = \|A\|\|A^{-1}\| \tag{3.17}$$

where $\|A\|$ denotes the Euclidean matrix norm of A. Therefore, the minimum value of $\kappa(A)$ is 1.

The ill-conditioned matrices usually occur in the field equation $[a]\{\phi\}+[b]\left\{\frac{\partial\phi}{\partial n}\right\} = \{y\}$. Each field point in the noise cancellation region contributes one equation to this system of linear algebraic equations. The kernel of the integral equation shown in equation (2.32) depends on the distance between field points and nodal points on the surface of the sources r. Consequently, the matrices in equations (3.8) and (3.12) become ill-conditioned when the field points are specified too close to each other. Any two closely specified field points will lead to two equations in the system of equations which are almost linearly dependent. This results in a very large condition number.

However, a few numerical experiments with the present algorithm suggest that it is possible to avoid situations involving severely ill-conditioned matrices without sacrificing too much in our goal of noise cancellation. When the cancellation of noise

is demanded at a field point, by setting the corresponding element of $\{y\}$ to zero, significant reduction in noise is achieved not just at a point but over a finite sized region in the neighborhood of the point. Therefore, the field points need not be very closely specified. The suitable spacing between the field points can be obtained through a senses of lengthy numerical experiments. Such numerical experiments are performed with the goal of arriving at a compromise between two undesirable situations. On one hand, too sparsely placed field points give a matrix with good condition number, but non-uniform and insignificant noise reduction. On the other hand, too closely placed field points will probably give excellent noise reduction, but the problem is unsolvable due to the severe ill-conditioning of the matrix. Since, we do not want to sacrifice much in our goal of noise reduction, we will place the field points at the "minimum" level of sparsity. In such a situation, the condition number will be somewhat reduced but still remains significantly large. This problem involving a matrix with large condition number is solved by using two well known numerical techniques, namely, the regularization method [26] and the singular-value-decomposition (SVD) method [26].

**3.3.1.1 Regularization method** The now familiar matrix form of the system of equations $\mathbf{Ax} = \mathbf{b}$ is considered. The matrix $\mathbf{A}$ is usually not a square matrix. Hence, for the solution of the equation, the equation is multiplied by transpose of matrix A as

$$\mathbf{A^T Ax} = \mathbf{A^T b}. \tag{3.18}$$

The coefficient matrix $A^T A$ is now a symmetric square matrix. The normal Gaussian elimination can then be applied to solve the system of equations. It should be noted

that the procedure described above tends to square the condition number of the original matrix which makes the problem even worse. The near singularity of the coefficient matrix is removed in the regularization method by modifying the equation to

$$\left[A^T A + \alpha I\right] \{x\} = \left\{A^T b\right\} \tag{3.19}$$

where $\alpha$ is a pre-selected small quantity, and I is the identity matrix. Theoretically, it is desirable that $\alpha$ be as small as possible such that the solution will not be affected too much. Nevertheless, too small $\alpha$ added to the diagonal terms of an ill-conditioned matrix is not sufficient to obtain a well-conditioned matrix. Therefore, the size of $\alpha$ must be determined by a trial-and-error process. The regularized matrix is then decomposed by standard routines such as Gaussian elimination. The solution of the system of linear equations is then achieved accordingly.

**3.3.1.2 SVD method** The SVD method applies the technique of singular value decomposition to the original non-square matrix. A set of singular values as well as two orthogonal square matrices are determined by SVD. The solution is then calculated directly from those matrices and the singular values. For example, the non-square matrix $[A]_{n*p}$ is considered. Theoretically, there exists an $n \times n$ orthogonal matrix U and a $p \times p$ orthogonal matrix V such that $U^T AV$ has one of the following two forms:

$$\begin{cases} U^T AV = \begin{bmatrix} \Sigma \\ 0 \end{bmatrix} & \text{if } n \geq p \\ U^T AV = [\Sigma \quad 0] & \text{if } n \leq p \end{cases} \tag{3.20}$$

where $\Sigma = diag\,(\sigma_1, \sigma_2, ....., \sigma_m)$,

$m = min\,\{n, p\}$, and

$\sigma_1 \geq \sigma_2 \geq ..... \geq \sigma_m \geq 0.$

The scalars $\sigma_1, \sigma_2, ....., \sigma_m$ are called the singular values of matrix A. The columns of U are the left singular vectors of A and the columns of V are the right singular vectors of matrix A. The non-square matrix A is first reduced to a bidiagonal form by means of Household transformation. The bidiagonal matrix is then iteratively reduced to a diagonal form by a variant of the QR algorithm. Consequently, the arrays U,V and the singular values $\Sigma$ are obtained.

Suppose the non-square matrix $[A]_{n*p}$ is judged to be of rank k, it is natural to solve least square problems involving A by setting the last $p-k$ singular values to zero. It is necessary to investigate the sensitivity of the solution calculated by SVD when matrix A is perturbed. The sensitivity of the solution can be identified by the condition number. The condition number for singular value decomposition is defined as follows.

$$\kappa(A) = \frac{\sigma_1}{\sigma_k} \tag{3.21}$$

The relative error [25] for $Ax = b$ is bounded by

$$\frac{\|x_0 - \hat{x}_0\|}{\|x_0\|} \leq 9 \left[\kappa(A) + \kappa(A)^2 \frac{\|r\|}{\|A\|\|x_0\|}\right] \frac{\|E\|}{\|A\|} \tag{3.22}$$

where E is the perturbation of A and E satisfies

$$\sigma_k \geq 10\|E\| > \|E\| > \sigma_{k+1} \tag{3.23}$$

$\|E\|$ is the Euclidean vector norm of E, $x_0$ is the true solution, $\hat{x}_0$ is the solution for A+E, and r is the residue $r = b - Ax$.

It is clear that SVD can be used to calculate solutions to the least square problem in the form of $Ax = b$. It is equally well applied to calculate the pseudo-inverse of a

non-square matrix A. Finally, the solution of $Ax = b$ is determined by

$$x = V\Sigma^{-1}U^T b \tag{3.24}$$

It is noted that the solution obtained by SVD is automatically in the least square sense [24].

**3.3.1.3 Comparison of regularization and SVD methods** The two methods for solving non-square matrix forms of systems of equations were investigated to test their performance. Two dimensional potential problems were used as test cases for simplicity. It was assumed that a number of point sources were distributed over a half circle in a 2-D plane as primary sources. A set of secondary point sources were used over another half circle outside the primary sources to cancel the noise at selected field points. The configuration of the test is shown in Figure 3.3. The condition numbers and residues from each method are listed in Table 3.1 for various numbers of primary sources, secondary sources, and field points. It should be noted that the residue shown in Table 3.1 is in the power of 10. In addition, the number of secondary sources always exceeded that of the primary sources to guarantee noise cancellation at specified field points. It is also noted in Table 3.1 that the condition number for the regularization method increased rapidly with increased number of primary sources. In addition, the residue from regularization increased with the increase of field points when $\alpha = 10^{-5}$ was used. On the other hand, the solution from the SVD method was not affected by the variation of the number of sources and field points being used. The most important part is that the residue from SVD method was always as good as that from regularization method if not better.

It is shown that the SVD method returned more accurate solution in comparison

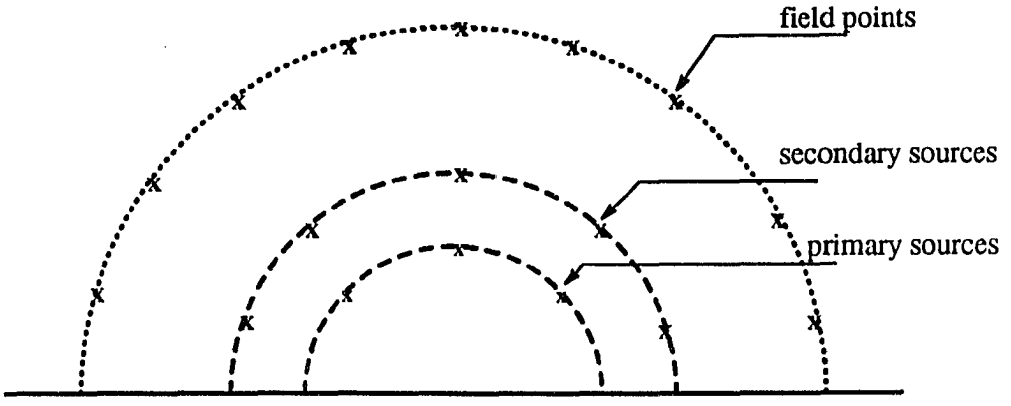


Figure 3.3: Configuration for 2-D potential problems

to the regularization method. However, the SVD method suffered from longer computation time than the regularization method because more matrix operations were involved and iterative reduction of a bidiagonal matrix was used in the QR algorithm. However, the SVD method was chosen in the proceeding numerical work due to the higher accuracy.

Table 3.1: Comparison of regularization and SVD methods by 2-D potential problem

| Case | Np | Ns | Nf | $A^TA$ | COND. NO. | $A^TA$ RES. | SVD | SVD RES. |
|---|---|---|---|---|---|---|---|---|
| 1 | 1 | 2 | 3 | 2*2 | 31.84 | -1 | 3*2 | -1 |
| 2 | 1 | 3 | 3 | 3*3 | 736 | -6 | 3*3 | -7 |
| 3 | 1 | 3 | 11 | 3*3 | 163 | -2 | 11*3 | -2 |
| 4 | 3 | 7 | 21 | 7*7 | 90056 | -3 | 21*7 | -3 |
| 5 | 5 | 11 | 15 | 11*11 | 1.64E+7 | -3 | 15*11 | -5 |
| 6 | 5 | 21 | 21 | 21*21 | 3E+8 | +3 | 21*21 | -6 |
| 7 | 49 | 117 | 121 | 117*117 | 1E+32 | +6 | 121*117 | -5 |

Np: number of primary sources
Ns: number of secondary sources
Nf: number of field points
$A^TA$: matrix dimension of regularization technique
SVD: matrix dimension of singular value decomposition technique
RES: residue in the order of power 10
COND. NO.: condition number, COND. NO.= 1.E+32 indicates singular matrix.

### 3.3.2 Uniform driving function for practical application

The noise cancellation techniques by the iterative control method and the coupled equation method were investigated numerically to justify their applicability to real world situations. A hemi-sphere which was assumed to oscillate radially with uniform normal velocity specified over the surface of the source was used as primary

source. A number of secondary sources were used to cancel the noise level outside the secondary sources. It was found that both iterative control and coupled equation methods return similar results which showed very good noise cancellation at specified field points. As an example, a hemi-sphere of radius 1 m with the center at the origin was used as the primary source. Four spheres with the same radius were symmetrically distributed around the primary source. The field points over a half circle of 10 m radius with center at origin and located on the x-z plane were specified to be the desired region of silence. The configuration of the numerical test condition is shown in Figure 3.4. The noise level at the 121 points uniformly distributed over the half circle were significantly reduced after 36 iterations as shown in Figure 3.5 when iterative control method was applied. However, the residue after each iteration did not reduce to half of its original value which was anticipated from the theoretical derivation. It was known that the feed back transfer function S was not exactly the solution represented in previous sections due to the numerical errors introduced by the digital computer, and in finite arithmetic $S\left(A_1G_2 + A_2G_4 + B_2\right) \neq 1$.

It was also noted that the residue decreased faster in the first few iterations than in later iterations. It happened occasionally that the $l_2$ norm of the residue array increased instead of decreasing after one iteration. In such cases, the feedback quantity $S\left(y_{ref} - y_k\right)$ in equation (3.9) was scaled by a constant before it was added to the original $\left\{\frac{\partial \phi_2}{\partial n}\right\}$. However, the final results satisfied the given error bound which was $\|y\| \leq 10^{-5}$. It should be noted that the $l_2$ norm of $\{y\}$ was calculated, and therefore the acoustic pressure at every point on the half circle should be less than $10^{-5}$ pascal. The coupled equation method gave a very similar solution. It indicated that the solutions for both methods would converge to the same

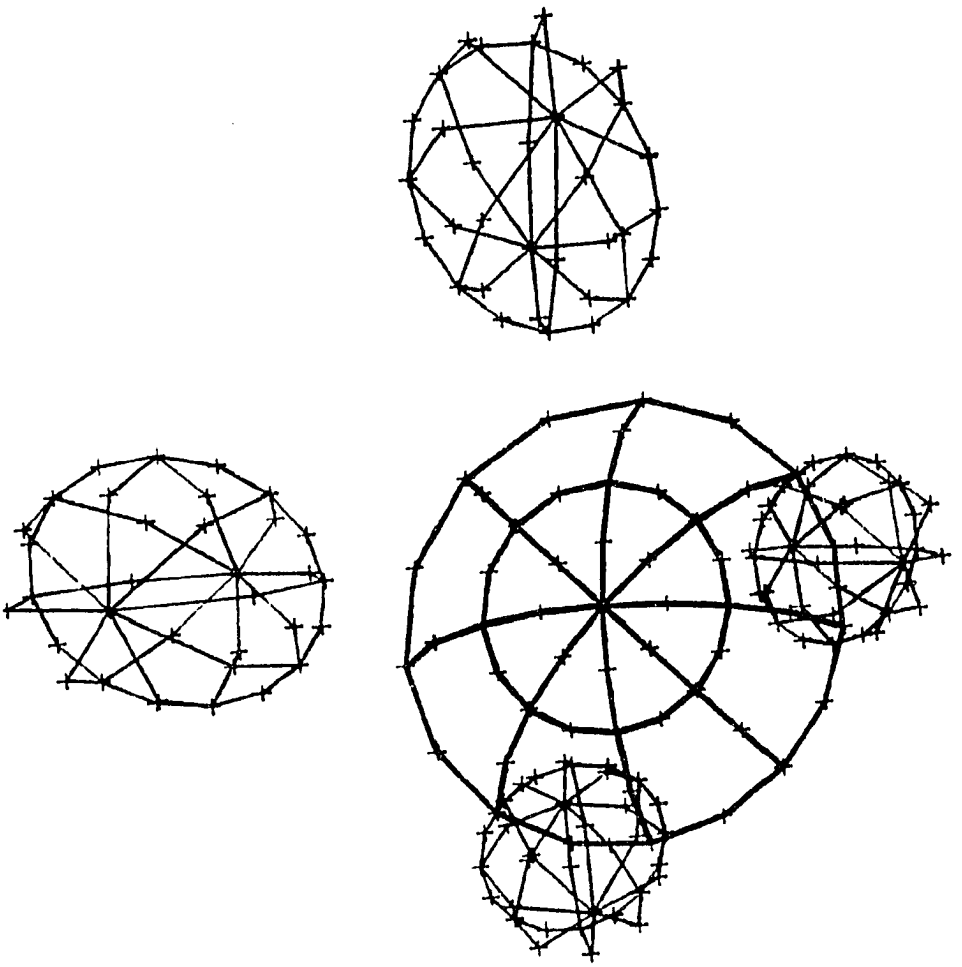

Figure 3.4: The configuration of the numerical test with hemi-sphere primary source and four sphere secondary sources

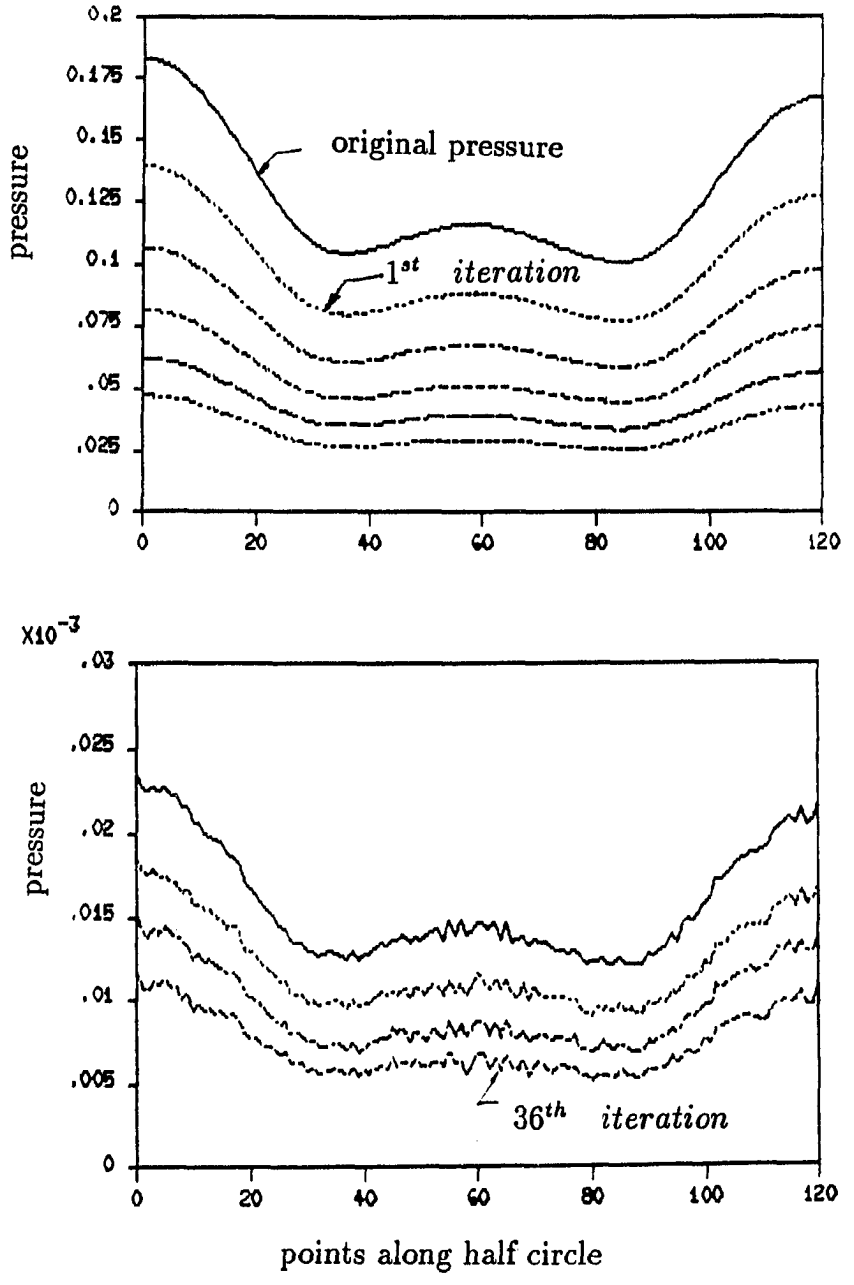


Figure 3.5: The pressure magnitude reduction along a half circle after 36 iterations

results eventually as expected. Even though the two methods performed equally well in noise cancellation, the coupled equation method was preferred because it was more computationally economical compared to the iterative control method.

Despite the success of the noise cancellation techniques shown above, the solution raises a critical question. It was observed that the normal velocity over the secondary sources fluctuated rapidly as shown in Figure 3.6. It was computationally correct that this rapidly varying normal velocity over the surface of the secondary sources would ensure good noise cancellation to near-by field points. However, it is either impossible to find such source in the real world or difficult to generate that specific driving function which would produce the computed surface velocity for the secondary sources. Therefore, the solution obtained was of little use other than numerical simulation. Since, the final goal of this research was to apply the noise cancellation technique to a real world situation, the technique has to be amended for incorporation in practical situations. It was thus assumed that the normal velocity over the surface of each secondary source is uniform. However, the value of such uniform surface velocity could be different for different sources. The amendment of forcing uniformly distributed normal velocity on the surface of each secondary sources significantly reduced the number of unknowns from $N_s$ (total number of nodal points on secondary sources) to $N_{ss}$ (total number of secondary sources). Consequently, the computational cost was reduced dramatically. On the other hand, the noise reduction over the prescribed area was not as good as in the previous case which did not have any constraint on the surface velocity of secondary sources.

According to the constraint on the surface velocity of the secondary sources, $\left\{\frac{\partial \phi_2}{\partial n}\right\}_{n_s*1}$ becomes $\left\{\frac{\partial \phi_2}{\partial n}\right\}_{n_{ss}*1}$, and $[E_2]_{n_f*n_s}$ becomes $[E_2]_{n_f*n_{ss}}$ in equation

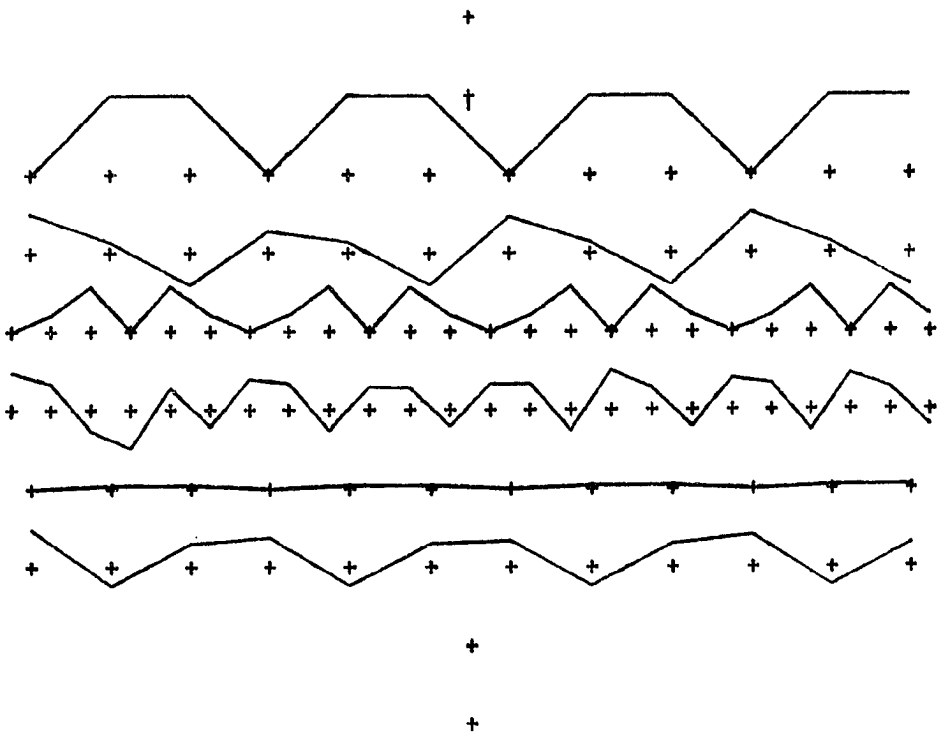

Figure 3.6: The velocity distribution over four sphereical secondary sources without constraint

(3.12). The numerical simulation based on this amendment is performed in order to determine the locations and excitation function for each secondary source when a designated region of noise reduction is specified.

## 3.4 Discussion

Two noise cancellation techniques using the BEM were derived and discussed in this chapter. Although both of them performed well mathematically, some numerical difficulties were encountered. Remedies for avoiding these difficulties are also suggested. It was known after a few numerical simulations that the coupled equation method was computationally more economical than the iterative control method. Nevertheless, both of them returned similar results.

Regularization as well as SVD methods were discussed to solve the problem involving ill-conditioned matrices. The regularization method was more economical in computational cost, however, the solution from it was not reliable when the condition number of the regularized matrix became too large which usually occurred when a large number of field points were specified. Although the SVD method was more time-consuming because of the matrix operations involved, the solution was accurate no matter how many field points were specified. Therefore, the coupled equation method with SVD implementation was used for further numerical simulations.

It was found that the normal velocity on the surface of the secondary sources had to be varied rapidly in order to have very good noise cancellation on every field point specified. However, it was almost impossible to obtain that specific normal velocity on the surface of the sources in the real world. Consequently, modifications were made to accommodate the noise cancellation technique to practical situations. The

normal velocity on the surface of each secondary source was forced to be uniform. The dimension of the system of linear equations was significantly reduced. However, the noise reduction was not as good as the situation without the constraint.

# 4. NUMERICAL DETERMINATION OF SECONDARY SOURCES

Results of a set of numerical simulations are presented in this chapter to show the characteristics of the secondary sources. The coupled equation method together with SVD as described in the previous chapter is used. The number and sizes of the secondary sources are kept unchanged; while the locations of secondary sources and region of noise cancellation are varied for each numerical simulation. The BEM calculated the best region of noise cancellation, maximum noise level reduction and excitation functions for each secondary source. A data bank is established by performing the numerical simulations for different locations of the secondary sources. The range of noise cancellation in the neighborhood of specified field points and the effect of the size of the secondary sources to the noise reduction over the cancellation regions are investigated.

## 4.1 Optimal Noise Cancellation for the Locations of Secondary Sources

The purpose of this research is not only to introduce an inexpensive technique for active noise cancellation but also to provide a practical and convenient means to achieve noise reduction in the desired region. Therefore, it is hoped that the locations and excitation functions for secondary sources could be obtained once the region of noise cancellation is specified. The calculation of location and excitation functions

for each secondary source is possible in principle. One can formulate this problem as an optimization problem where a certain function is minimized. Such a formulation will lead to a non-linear problem and will require an iterative method for solution. However, several questions naturally arise. For example, is the convergence guaranteed? Is it guaranteed that the iteration will converge to the global minimization instead of converging to one of many possible local minima? Does an unique solution exist? Such questions can only be answered through detailed mathematical analysis in the published literature, and such analysis will not be attempted here. Instead, a series of numerical experiments were performed.

A baffled piston source of radius 1 m at $k = 1$ with uniform normal surface velocity was used as a primary source which radiated undesired acoustic noise into a half space. Because of the symmetry of the geometry and results from directivity tests, four secondary sources with the same dimensions were placed symmetrically around the primary source. The configuration of the numerical tests is shown in Figure 4.1. The primary source was discretized into 49 nodes and 16 surface elements, while each secondary source was discretized into 37 nodes and 12 surface elements. Therefore, there were 197 nodes and 64 surface elements for both primary and secondary sources. The distance d between the centers of primary and secondary sources, and the height of the noise cancellation plane $z = z_0$ were changed for each numerical simulation. The test cases are listed in Table 4.1. For each test case, two different arrangements of field points were considered as shown in Figure 4.2. In the first arrangement, 961 field points were specified over a $120m \times 120m$ plane to simulate the noise cancellation over an infinite region. In the second arrangement, 600 field points were specified over $120m \times 120m$ plane which excluded the central

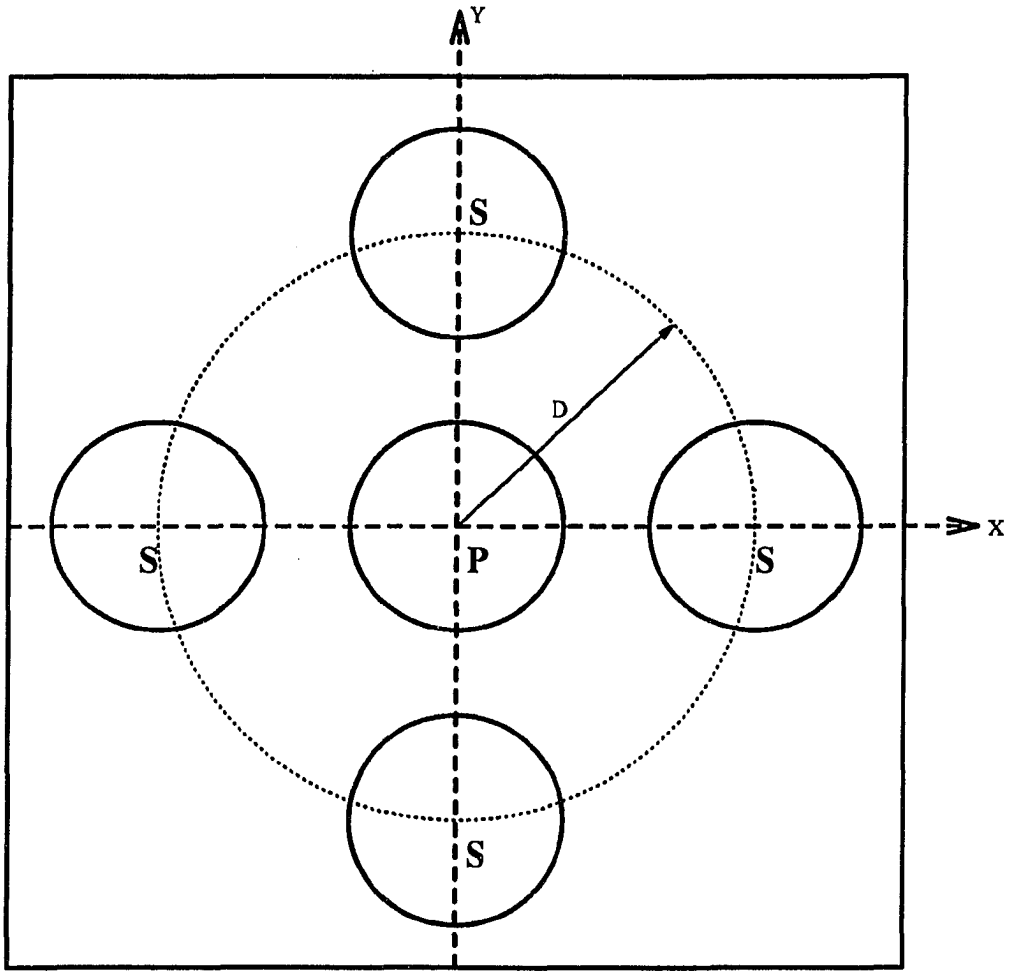


P : PRIMARY SOURCE

S : SECONDARY SOURCES

D : DISTANCE BETWEEN CENTER OF PRIMARY AND SECONDARY SOURCES

Figure 4.1: The configuration for noise cancellation technique

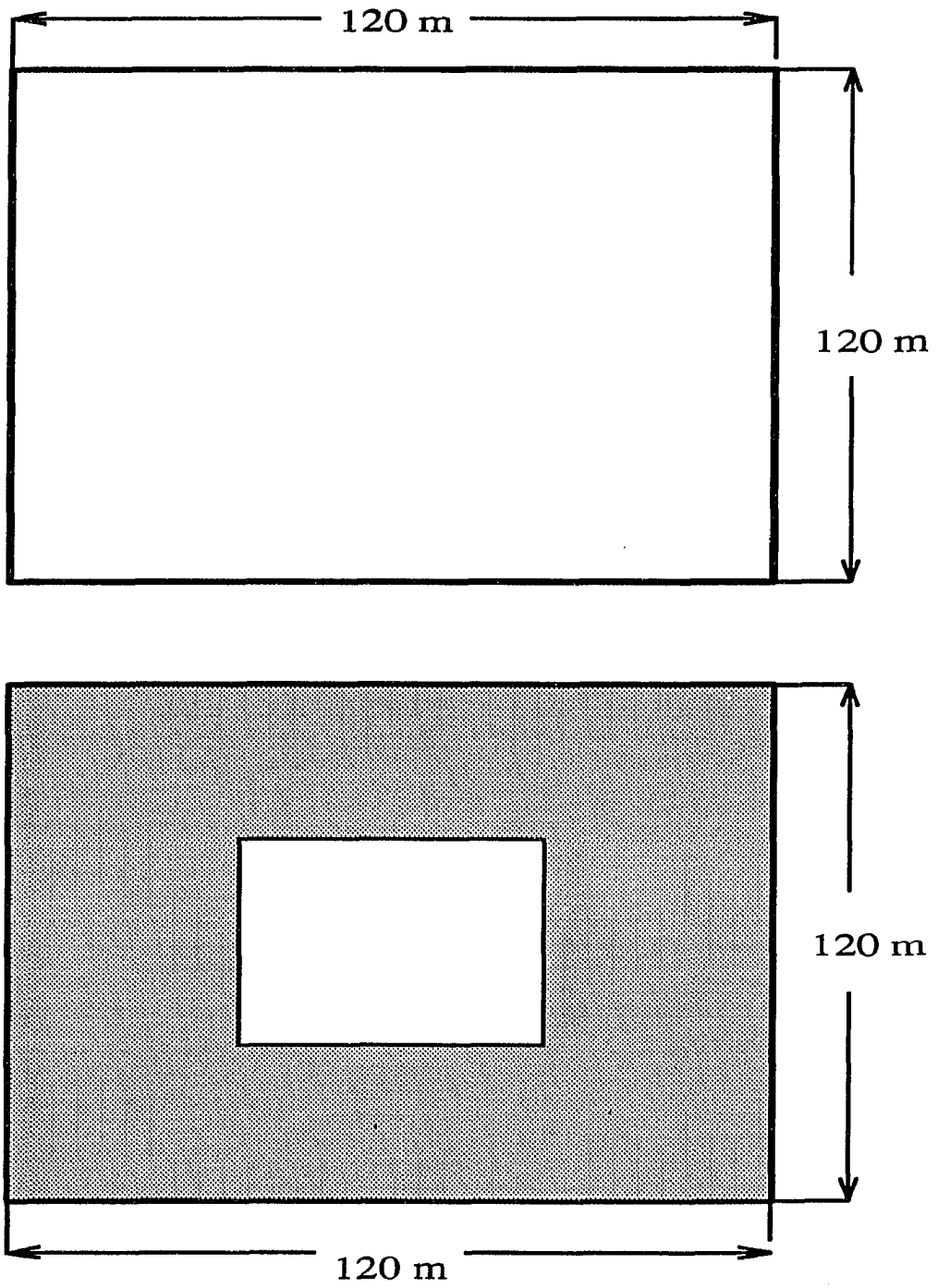


Figure 4.2: The cancellation planes

Table 4.1: Test conditions for numerical simulations

| d / $z_0$ | 2 | 3 | 4 | 5 | 6 | 7 | 8 | 9 | 10 | 15 | 20 | 25 | 30 |
|---|---|---|---|---|---|---|---|---|---|---|---|---|---|
| 1 | 1 | 2 | 3 | 4 | 5 | 6 | 7 | 8 | 9 | 10 | 11 | 12 | 13 |
| 5 | 14 | 15 | 16 | 17 | 18 | 19 | 20 | 21 | 22 | 23 | 24 | 25 | 26 |
| 10 | 27 | 28 | 29 | 30 | 31 | 32 | 33 | 34 | 35 | 36 | 37 | 38 | 39 |
| 15 | 40 | 41 | 42 | 43 | 44 | 45 | 46 | 47 | 48 | 49 | 50 | 51 | 52 |
| 20 | 53 | 54 | 55 | 56 | 57 | 58 | 59 | 60 | 61 | 62 | 63 | 64 | 65 |
| 25 | 66 | 67 | 68 | 69 | 70 | 71 | 72 | 73 | 74 | 75 | 76 | 77 | 78 |

The 78 test cases were done for two different arrangements of field points with the same configuration.
d: distance between centers of primary and secondary sources, in meters,
$z_0$: height of the noise cancellation plane, in meters.

$80m \times 80m$ square area to simulate the noise cancellation at far field points outside the sources. The test cases were done by the coupled equation method with SVD numerical implementation. In addition, uniform normal surface velocities for all the four secondary sources were assumed. The results were tabulated in Table 4.2 through 4.7. Typical noise reduction over the specified field points before and after secondary sources been added is shown in Figure 4.3. All the numerical simulations were performed for $ka = 1$, where k is the wave number, and a is the radius of the primary and secondary sources.

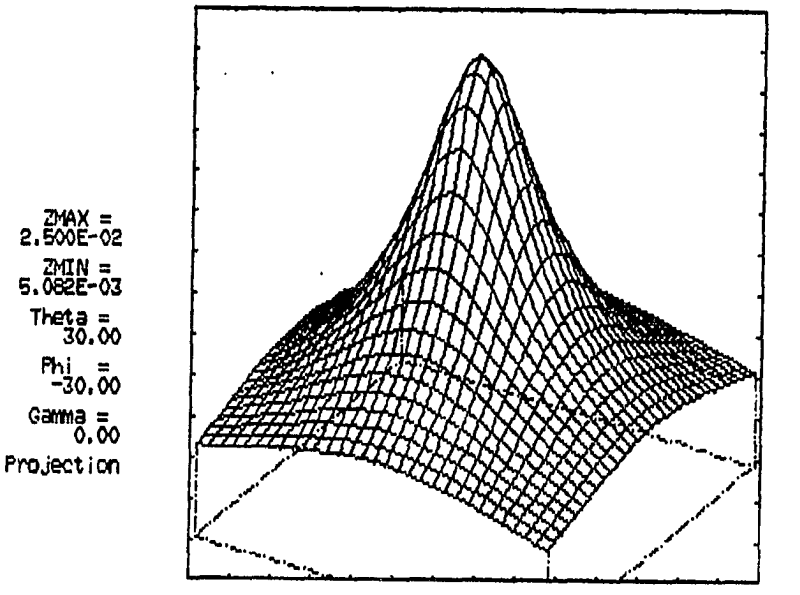


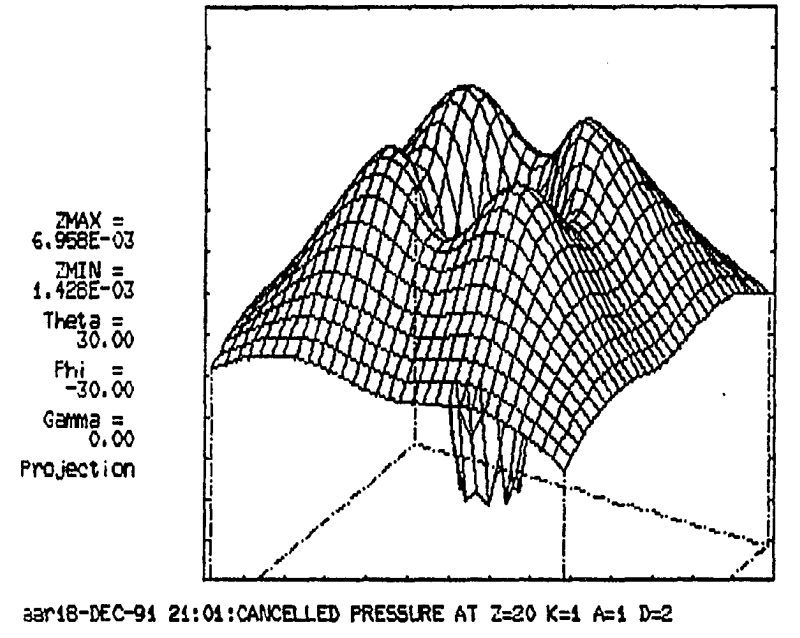


Figure 4.3: Acoustic pressure magnitude (in Pa) over 961 field points at $z_0 = 20m$ for $k = 1, a = 1m$; top: primary source only, bottom: canceled pressure with $d = 2m$

Table 4.2: Numerical simulation for $z_0 = 1m$

| d | $VEL.^1$ | $CAN.^1$ | $NR^1$ | $VEL.^2$ | $CAN.^2$ | $NR^2$ |
|---|---|---|---|---|---|---|
| 2 | (-0.318,2.968e-2) | 4.01 | 1.1748 | (-0.327,-1.731e-3) | 4.16 | 1.116e-2 |
| 3 | (-0.45,0.255) | 0.4 | 5.3236 | (-1.067,-4.748e-2) | N/A | 0.5072 |
| 4 | (0.414,0.169) | 7.81 | 5.9477 | (0.634, 1.562e-1) | 27.68 | 1.41 |
| 5 | (0.314,-9.210e-4) | 23.47 | 5.5865 | (0.314,6.901e-3) | 20.74 | 1.7117 |
| 6 | (0.195,-8.243e-2) | 8.58 | 7.1059 | (0.311,1.706e-2) | 3.06 | 2.3035 |
| 7 | (-6.361e-2,-0.142) | 3.64 | 7.7019 | (-0.132,1.823e-2) | 6.95 | 2.321 |
| 8 | (-0.351,-0.115) | 13.29 | 6.239 | (-0.434,-1.501e-3) | 12.49 | 1.6656 |
| 9 | (-0.281,4.444e-3) | 12.54 | 6.9307 | (-0.280,-4.207e-2) | 7.99 | 2.1642 |
| 10 | (-5.194e-2,7.962e-2) | 3.86 | 7.9324 | (6.411e-2,2.344e-2) | 4.11 | 2.3901 |
| 15 | (-9.663e-2,-7.136e-2) | 5.11 | 7.8805 | (-0.124,-9.168e-3) | 5.77 | 2.3151 |
| 20 | (-3.887e-2,1.671e-2) | 6.21 | 8.0615 | (-0.111,1.475e-2) | 4.46 | 2.3306 |
| 25 | (2.228e-2,-6.386e-3) | 2.08 | 8.081 | (6.564e-2,3.995e-2) | 9.55 | 2.3908 |
| 30 | (-1.162e-2,1.761e-2) | 2.16 | 3.7951 | (0.136,1.744e-3) | -6.15 | 2.3012 |

d : distance between centers of primary and secondary sources, in meters,
VEL. : normal surface velocity of secondary sources, in meter/second,
CAN. : maximum noise cancellation in dB,
NR : $l_2$ norm for all field points, in $Pascal^2$,
1 : 961 field points over 120 m * 120 m plane,
2 : 600 field points over 120 m * 120 m plane exclude central 80 m * 80 m area.

Table 4.3: Numerical simulation for $z_0 = 5m$

| d | $VEL.^1$ | $CAN.^1$ | $NR^1$ | $VEL.^2$ | $CAN.^2$ | $NR^2$ |
|---|---|---|---|---|---|---|
| 2 | (-0.307,5.548e-4) | 12.85 | 0.4331 | (-0.326,-1.68e-3) | 14.41 | 1.2098e-2 |
| 3 | (-0.536,6.140e-3) | 8.87 | 2.7764 | (-1.046,-4.529e-2) | 4.14 | 0.4975 |
| 4 | (0.207,8.580e-3) | 12.68 | 5.5353 | (0.641,-1.712e-2) | 30.29 | 1.4117 |
| 5 | (0.282,-2.157e-3) | 24.9 | 4.6484 | (0.317,6.156e-3) | 20.6 | 1.6933 |
| 6 | (0.179,-9.703e-3) | 5.63 | 5.2502 | (0.137,1.673e-2) | 3.53 | 2.285 |
| 7 | (1.995e-3,-1.629e-2) | 0.28 | 5.7561 | (-0.126,1.930e-2) | 5 | 2.3225 |
| 8 | (-0.195,-1.454e-2) | 7.85 | 5.32 | (-0.425,2.441e-3) | 13.79 | 1.6757 |
| 9 | (-0.239,8.758e-3) | 14 | 5.1844 | (-0.302,-3.945e-2) | 14.48 | 2.1191 |
| 10 | (-4.957e-2,2.866e-2) | 1.93 | 5.7148 | (5.698e-2,-2.51e-2) | 2.48 | 2.3884 |
| 15 | (-8.604e-2,-6.437e-2) | 4.06 | 5.5908 | (-0.131,-3.936e-3) | 6.1 | 2.295 |
| 20 | (4.765e-2,6.848e-2) | 3.16 | 5.6687 | (-9.933e-2,2.172e-2) | 5.87 | 2.3386 |
| 25 | (-5.355e-2,-1.112e-2) | 2.6 | 5.7246 | (9.104e-2,2.611e-2) | 6.83 | 2.3644 |
| 30 | (9.112e-2,-4.708e-2) | 6.33 | 5.6382 | (0.117,-2.898e-2) | 10.44 | 2.3156 |

Table 4.4: Numerical simulation for $z_0 = 10m$

| d | $VEL.^1$ | $CAN.^1$ | $NR^1$ | $VEL.^2$ | $CAN.^2$ | $NR^2$ |
|---|---|---|---|---|---|---|
| 2 | (-0.301,5.390e-4) | 18.58 | 0.3739 | (-0.324,-1.541e-3) | 20.03 | 1.5674e-2 |
| 3 | (-0.496,4.522e-3) | 14.99 | 2.2339 | (-0.988,-3.924e-2) | 20.06 | 0.4722 |
| 4 | (7.795e-2,5.624e-3) | 3 | 4.9668 | (0.661,-2.187e-2) | 30.31 | 1.419 |
| 5 | (0.270,-2.916e-3) | 26.31 | 4.1928 | (0.326,3.874e-3) | 20.83 | 1.6396 |
| 6 | (0.197,-6.754e-3) | 7.3 | 4.4846 | (0.156,1.542e-2) | 4.77 | 2.2265 |
| 7 | (4.558e-2,-7.06e-3) | 0.95 | 4.9696 | (-0.105,2.2023e-2) | 4.21 | 2.3258 |
| 8 | (-0.138,-4.742e-4) | 4.58 | 4.8131 | (-0.397,1.301e-2) | 13.72 | 1.7103 |
| 9 | (-0.219,1.182e-2) | 13.46 | 4.6056 | (-0.362,-2.85e-2) | 24.36 | 1.9743 |
| 10 | (-7.308e-2,1.263e-2) | 2.4 | 4.9383 | ((3.144e-2,-2.921e-2) | 1.48 | 2.379 |
| 15 | (-7.083e-2,-2.385e-3) | 2.38 | 4.9326 | (-0.143,1.27e-2) | 6 | 2.2417 |
| 20 | (1.754e-2,4.833e-3) | 0.64 | 4.9901 | (-5.871e-2,3.202e-2) | 2.71 | 2.359 |
| 25 | (2.087e-3,-1.227e-2) | 0.45 | 4.9924 | (0.116,-2.608e-2) | 5.13 | 2.2963 |
| 30 | (7.288e-2,-5.305e-2) | 4.5 | 4.9138 | (3.223e-2,-4.089e-2) | 2.54 | 2.3711 |

Table 4.5: Numerical simulation for $z_0 = 15m$

| d | $VEL.^1$ | $CAN.^1$ | $NR^1$ | $VEL.^2$ | $CAN.^2$ | $NR^2$ |
|---|---|---|---|---|---|---|
| 2 | (-0.297,6.271e-4) | 20.7 | 0.3325 | (-0.320,-1.329e-3) | 22.8 | 2.1726e-2 |
| 3 | (-0.466,4.72e-3) | 17.62 | 1.8886 | (-0.906,-3.135e-2) | 22.36 | 0.4416 |
| 4 | (-3.297e-2,7.040e-3) | 1.13 | 4.4895 | (0.694,-3.009e-2) | 26.09 | 1.4419 |
| 5 | (0.253,-3.449e-3) | 23.92 | 3.9021 | (0.339,2.551e-2) | 21.92 | 1.5611 |
| 6 | (0.282,-8.210e-3) | 9.12 | 3.9859 | (0.183,1.261e-2) | 6.71 | 2.1282 |
| 7 | (8.211e-2,-8.975e-3) | 2.25 | 4.4232 | (-7.066e-2,2.472e-2) | 2.96 | 2.3221 |
| 8 | (-9.05e-2,-1.604e-3) | 2.6 | 4.4225 | (-0.357,2.602e-2) | 14.69 | 1.771 |
| 9 | (-0.199,1.275e-2) | 11.77 | 4.1941 | (-0.425,-5.631e-3) | 11.5 | 1.7512 |
| 10 | (-0.109,1.654e-2) | 4.06 | 4.39 | (-2.217e-2,-3.115e-2) | 1.0 | 2.3451 |
| 15 | (-5.369e-2,-4.497e-4) | 1.8 | 4.4655 | (-0.146,3.696e-2) | 6.7 | 2.1875 |
| 20 | (2.84e-2,-1.130e-2) | 0.89 | 4.485 | (1.357e-2,1.326e-2) | 0.69 | 2.3503 |
| 25 | (2.803e-2,-9.067e-3) | 1.01 | 4.4852 | (8.192e-2,-6.828e-2) | 3.81 | 2.2674 |
| 30 | (-8.152e-4,8.075e-3) | 0.22 | 4.4935 | (-9.605e-3,3.416e-2) | 0.98 | 2.3436 |

Table 4.6: Numerical simulation for $z_0 = 20m$

| d | $VEL.^1$ | $CAN.^1$ | $NR^1$ | $VEL.^2$ | $CAN.^2$ | $NR^2$ |
|---|---|---|---|---|---|---|
| 2 | (-0.293,7.006e-4) | 23.89 | 0.2956 | (-0.316,-1.078e-3) | 24.72 | 2.8686e-2 |
| 3 | (-0.443,4.861e-3) | 18.38 | 1.6138 | (-0.819,-2.344e-2) | 21.46 | 0.4129 |
| 4 | (-0.131,8.482e-3) | 5.31 | 4.0429 | (0.736,-4.244e-2) | 26.29 | 1.4941 |
| 5 | (0.232,-3.46) | 18.46 | 3.6881 | (0.356,-4.404e-3) | 21.9 | 1.4712 |
| 6 | (0.216,-9.521e-3) | 10.81 | 3.6188 | (0.214,8.008e-3) | 9.41 | 1.994 |
| 7 | (0.114,-1.115e-2) | 3.72 | 3.9848 | (-2.185e-2,2.535e-2) | 1.08 | 2.2969 |
| 8 | (-4.574e-2,-3.659e-3) | 1.24 | 4.0945 | (-0.309,3.773e-2) | 15.16 | 1.8509 |
| 9 | (-0.171,1.234e-2) | 9.13 | 3.9 | (-0.453,2.442e-2) | 13.44 | 1.5383 |
| 10 | (-0.137,2.058e-2) | 5.76 | 3.967 | (-0.115,-2.251e-2) | 3.53 | 2.2437 |
| 15 | (-2.699e-2,-5.472e-3) | 0.74 | 4.1053 | (-0.130,5.909e-2) | 5.05 | 2.1684 |
| 20 | (4.198e-2,-1.599e-2) | 1.32 | 4.095 | (8.065e-2,-5.013e-2) | 3.36 | 2.2503 |
| 25 | (1.318e-2,-1.276e-3) | 0.37 | 4.11 | (3.310e-2,-4.386e-2) | 1.95 | 2.2832 |
| 30 | (-1.565e-2,2.215e-2) | 0.98 | 4.1053 | (-1.079e-3,6.242e-2) | 2.15 | 2.2775 |

Table 4.7: Numerical simulation for $z_0 = 25m$

| d | $VEL.^1$ | $CAN.^1$ | $NR^1$ | $VEL.^2$ | $CAN.^2$ | $NR^2$ |
|---|---|---|---|---|---|---|
| 2 | (-0.289,7.618e-4) | 24.65 | 0.2621 | (-0.311,-8.146e-4) | 26.24 | 3.505 |
| 3 | (-0.424,4.951e-3) | 20.91 | 1.3856 | (-0.735,-1.661e-2) | 21.29 | 0.3873 |
| 4 | (-0.214,9.876e-3) | 11.69 | 3.6133 | (0.773,-6.001e-2) | 23.44 | 1.5899 |
| 5 | (0.204,-3.162e-3) | 13.81 | 3.5145 | (0.375,-9.758e-3) | 23.84 | 1.3834 |
| 6 | (0.220,-1.062e-2) | 12.2 | 3.3358 | (0.245,1.946e-3) | 12.71 | 1.8355 |
| 7 | (0.143,-1.345e-2) | 5.21 | 3.6143 | (3.907e-2,2.223e-2) | 0.78 | 2.2231 |
| 8 | (-2.725e-3,-6.529e-3) | 0.11 | 3.7981 | (-0.255,4.576e-2) | 13.7 | 1.937 |
| 9 | (-0.138,1.063e-2) | 6.46 | 3.6657 | (-0.438,5.099e-2) | 16.6 | 1.4345 |
| 10 | (-0.153,2.376e-2) | 7.14 | 2.6331 | (-0.235,4.455e-3) | 11.11 | 2.0285 |
| 15 | (5.249e-3,-1.396e-2) | 0.54 | 3.7968 | (-8.21e-2,6.288e-2) | 3.97 | 2.1886 |
| 20 | (4.142e-2,-1.541e-2) | 1.27 | 3.7839 | (9.420e-2,-0.105) | 5.86 | 2.1351 |
| 25 | (-6.53e-3,1.259e-2) | 0.44 | 3.797 | (1.377e-2,3.621e-2) | 1.2 | 2.2355 |
| 30 | (-1.162e-2,1.761e-2) | 0.63 | 3.7951 | (-2.802e-2,5.431e-2) | 1.97 | 2.2226 |

It is noted from the Tables shown above that the noise reduction level depends not only on the locations of secondary sources and plane of noise cancellation but also on the arrangement of field points on the plane of noise cancellation. It is also noted that there are always one or more suitable configurations of secondary sources which will yield the best noise cancellation for a certain noise cancellation plane above the source plane. For example, if the noise reduction on a plane 10 m above the source plane is required for the second arrangement of field points, one can anticipate as much as 30.31 dB (see third row, sixth column of Table 4.4) noise cancellation at certain points when the distance between the centers of primary and secondary sources is 4 m apart provided that the excitation function for secondary sources is (0.6612,-2.1867e-2) m/s. Such exciting value of 30 dB noise cancellation indicates that the present method has great potential for application in practical noise

control. It is possible to determine the location and strength of secondary sources when a region of noise reduction is specified. Since, we have avoided the solution of a non-linear problem that has both location and strength as unknowns, the data bank created for the 78 cases will be employed in such determination. The data, as presented in Table 4.2 through 4.7, do not show any apparent pattern, and it is difficult for a designer to interpret these data. However, a pattern is hidden in these numbers, and we will now proceed to uncover that pattern.

A set of numerical experiments were performed for various combinations of $z_0$ and d. For each combination, the strengths of the secondary sources were computed by demanding noise cancellation in the least-square sense at 961 field points on the $z = z_0$ plane. The calculated values of the strengths of the secondary sources were then inserted in the boundary integral equation and the values of the acoustic pressure at the 961 field points are recalculated. The noise reduction level (NRL) at each of these points was then calculated from the equation

$$NRL = 20 \times log_{10} \left\{ \frac{p_2}{p_1} \right\} \tag{4.1}$$

where $p_2$ is the acoustic pressure after appropriate secondary sources are placed in the domain, and $p_1$ is the acoustic pressure due to the original primary source only. Points with positive NRL that indicated noise reinforcement instead of cancellation were discarded if they occurred. The remaining field points were guaranteed to have noise cancellation. The mean value $\mu$ and standard deviation $\sigma$ of the remaining NRL were calculated. Any point with NRL below the mean value were discarded again to ensure the regions of noise reduction were better than the average NRL. The remaining points were divided into four groups. The fourth group were those field points with $\mu \leq NRL < \mu + \sigma$ and are marked 4 on the following plots. The

third group were those field points with $\mu + \sigma \leq NRL < \mu + 2\sigma$ and are marked 3. The second group were for the field points with $\mu + 2\sigma \leq NRL < \mu + 3\sigma$ and are marked 2. The first group were for those field points with $\mu + 3\sigma \leq NRL$ and are marked 1. Since, the maximum NRL, mean $\mu$, and standard deviation $\sigma$ of the noise reduction level for each combination of $z_0$ and d are substantially different from one another, the first group in one test case was not necessarily better then the second group in another test. The typical noise reduction plots for $z_0 = 5m$ using the methodology above are shown in Figures 4.4 through 4.12. The plots for other $z_0$ values are very similar.

In these figures, the noise cancellation patterns are shown for the range $2m \leq d \leq 20m$. At $d = 2m$ (see Figure 4.4), the maximum noise cancellation region (region 1) are vertically above the primary source, and the cancellation region spreads from the center toward the edges of the square domain. At $d = 3m$ (see Figure 4.5), the cancellation regions get compressed and is located right above the primary source. At $d = 4m$ and 5m (see Figures 4.6 and 4.7), the cancellation regions 3 and 4 are aligned along the diagonals; with region 3 toward the corner, and region 4 toward the center. At $d = 6m$ (see Figure 4.8), the regions remain along the diagonals; with region 4 toward the corner. At $d = 7m$ (see Figure 4.9), the regions bifurcate into eight branches and get closer to the center of the domain. At $d = 8m$ (see Figure 4.10), the bifurcation disappears and four diagonal branches reappear. This pattern continues for $d = 9m$ and 10 m. At $d = 15m$ (see Figure 4.11), the cancellation region has a central ring, four short diagonal branches, and eight other long branches. At $d = 20m$ (see Figure 4.12), the pattern appears to have two central rings and twelve branches of almost equal lengths.

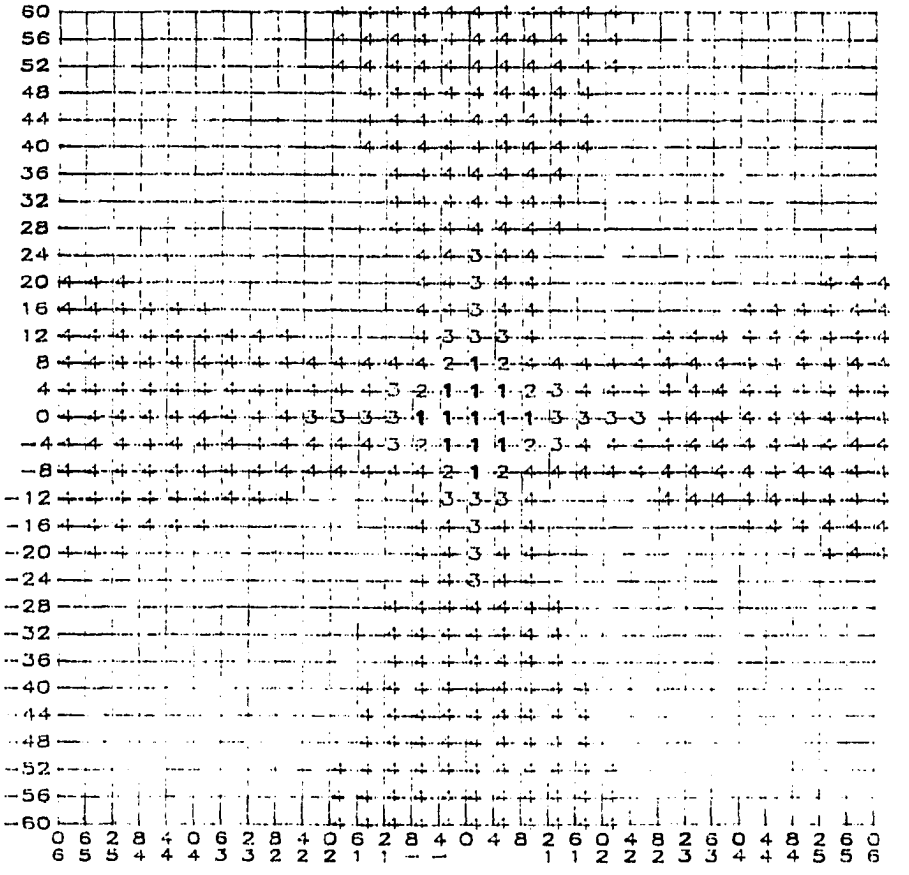


Figure 4.4: Noise reduction pattern for
$z_0 = 5m, k = 1, a = 1m, d = 2m, \mu = 2.94, \sigma = 1.11$

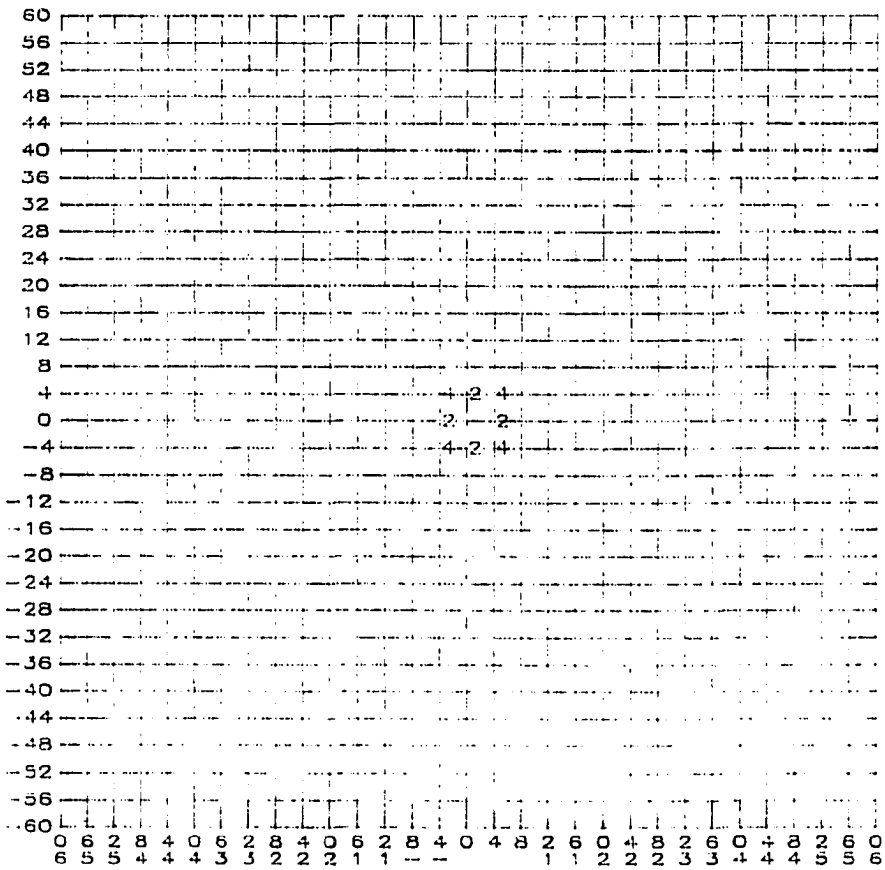


Figure 4.5: Noise reduction pattern for
$z_0 = 5m, k = 1, a = 1m, d = 3m, \mu = 1.28, \sigma = 3.72$

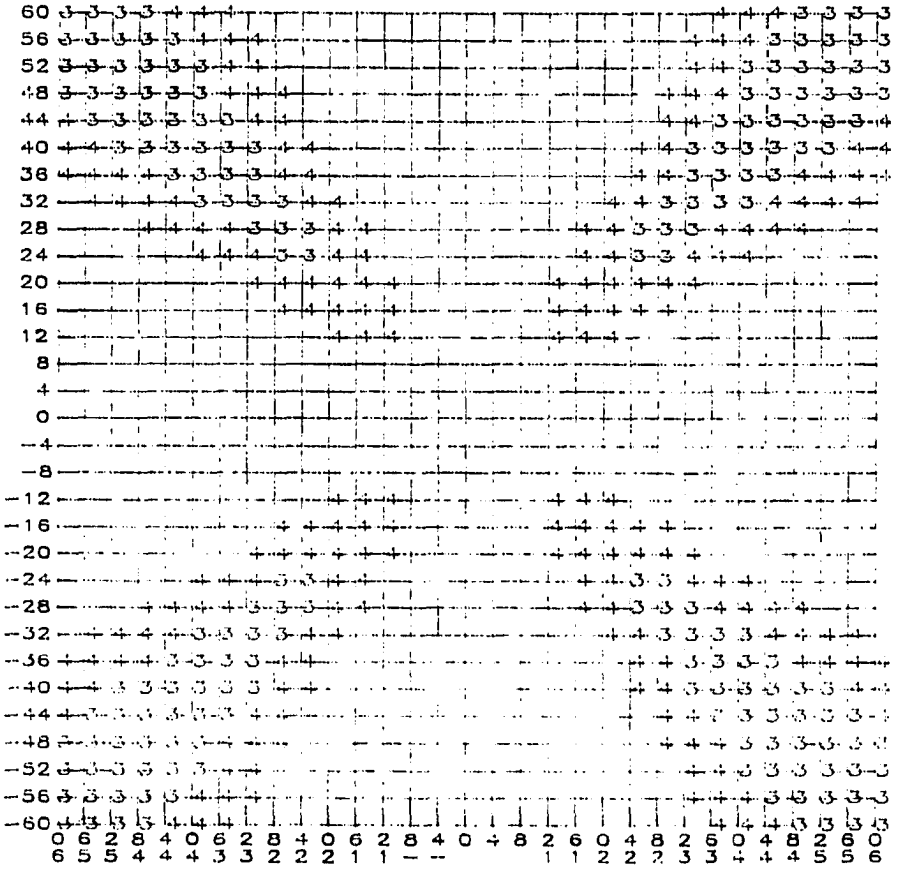


Figure 4.6: Noise reduction pattern for
$z_0 = 5m, k = 1, a = 1m, d = 4m, \mu = 6.58, \sigma = 4.06$

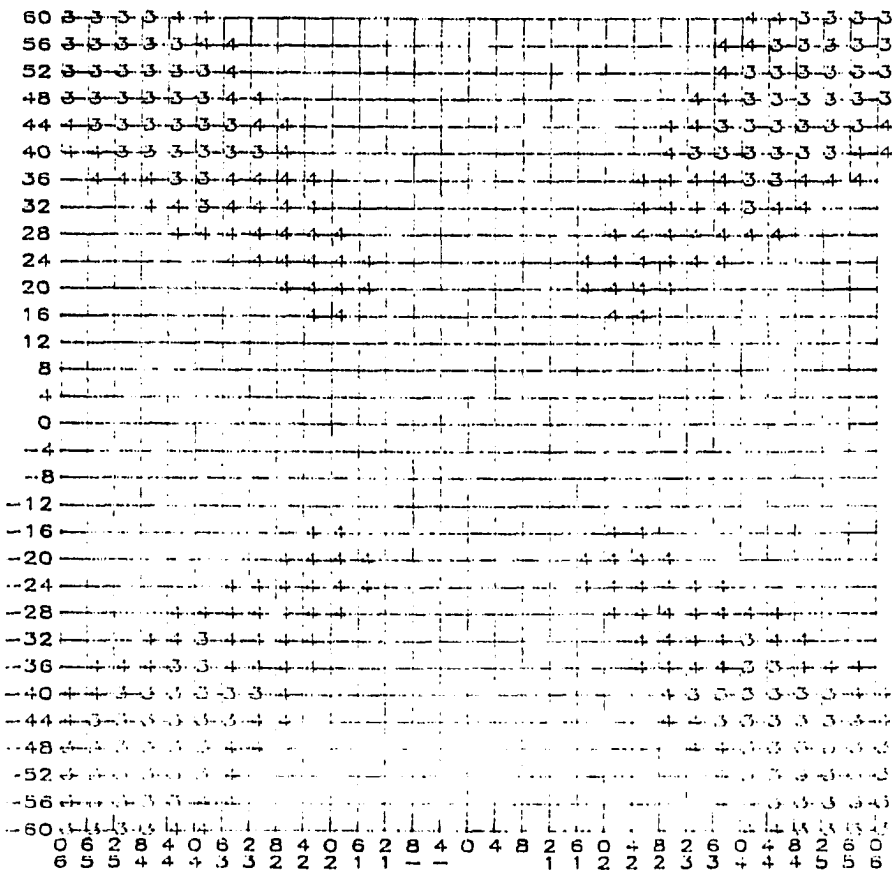


Figure 4.7: Noise reduction pattern for
$z_0 = 5m, k = 1, a = 1m, d = 5m, \mu = 12.36, \sigma = 7.73$

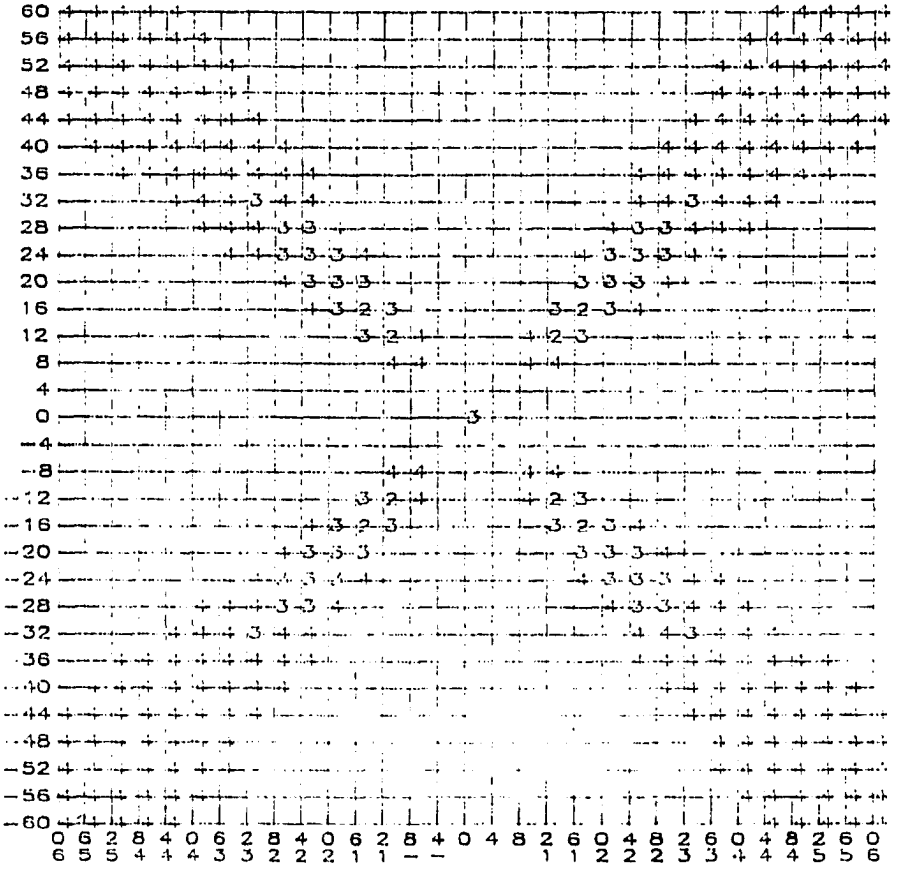


Figure 4.8: Noise reduction pattern for
$z_0 = 5m, k = 1, a = 1m, d = 6m, \mu = 2.63, \sigma = 1.4$

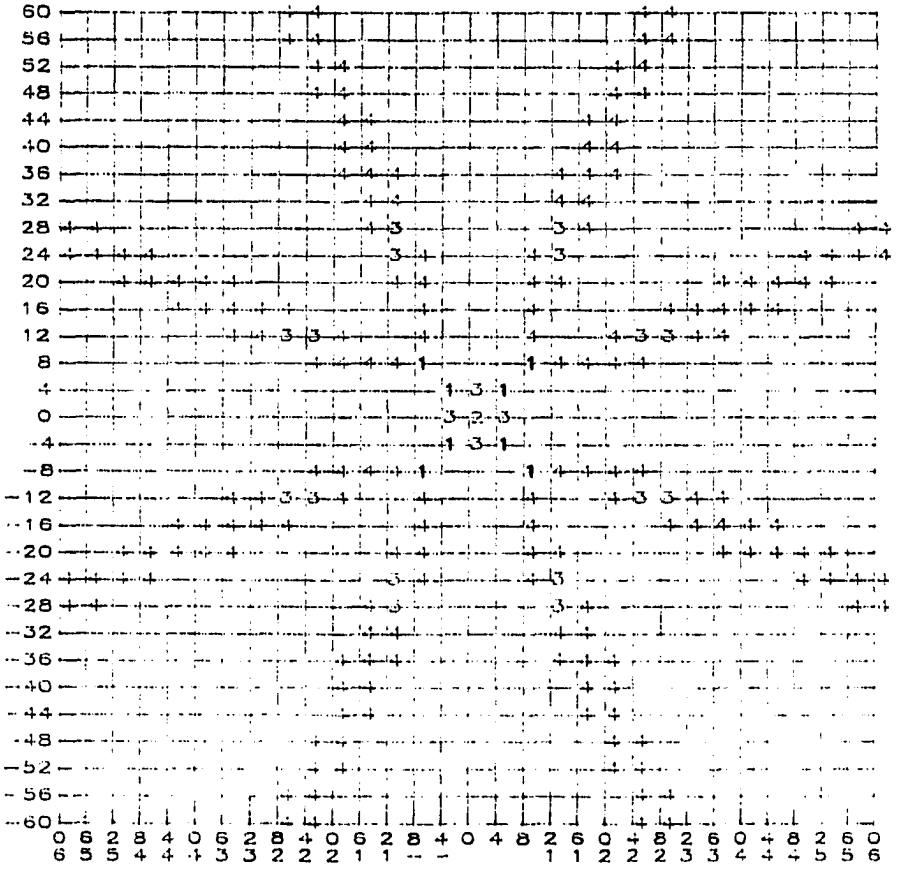


Figure 4.9: Noise reduction pattern for
$z_0 = 5m, k = 1, a = 1m, d = 7m, \mu = 0.06, \sigma = 0.04$

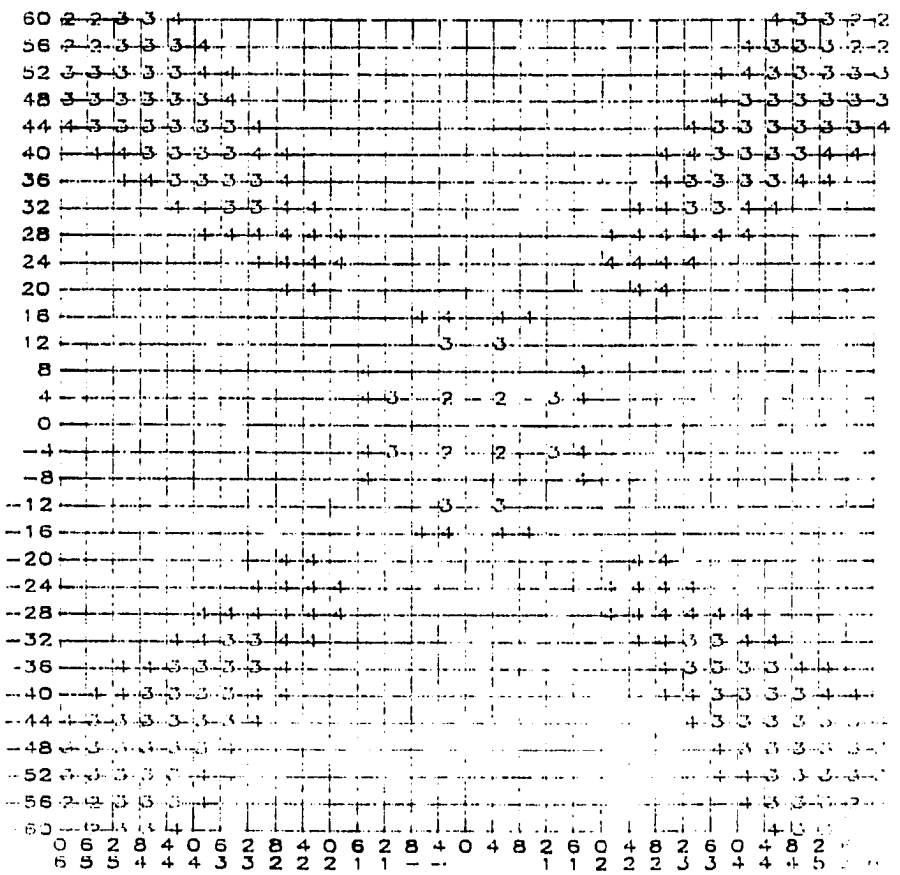

Figure 4.10: Noise reduction pattern for
$z_0 = 5m, k = 1, a = 1m, d = 8m, \mu = 2.66, \sigma = 1.97$

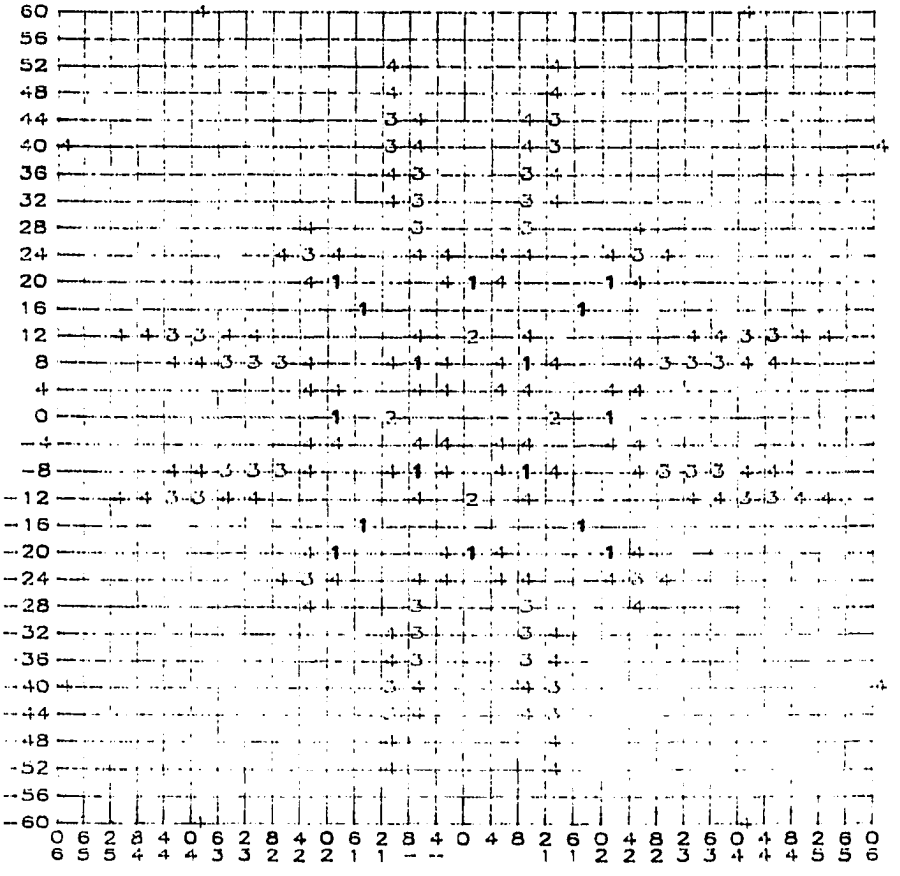


Figure 4.11: Noise reduction pattern for
$z_0 = 5m, k = 1, a = 1m, d = 15m, \mu = 0.92, \sigma = 0.77$

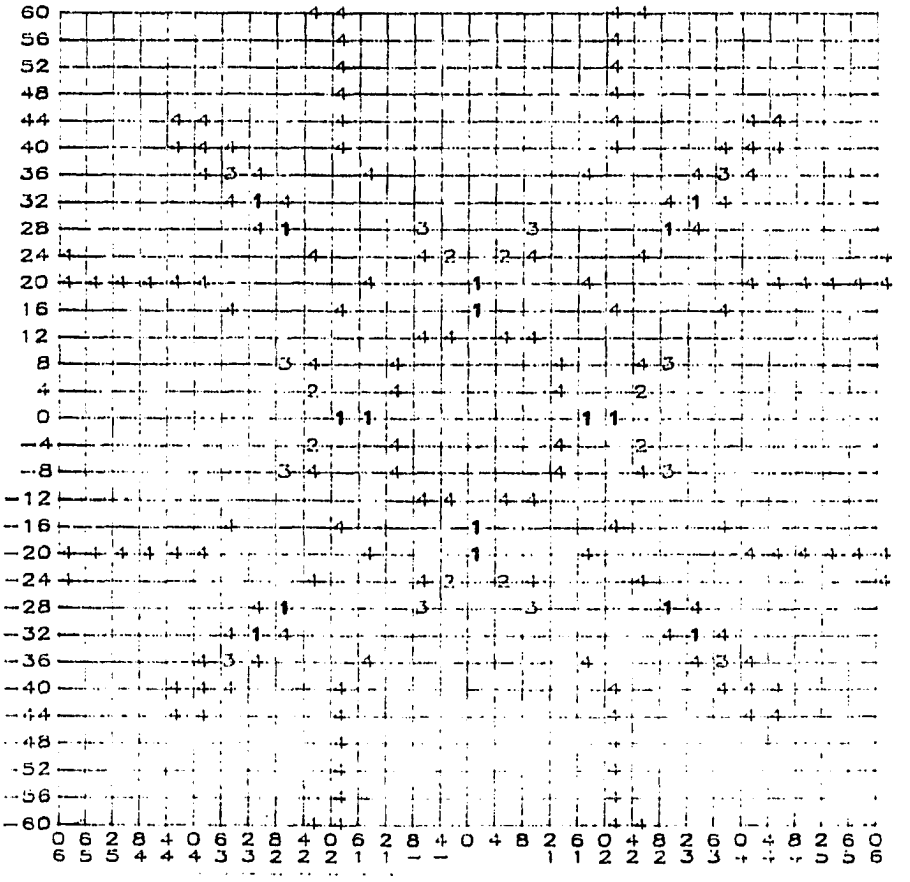


Figure 4.12: Noise reduction pattern for
$z_0 = 5m, k = 1, a = 1m, d = 20m, \mu = 0.69, \sigma = 0.59$

The magnitude of noise reduction for the region 1, 2, 3, and 4 for different values of d are shown in Table 4.8. These tabulated data show that cases corresponding

Table 4.8: Ranges of noise cancellation for various d at $z_0 = 5m$

| d (m) | Noise cancellation range in dB | | | |
|---|---|---|---|---|
| | Region 1 | Region 2 | Region 3 | Region 4 |
| 2 | 6.27 to 12.85 | 5.16 to 6.27 | 4.05 to 5.16 | 2.94 to 4.05 |
| 3 | - | 8.88 | - | 1.82 to 5 |
| 4 | - | - | 10.64 to 12.68 | 6.58 to 10.64 |
| 5 | - | - | 20.09 to 24.9 | 12.36 to 20.09 |
| 6 | - | 5.23 to 5.63 | 4.03 to 5.23 | 2.63 to 4.03 |
| 7 | 0.18 to 0.28 | 0.14 to 0.18 | 0.1 to 0.14 | 0.06 to 0.1 |
| 8 | - | 6.6 to 7.85 | 4.63 to 6.6 | 2.66 to 4.63 |
| 9 | - | - | 10.21 to 14 | 6.24 to 10.21 |
| 10 | - | - | 1.54 to 1.93 | 0.99 to 1.54 |
| 15 | 3.23 to 4.06 | 2.46 to 3.23 | 1.69 to 2.46 | 0.92 to 1.69 |
| 20 | 2.46 to 3.16 | 1.87 to 2.46 | 1.28 to 1.87 | 0.69 to 1.28 |
| 25 | 2.14 to 2.6 | 1.61 to 2.14 | 1.08 to 1.61 | 0.55 to 1.08 |
| 30 | 4.94 to 6.33 | 3.74 to 4.94 | 2.54 to 3.74 | 1.34 to 2.54 |

to $d$ = 2, 4, and 5 m which are the most efficient cases. When noise reduction right above the primary source is required, one can place the secondary sources at $d = 2m$ and expect a 6.27 dB to 12.85 dB reduction over a square domain of size $12m \times 12m$. When noise reduction away from the center is required, one can place the secondary sources at $d = 4m$ or 5 m. However, the two perpendicular lines on which the secondary sources are placed should be rotated by an appropriate amount so that one of the four diagonal branches coincide with the required area of noise reduction. For such an arrangement, one can expect a 10.64 dB to 24.9 dB noise reduction.

The noise reduction pattern of all the generated data for $z_0$ = 1, 10, 15, 20, and 25 m are very similar to those shown in Figures 4.4 through 4.12 for $z_0 = 5m$. Hence,

the guidelines for the placement of secondary sources, given above, remain the same for a wide range of $z_0$.

## 4.2 Slab of Cancellation

It has been observed in the numerical experiments that the noise reduction technique provides a noise reduction not just at the specified field points but in a finite neighborhood of the field points. Hence, when the cancellation conditions are enforced on a plane of zero thickness, one in effect gets a noise reduction in a slab of finite thickness. In order to gauge the thickness of the slab, the noise reduction condition was enforced at the plane $z_0 = 10m$, and the strengths of the secondary sources were obtained. These strengths were then utilized to calculate NRL in dB scale along a finite vertical line between $z_0 = 1m$ to $z_0 = 100m$ and passing through the point $(x,y) = (40m, 16m)$. The variation of the NRL is shown in Figure 4.13. This plot shows that within a thickness of $z_0 = 1m$ to $z_0 = 30m$, the NRL is more than 20 dB.

## 4.3 Effect of the Size of Secondary Sources

The size of secondary sources were pre-selected in the numerical simulations performed in the previous sections. However, the size of secondary sources is expected to affect the noise reduction level on the cancellation plane. The radii of secondary sources were changed from 1 m to 3 m with 0.5 m increment while the radius of primary source was kept to be 1 m to investigate the effect of the size of secondary sources on the noise reduction level over the cancellation plane. The configuration shown in Figure 4.1 was used except the radii of secondary sources were varied. The

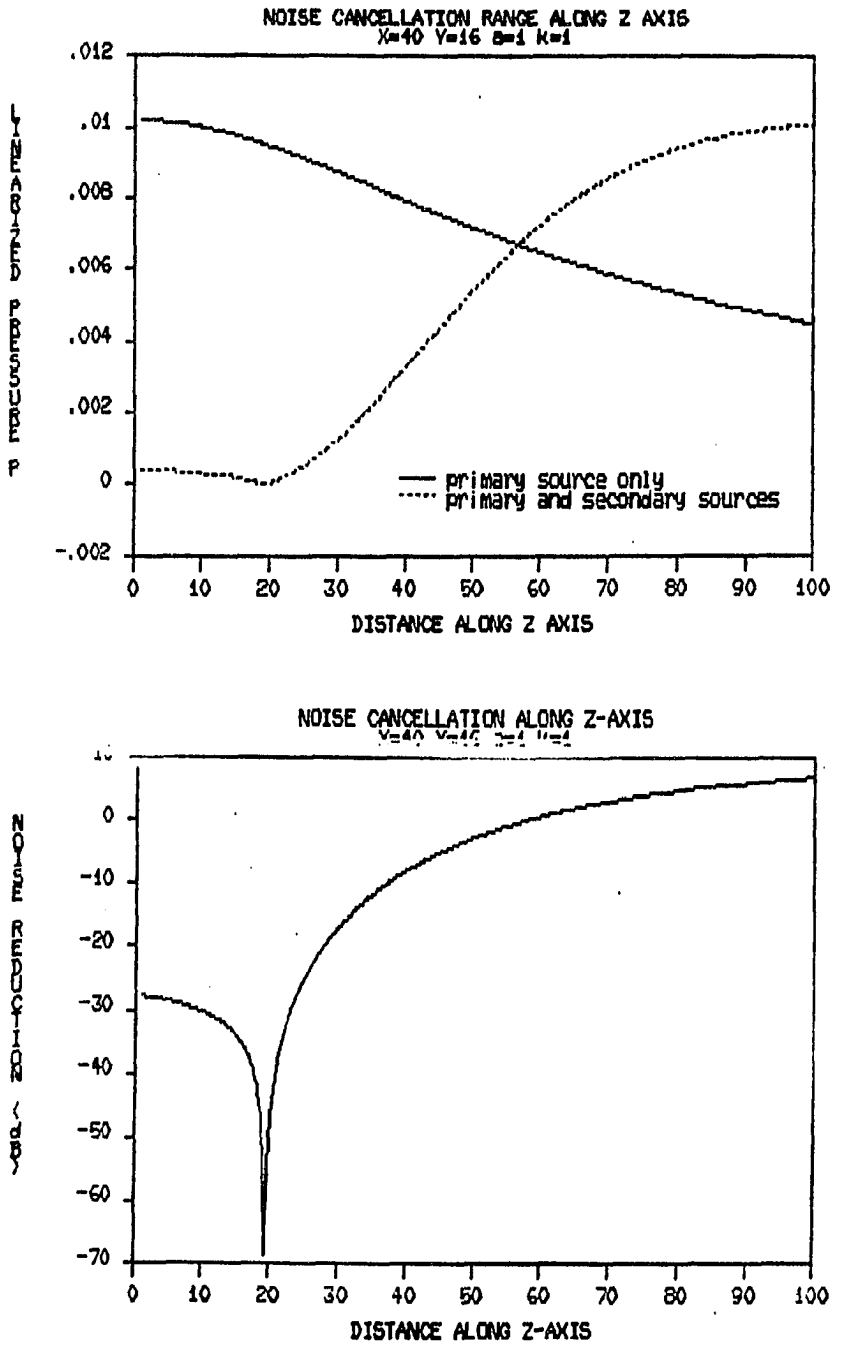


Figure 4.13: Noise reduction at the neighborhood of field point with $k = 1, a = 1m, d = 4m, x = 40m, y = 16m$; Excitation function based on $z_0 = 10m$; top: acoustic pressure magnitude in Pa, bottom: noise reduction level.

961 field points over $120m \times 120m$ plane were specified on $z_0 = 10m$. The solutions are shown in Table 4.9.

Table 4.9: Numerical simulation of $z_0 = 10m, d = 4m$ and $a_1 = 1m$ with different secondary sources radius

| $a_2$ | VEL. [m/s] | MAX. CAN. | NR |
|---|---|---|---|
| 1.0 | (7.7946e-2,5.6239e-3) | 3 | 4.9668 |
| 1.5 | (0.1306,-1.6379e-3) | 22.64 | 4.2611 |
| 2.0 | (8.1255e-2,-1.2572e-3) | 14.27 | 4.3761 |
| 2.5 | (5.5582e-2,-1.1565e-3) | 8.04 | 4.5557 |
| 3.0 | (3.4072e-2,-1.1416e-3) | 3.69 | 4.7949 |

$a_2$ : radii of secondary sources, in meters,
VEL. : normal surface velocity on secondary sources, in meter/second,
MAX. CAN. : maximum noise reduction level in dB,
NR : $l_2$ norm of the acoustic pressure over the field points.

The noise reduction patterns are shown in Figures 4.14 through 4.17. It was found that the noise reduction pattern for all configurations was similar. However, the maximum noise reduction levels were significantly increased from 3 dB to 22.64 dB when the radii of secondary sources increased from 1 m to 1.5 m. However, further increments of the size of secondary sources did not increase the noise reduction level. On the contrary, the maximum noise reduction level was decreased to 3.69 dB when the radii of secondary sources were 3m. It is realized that larger controllable surface area from secondary sources tends to produce better noise reduction level over the same cancellation plane than small surface area does. However, the secondary sources tended to cancel themselves instead of the primary source when the surface area from secondary sources was too large. In fact, the secondary sources tried to cancel the noise produced by themselves rather than the noise from the primary source.

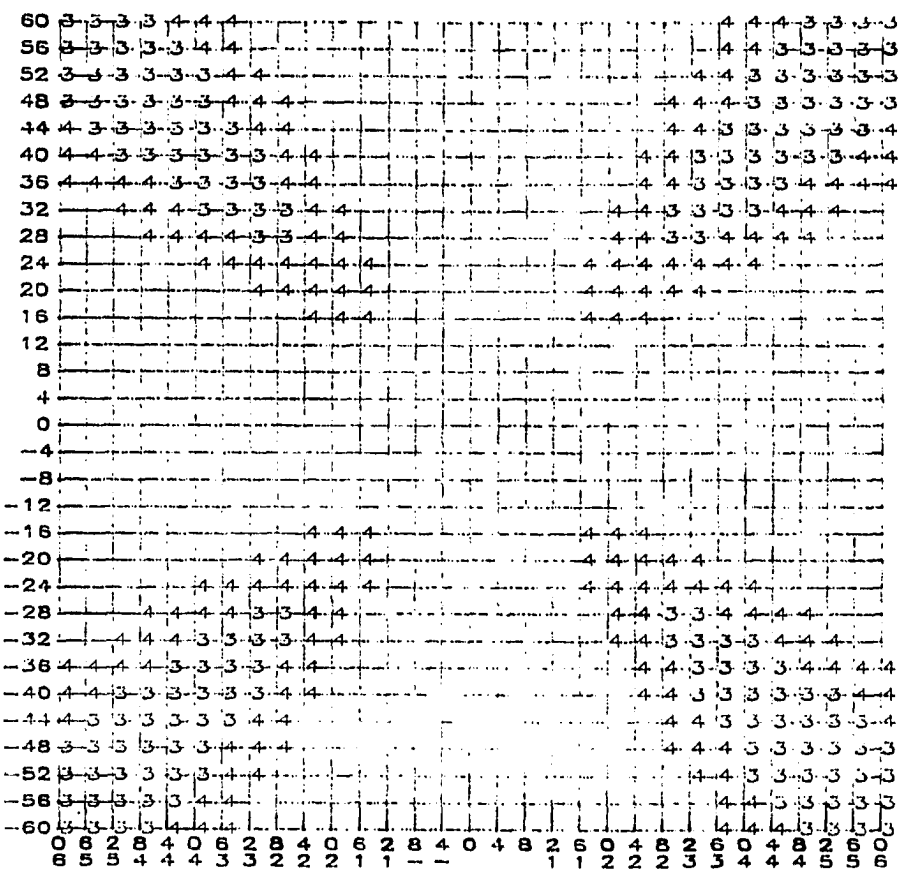

Figure 4.14: Noise reduction pattern for
$z_0 = 10m, k = 1, a_1 = 1m, a_2 = 1.5m, d = 4m, \mu = 9.59, \sigma = 6.85$

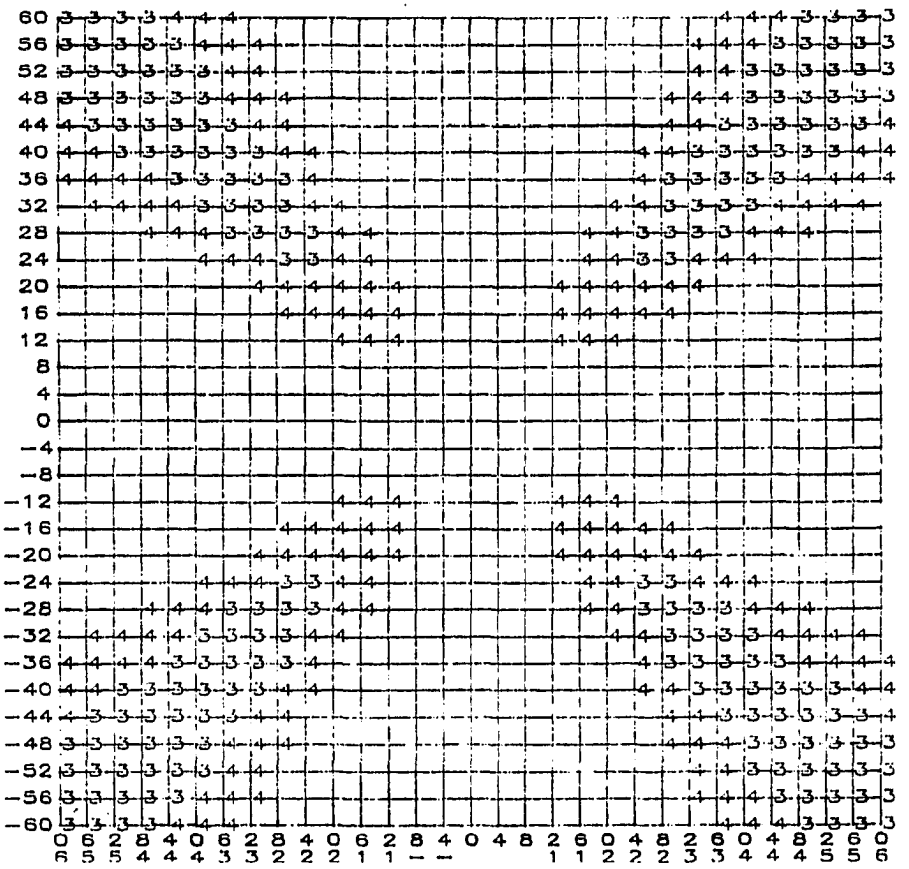


Figure 4.15: Noise reduction pattern for
$z_0 = 10m, k = 1, a_1 = 1m, a_2 = 2m, d = 4m, \mu = 7.08, \sigma = 4.65$

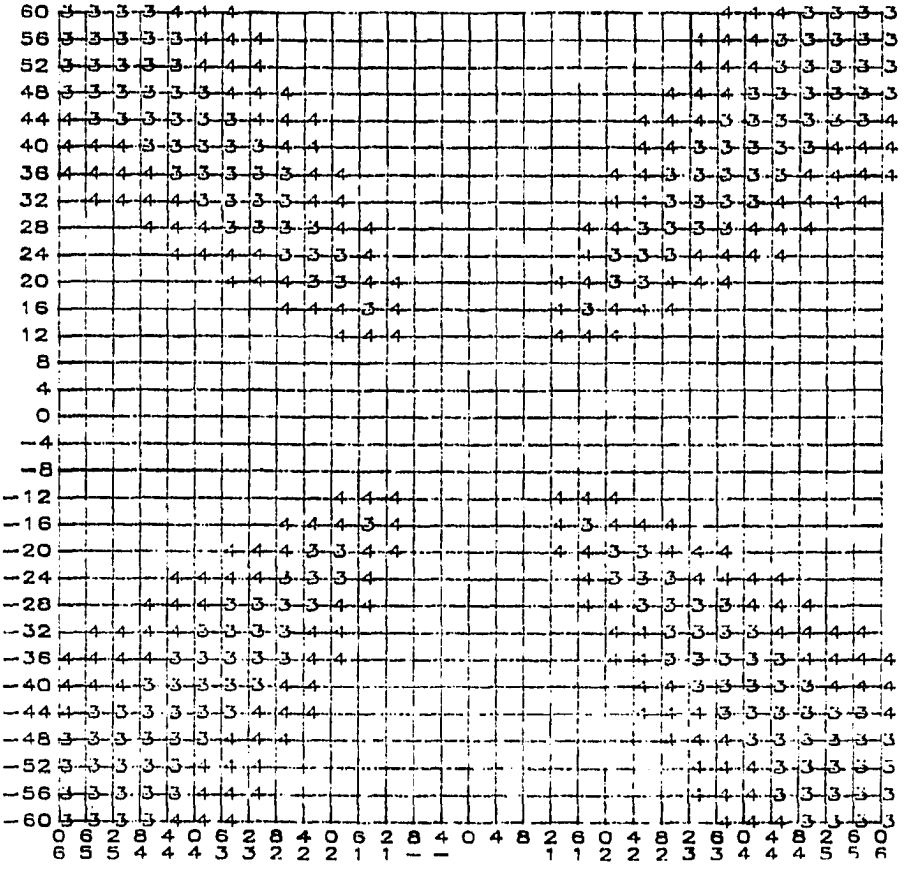


Figure 4.16: Noise reduction pattern for
$z_0 = 10m, k = 1, a_1 = 1m, a_2 = 2.5m. d = 4m, \mu = 4.49, \sigma = 2.69$

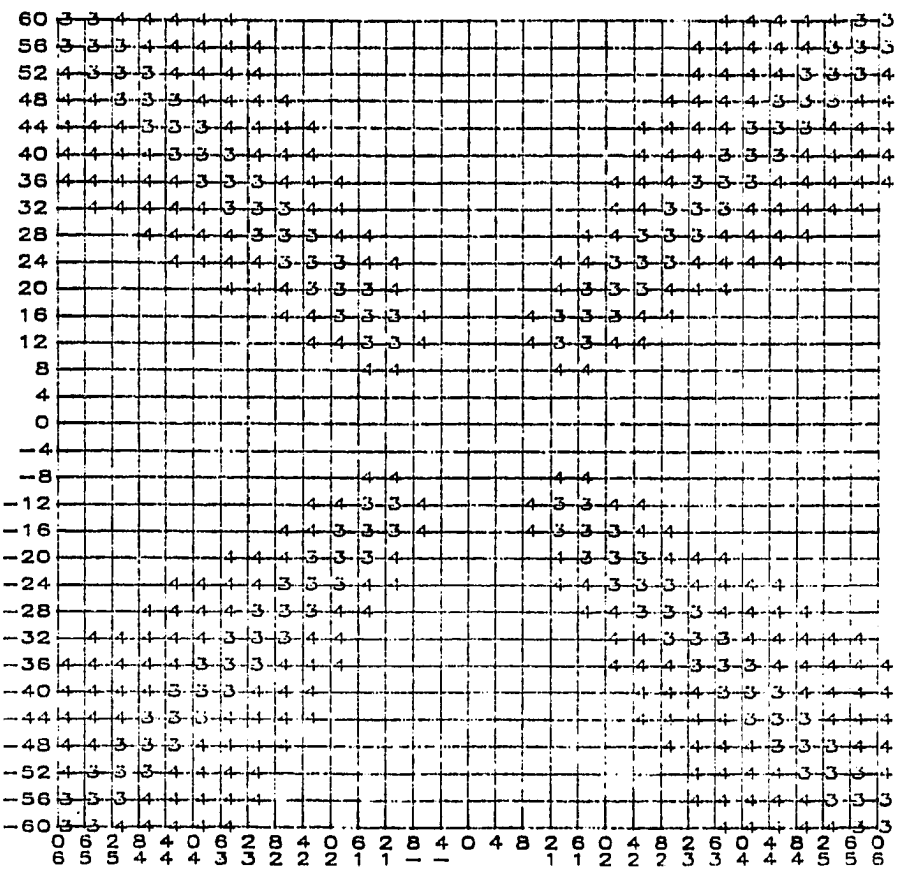

Figure 4.17: Noise reduction pattern for
$z_0 = 10m, k = 1, a_1 = 1m, a_2 = 3m, d = 4m, \mu = 2.01, \sigma = 1.1$

Consequently, the noise reduction level was lowered when the size of secondary sources increased. From the numerical simulations shown above, it would be better to have the radii of secondary sources 1.5 times that of the primary source in order to achieve better noise reduction level.

## 4.4 Discussion

The validity of the noise cancellation technique was justified numerically by BEM with coupled equation method in this chapter. The characteristics of secondary sources were also identified by BEM. A set of 156 numerical simulations were performed in order to get the relationship between the locations of secondary sources and the regions of best cancellation for constant size of secondary sources. It was suggested that the noise reduction pattern for the configuration which has the best noise cancellation be stored. The noise cancellation technique is then applied to obtain noise reduction over desired regions by rotating the locations of secondary sources such that the noise reduction pattern coincides with the regions in which noise reduction are required.

It should be noted that the noise cancellation technique minimizes the root mean square of the acoustic pressure over all specified field points. Therefore, closely specified field points are not desirable. In addition, closely specified field points will cause the secondary sources to cancel the noise from each other instead of canceling the noise from primary source. Consequently, the noise reduction level will be poor. In addition, it was shown that the cancellation region is quite wide and thick.

It is important to notice that the size of secondary sources has significant effect on the noise reduction. However, it was shown that the radii of secondary sources should

be 1.5 times the radius of primary sources for the numerical simulations investigated in this research.

# 5. EXPERIMENTAL VERIFICATION OF DERIVED NOISE CANCELLATION

The validity of the noise cancellation technique is verified experimentally in this chapter. A 6" speaker which radiated undesired acoustic noise into a half space was mounted in a rigid baffle. The speaker was used as the primary noise source to simulate a noise source with uniform surface velocity. The speaker was driven at 100, 1000, and 2000 Hz frequencies and its radiation patterns were experimentally investigated for those three frequencies to confirm the similarity to baffled piston radiation. The noise was canceled by four 10" speakers located symmetrically around the 6" speaker. The cancellation plane was 20 cm above the baffle plane with dimensions $120cm \times 120cm$ where 961 field points were specified over the plane. In addition, a baffled rectangular aluminum plate with a rib along its short side was used as a primary noise source with non-uniform surface velocity. The acoustic noise was canceled by four 10" speakers positioned at one side of the plate. The cancellation plane was 5 cm above the baffle plane with dimensions $120cm \times 60cm$ where 496 field points were specified over the plane. It should be noted that the configuration of the sources and the cancellation plane were chosen arbitrarily in order to investigate the validity of the noise cancellation technique. It is not necessary that the configuration used in this chapter gives the best noise cancellation for the specified cancellation plane.

The surface velocity normal to the primary source was evaluated in order to calculate the acoustic pressure over the cancellation plane. The noise cancellation technique was applied to cancel the acoustic noise generated by the primary noise source. In order to accomplish this goal, the excitation functions for the secondary sources were identified numerically by the noise cancellation technique using the boundary element method. The excitation functions for the secondary sources were generated by a computer and supplied to the secondary speakers through a multi-channel digital/analog converter. The acoustic pressure before and after adding the secondary sources were measured by a $\frac{1}{4}$-inch microphone and an FFT analyzer. The acquired data were transferred via a IEEE 488 interface bus to a computer to evaluate the noise reduction on every specified field point. The best regions for noise cancellation and the maximum noise reduction for the specific configuration were thus evaluated according to the experimentally measured data. The results of noise reduction for both types of primary sources were displayed and discussed.

## 5.1 Experimental Procedures

The noise cancellation technique was applied to a half space inside an anechoic chamber. The acoustic field inside the half space generated by the primary noise source should be identified before the noise cancellation technique can be applied. Therefore, the surface velocity normal to the primary noise source was evaluated in order to calculate the acoustic pressure over the cancellation plane inside the half space. The measurement setup for the experimental evaluation of the noise cancellation technique is shown in Figure 5.1. The acoustic pressure on the cancellation plane was measured by a quarter-inch microphone which was mounted on a 2-D

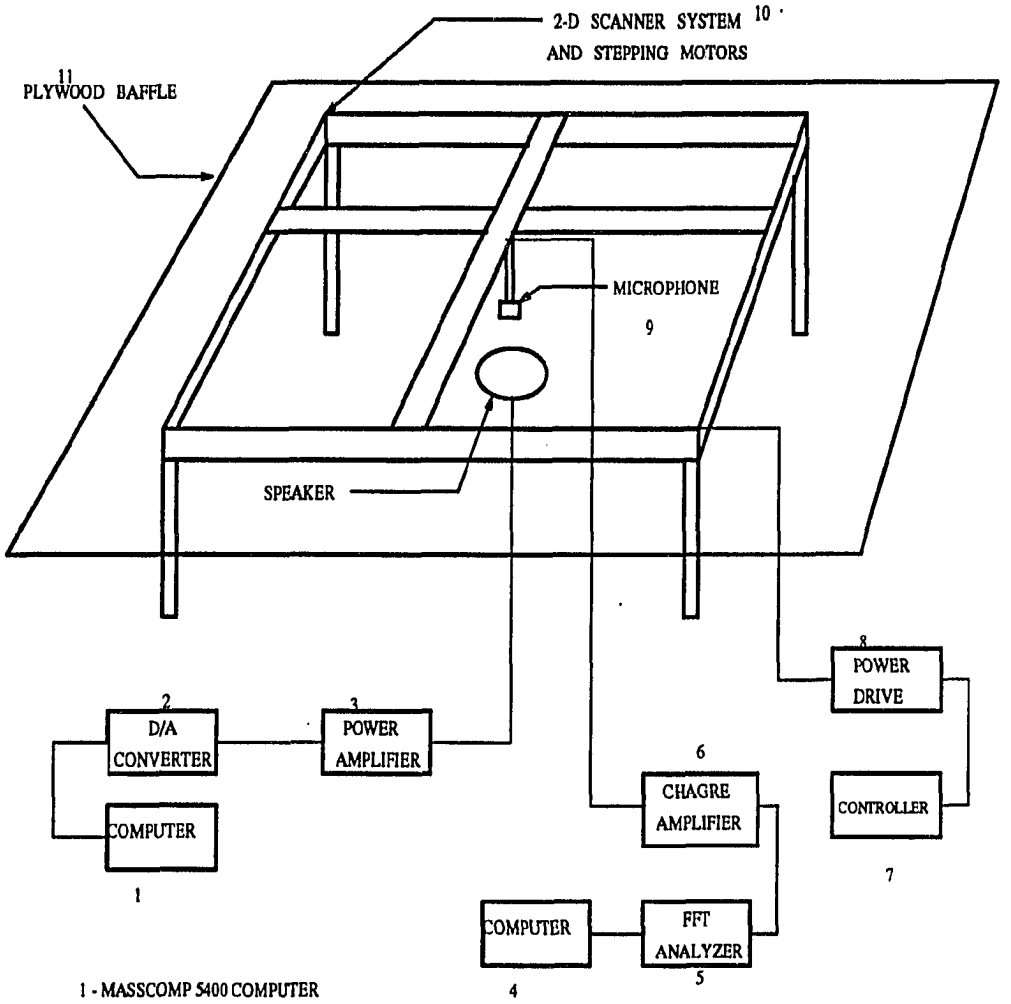


1 - MASSCOMP 5400 COMPUTER
2 - DIGITAL/ANALOG CONVERTER
3 - POWER AMPLIFIER BRUEL & KJAER 2706
4 - MICRO-VAX I COMPUTER
5 - FFT FREQUENCY ANALYZER BRUEL & KJAER 2032
6 - CHARGE AMPLIFIER BRUEL & KJAER 2807
7 - DUAL CHANNEL CONTROLLER KLINGER CC1.2
8 - STEPPING MOTER POWER DRIVE KLINGER MD 4
9 - 1/4" MICROPHONE BRUEL & KJAER 3519
10 - 2-D SCANNER SYSTEM AND STEPPING MOTORS SUPERIOR ELECTRIC M092-FD09
11 - PLYWOOD BAFFLE

Figure 5.1: The measurement setup for the experimental evaluation of the noise cancellation technique.

scanner. The microphone was moved to specified field points by a dual channel controller and stepping motors. The measured signal was analyzed by a Bruel and Kjaer FFT analyzer to evaluate the complex acoustic pressure. The acoustic pressure was then transferred to a VAX computer for post-processing. The block diagram for the experimental setup is shown in Figure 5.2. It should be noted that the FFT analyzer can not measure the complex acoustic pressure directly. Consequently, a reference signal is required. The output signal from the power amplifier was used as a reference signal. The autospectrum of this reference signal and the frequency response function between this reference signal and the desired acoustic pressure were measured using a Bruel and Kjaer 2032 FFT frequency analyzer. The complex acoustic pressure was then recovered from these two functions. All measured signals were referred to this reference signal in order to obtain both the magnitude and phase of the acoustic pressure at measuring locations. Consequently, the acoustic pressure over the cancellation plane from the primary noise source was identified.

The experimental procedure for the application of the noise cancellation technique is described as follows:

1. The locations of the primary source was determined. The cancellation plane was chosen where the field points were specified over the plane. The acoustic pressure at each field point was measured according to the measurement procedures described in a previous paragraph where the autospectrum of the reference signal and the frequency response function between reference signal and the desired signal were measured with 100 ensemble averages.

   Three different frequencies of 100 Hz, 1000 Hz, and 2000 Hz were used when the 6" speaker was used as the primary source. On the other hand, 150 Hz, which

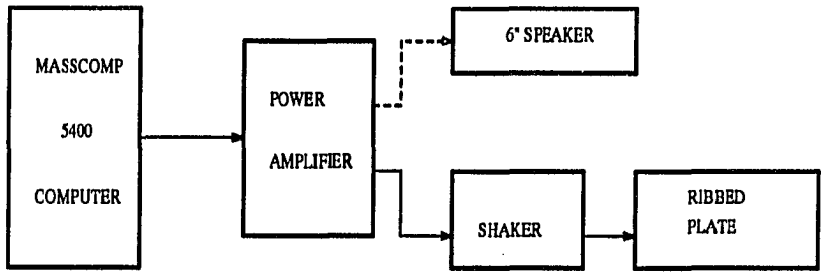


(a) The block diagram for primary noise source generation

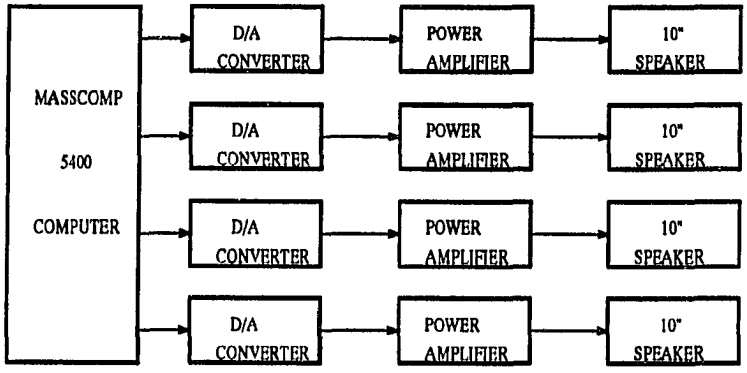


(b) The block diagram for secondary noise source generation


(c) The block diagram for 2-D scanner system used to position the microphone

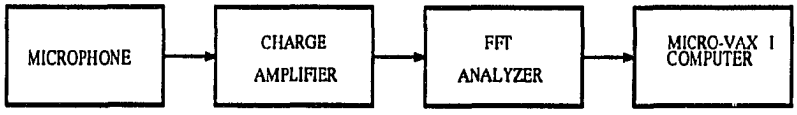


(d) The block diagram for data acquisition system

DUAL CHANNEL CONTROLLER : KLINGER CC1.2
POWER DRIVE : KLINGER MD 4
STEPPING MOTOR : SUPERIOR ELECTRIC M092-FD09
MICROPHONE : BRUEL & KJAER 3519
CHARGE AMPLIFIER : BRUEL & KJAER 2807
POWER AMPLIFIER : BRUEL & KJAER 2706
SHAKER : BRUEL & KJAER 4809

Figure 5.2: The block diagram for the experimental setup.

corresponds to the (2,3) mode of the plate, was used when the thin aluminum plate with dimensions $71.2cm \times 60cm \times 0.3175cm$ was used as the primary source. The excitation point was located at (15 cm, 13.5 cm) left of the center of the plate. In this case, the surface velocity of the plate was measured over 441 points over the aluminum plate with Polytec Laser Vibrometer model OFV 1102.

2. The surface velocity normal to the primary source was evaluated either by piston theory (for 6" speaker) or by direct measurement from a laser vibrometer (for rectangular aluminum plate). The acoustic pressure on the cancellation plane was calculated and compared with experimental measurements in a previous step.

3. The sizes and locations of the secondary sources were pre-determined. The discretization of both primary and secondary sources were obtained for the noise cancellation technique.

4. The noise cancellation technique using BEM was applied numerically when the normal surface velocity of the primary source was identified in step 2.

5. The numerical simulation of the noise cancellation technique returned the excitation functions for each of the secondary sources for the specific configuration.

6. The acoustic pressure on the cancellation plane was calculated numerically with the addition of the secondary sources which were activated by the excitation functions specified in a previous step.

7. The noise reduction level for the cancellation plane was evaluated by comparing

the acoustic pressure at every specified field point calculated before (step 2) and after (step 6) the secondary sources were applied. Consequently, the regions of the best noise cancellation over the cancellation plane and the maximum noise reduction level were obtained numerically.

8. The excitation functions for each secondary source were generated by a 4-channel digital/analog converter (a module in the Masscomp 5400 computer) according to the solutions returned by the numerical simulation in step 5. The excitation functions were fed into the four speakers individually.

9. The acoustic pressure over the cancellation plane was measured experimentally in the same way described in the measurement procedures.

10. The experimental noise reduction level for the cancellation plane was evaluated from the acoustic pressure measurements before (step 1) and after (step 9) the secondary sources were added.

11. The results from experimental measurements were compared with those from the numerical simulations to investigate the validity of the noise cancellation technique.

It should be noted that the experimental results only confirmed the results of the noise cancellation from the numerical simulations. Therefore, the comparison between experimental and numerical solutions (in step 11) should agree satisfactorily. Nevertheless, the noise reduction over the cancellation plane for the configuration used was not necessarily the best noise reduction one might achieve when other configurations could have been used.

## 5.2 Noise Source with a Constant Velocity Distribution

A 6" speaker was used to simulate the noise source with constant surface velocity. The speaker which radiated acoustic noise into the upper half of an infinite space was mounted in an $8' \times 8' \times 0.25$" plywood baffle inside an anechoic chamber. The noise cancellation technique was applied on a cancellation plane 20 cm above the baffle plane with the dimensions $120cm \times 120cm$ where 961 field points were specified over the plane. The theory of the baffled piston with uniform surface velocity was used to simulate the speaker source. However, the surface velocity of the speaker source was not directly measurable. Furthermore, the surface of the speaker was cone shaped instead of a flat surface which was assumed in the piston theory. Consequently, it was impractical to control the surface velocities of the speakers directly. On the other hand, it was convenient to control the output acoustic field of the speakers by properly controlled input voltages to the speakers. Therefore, the input voltage to the speaker was controlled to generate the desired excitation function for the speaker. The surface velocity of the speaker was evaluated from the input voltage to the speaker and the output acoustic field of the speaker as follows:

1. The acoustic pressure radiated by the speaker was measured over a plane parallel to the baffle. It was confirmed that at low frequencies the speaker radiation agreed reasonably well with a baffled piston theory.

2. The acoustic pressure on the cancellation plane was measured experimentally by the measurement procedures described in the previous section with pre-selected input voltage fed into the speaker.

3. The acoustic pressure on the cancellation plane was calculated according to the baffled piston theory with uniform surface velocity assumed at certain frequency.

4. The numerical and experimental acoustic pressure in steps 2 and 3 were compared to evaluate the equivalent function between the input voltage to the speaker and the uniform surface velocity of the speaker. It should be noted that the equivalent function was assumed to be linear.

5. The surface velocity of the speaker source was calculated from the measured acoustic pressure and the equivalent function obtained from the previous step by the relation

$$\text{Actual surface velocity} = \frac{\text{Experimental pressure}}{\text{Numerical pressure}} \times \text{Assumed surface velocity}$$

$$\text{Desired input voltage} = \frac{\text{Desired surface velocity}}{\text{Actual surface velocity}} \times \text{Assumed input voltage.}$$

6. The evaluated surface velocity of the speaker source was applied to the baffled piston theory to calculate the acoustic pressure on the cancellation plane. The result of the acoustic pressure on the cancellation plane from the numerical simulation was compared with the experimental result from step 2 to identify the validity of using baffled piston theory for speaker source.

The block diagram for the evaluation of the equivalent function is shown in Figure 5.3. The evaluation procedures of the surface velocity of the speaker source were performed for both the 6" speaker and the four 10" speakers, respectively, in order to identified the equivalent functions for each individual speaker source. In addition,


(a) The block diagram for numerical acoustic pressure evaluation


(b) The block diagram for experimental acoustic pressure measurement

Figure 5.3: The block diagram for the evaluation of the equivalent function

the same procedures were applied with four 10" speakers being activated simultaneously such that the linearity of the speakers was justified. The results for the equivalent function evaluation of one speaker and four speakers at 100 Hz were shown in Figures 5.4 and 5.5, respectively. The same procedures were also applied at 1000 Hz and 2000 Hz because the evaluated equivalent function would be frequency dependent. It was necessary to evaluate the equivalent function of the speaker source at different frequencies when the noise cancellation technique was applied at various frequencies. It should be noted that the simulation of the speaker source to the baffled piston theory at higher frequencies was not as good as that at lower frequencies as shown in Figures 5.6 and 5.7. The reason is that at higher frequencies various modes of diaphragm vibration occurred. Therefore, the surface velocity of the speaker source was far from being uniformly distributed. Consequently, discrepancies showed up when the acoustic pressure from the speaker source was compared with that from baffled piston theory at high frequencies as expected.

The evaluated surface velocity of the 6" speaker source was applied to the noise cancellation technique along with the discretization of secondary sources which were the four 10" speakers. Each speaker was discretized into 49 nodes and 16 surface elements. Therefore, there were 245 nodes with 80 surface elements for both the 6" and 10" speakers. The noise cancellation at three different frequencies were tested. The chosen frequencies were 100 Hz, 1000Hz and 2000 Hz. In addition, two cancellation planes were selected for the noise cancellation at the center and around a ring region. There were 961 field points specified over a $120cm \times 120cm$ plane at 20 cm above the baffle plane for the cancellation at the center. However, only 160 field points were specified over an annular rings with radius 20cm to 52cm at 20 cm above the baffle

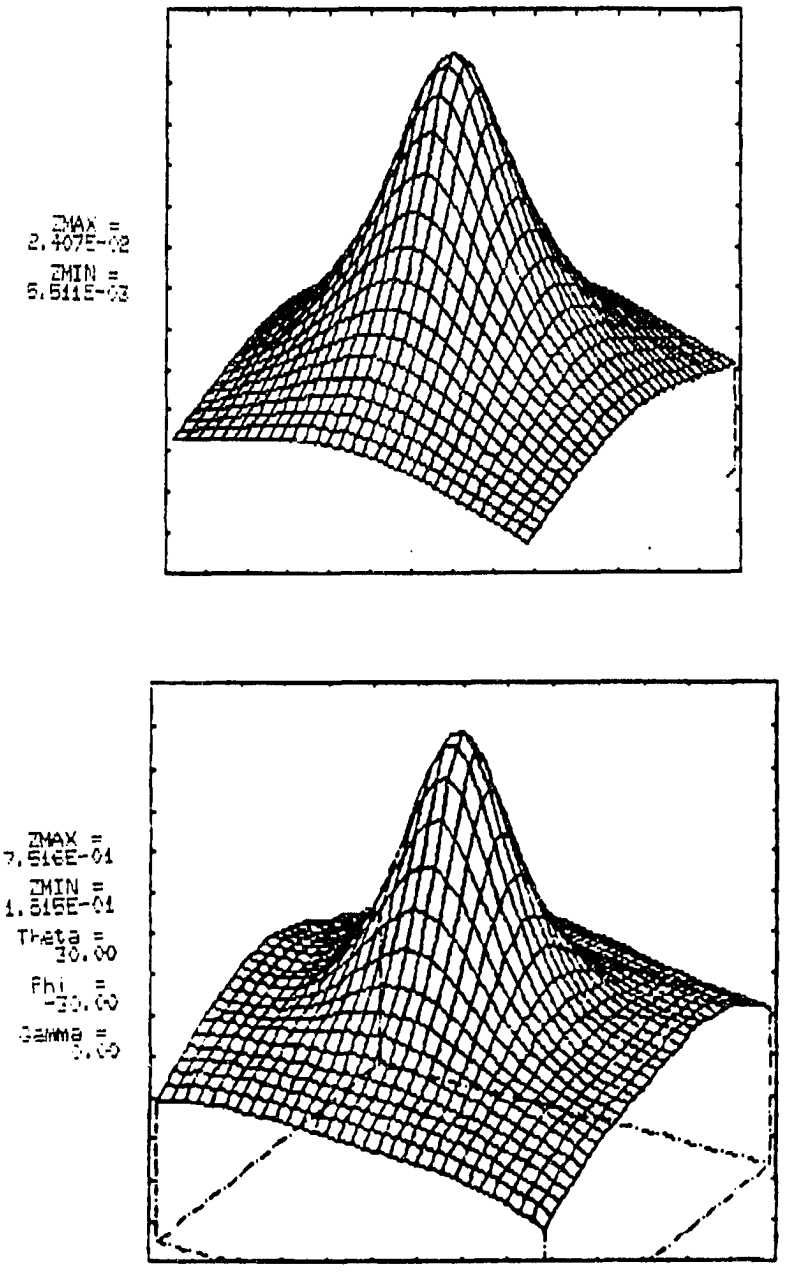


Figure 5.4: Theoretical and experimental pressure on cancellation plane for 6" speaker at 100 Hz. top: theoretical, bottom: experimental.

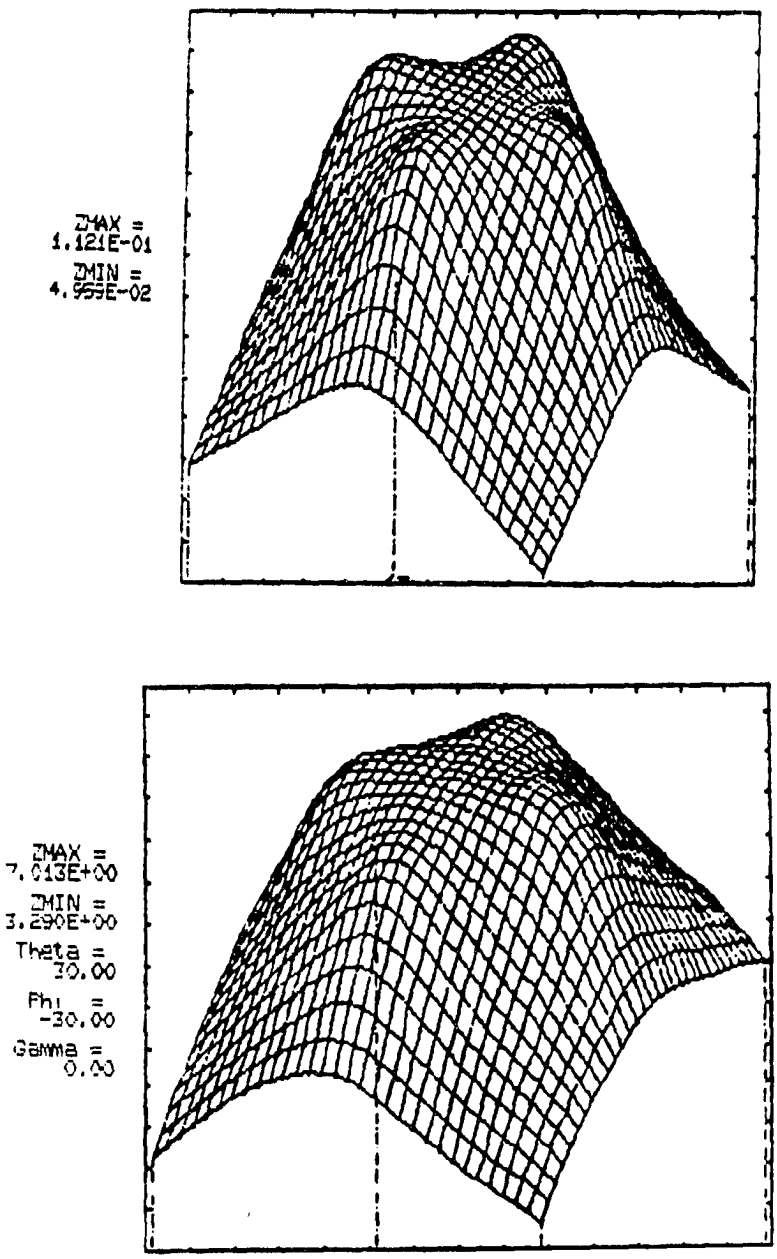


Figure 5.5: Theoretical and experimental pressure on cancellation plane for four 10" speakers at 100 Hz. top: theoretical, bottom: experimental.

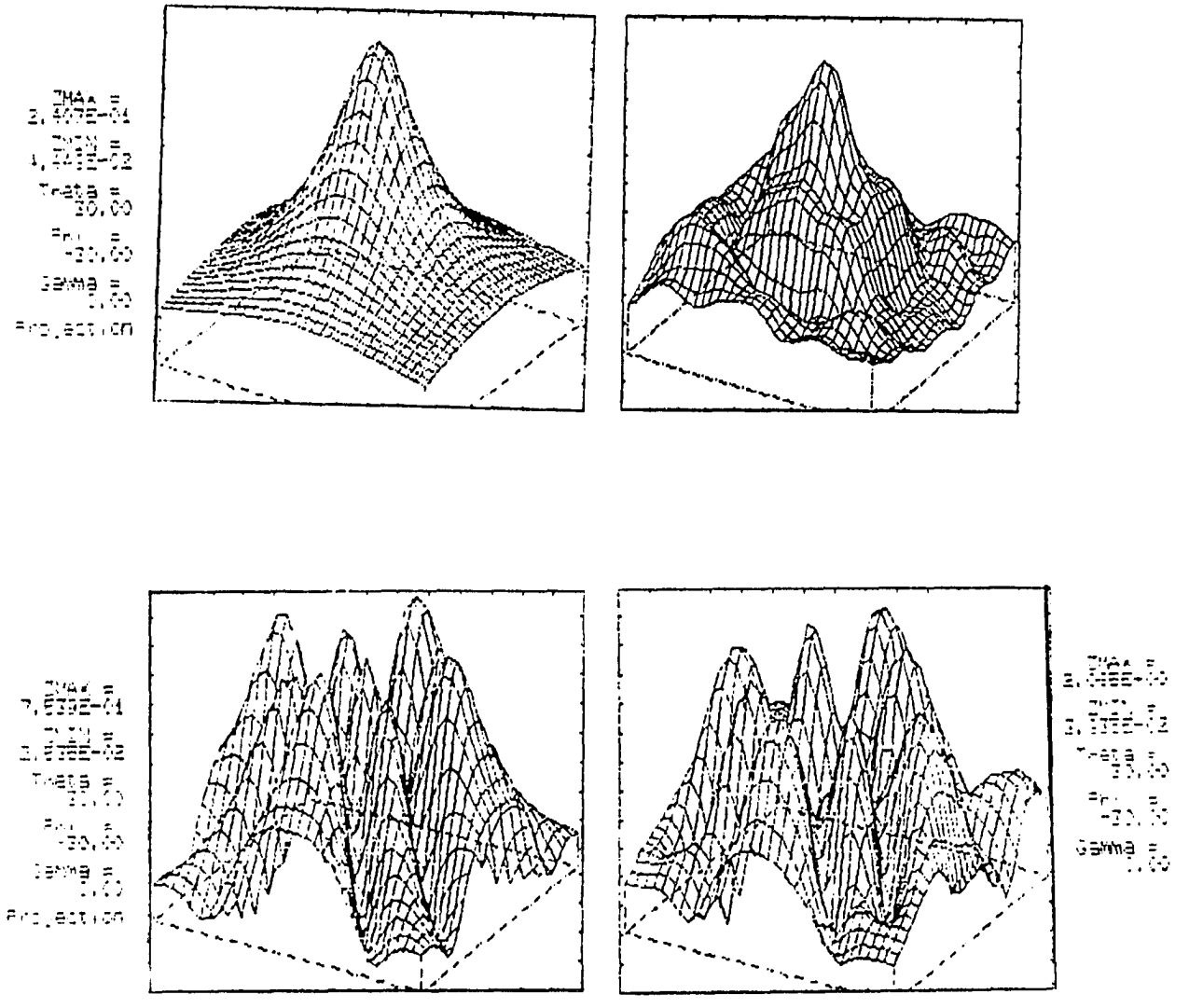

Figure 5.6: Theoretical and experimental pressure on cancellation plane for 6" and four 10" speakers at 1000 Hz; for 6" speaker: top left: theoretical, top right: experimental; for 10" speakers: bottom left: theoretical, bottom right: experimental.

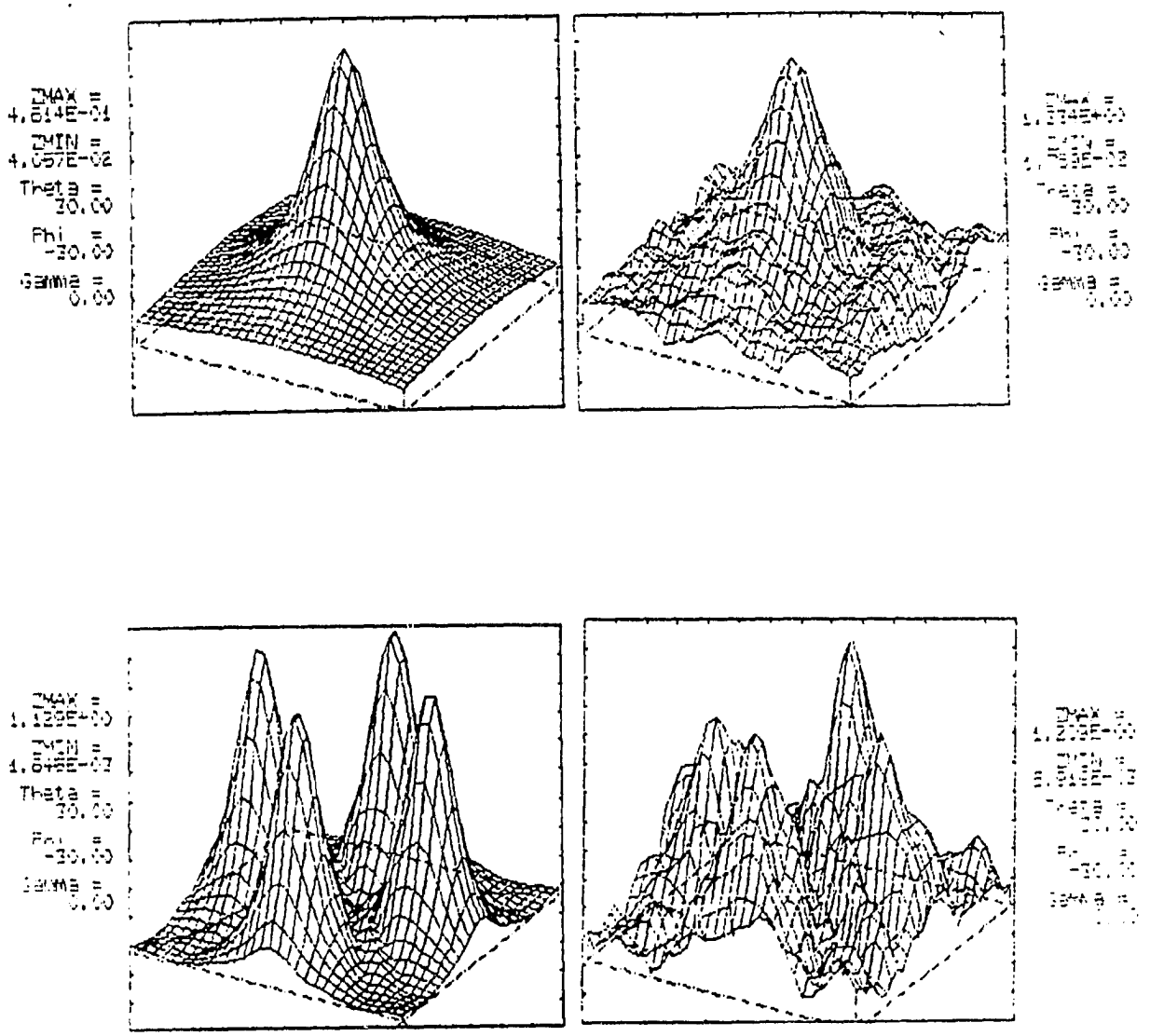


Figure 5.7: Theoretical and experimental pressure on cancellation plane for 6" and four 10" speakers at 2000 Hz; for 6" speaker: top left: theoretical, top right: experimental; for 10" speakers: bottom left: theoretical, bottom right: experimental.

plane for the cancellation around the ring region. The experimental configuration is shown in Figure 5.8. The noise cancellation technique returned the required surface velocity for each of the secondary sources. The calculated surface velocity of the secondary sources were almost identical, which will be shown in the following figures, because the configuration of the sources was axisymmetric. The equivalent functions of the secondary sources were used to convert the calculated surface velocity into desired input voltage to each secondary source. The digital/analog converter generated the input voltage to each speaker. It should be noted that the Masscomp 5400 computer generates signals of the same frequency but different amplitudes and phases for the primary and secondary sources. The transfer functions of each path ( including cables and the equipment along the path) should be carefully evaluated in advance such that the mismatch among each path can be eliminated. Finally, the acoustic pressure on the cancellation plane was measured by the 2-D scanner system with the four secondary sources activated. The measured acoustic pressure was compared with the pressure from the primary source (6" speaker) only. The noise reduction level on the cancellation plane was then evaluated. The results of noise reduction from the experimental measurements should match with those from the numerical simulation which were obtained before the measurements.

The measured acoustic pressure and the noise reduction level on the cancellation plane agreed well with the results from numerical predictions where noise cancellation at the center of the plane was observed at 100 Hz as shown in Figures 5.9-5.10. However, the numerical simulation predicted almost 34 dB maximum noise cancellation where only 17.5 dB maximum noise reduction was observed from the measurements. The discrepancy was mainly attributed to experimental error which occurred in

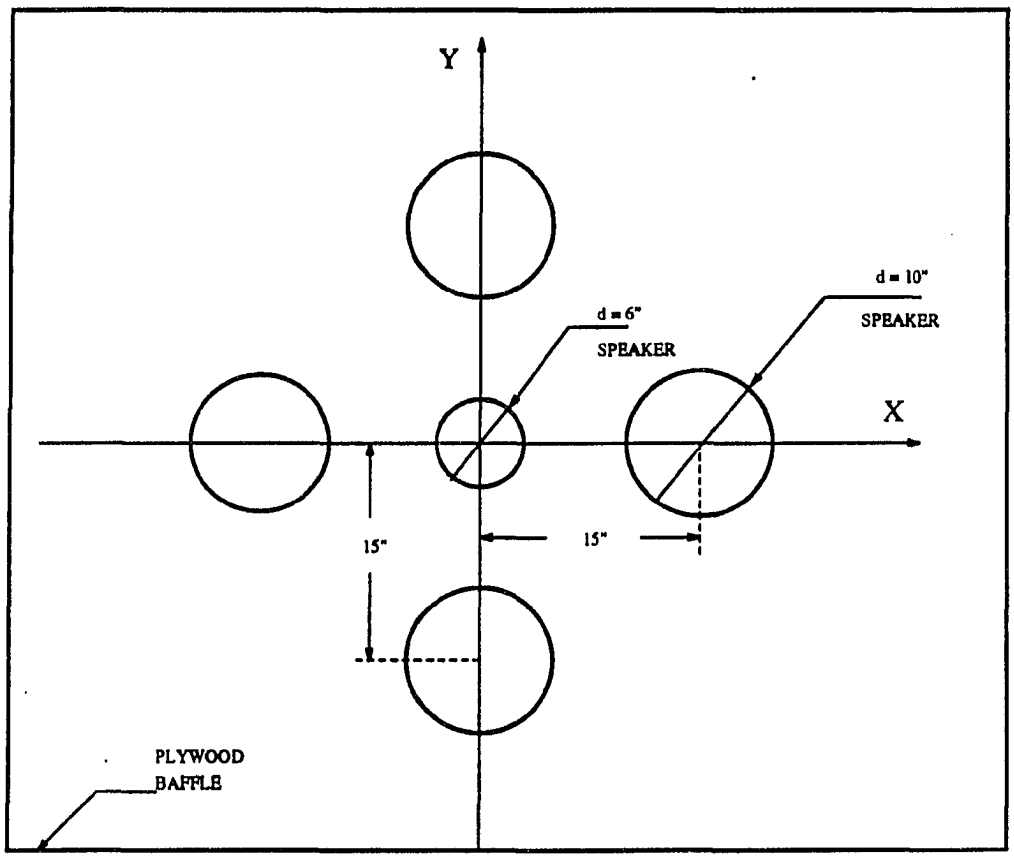


Figure 5.8: The experimental configuration for noise cancellation technique.

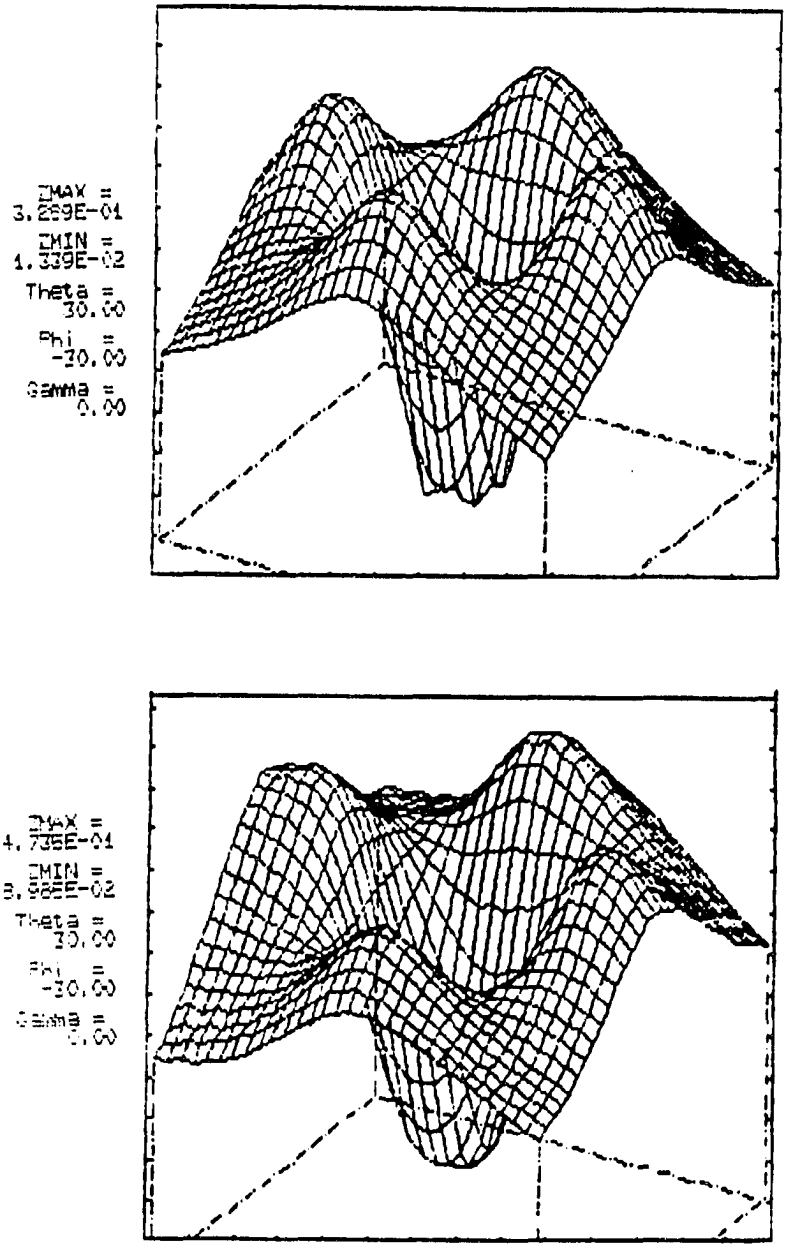


Figure 5.9: Theoretical and experimental pressure canceled at the center of the cancellation plane at 100 Hz using configuration of Figure 5.8 and driving functions (8.2871, 30.9280) m/s for primary source, (-1.3887, -3.8042) m/s for four secondary sources. top: theoretical, bottom: experimental.

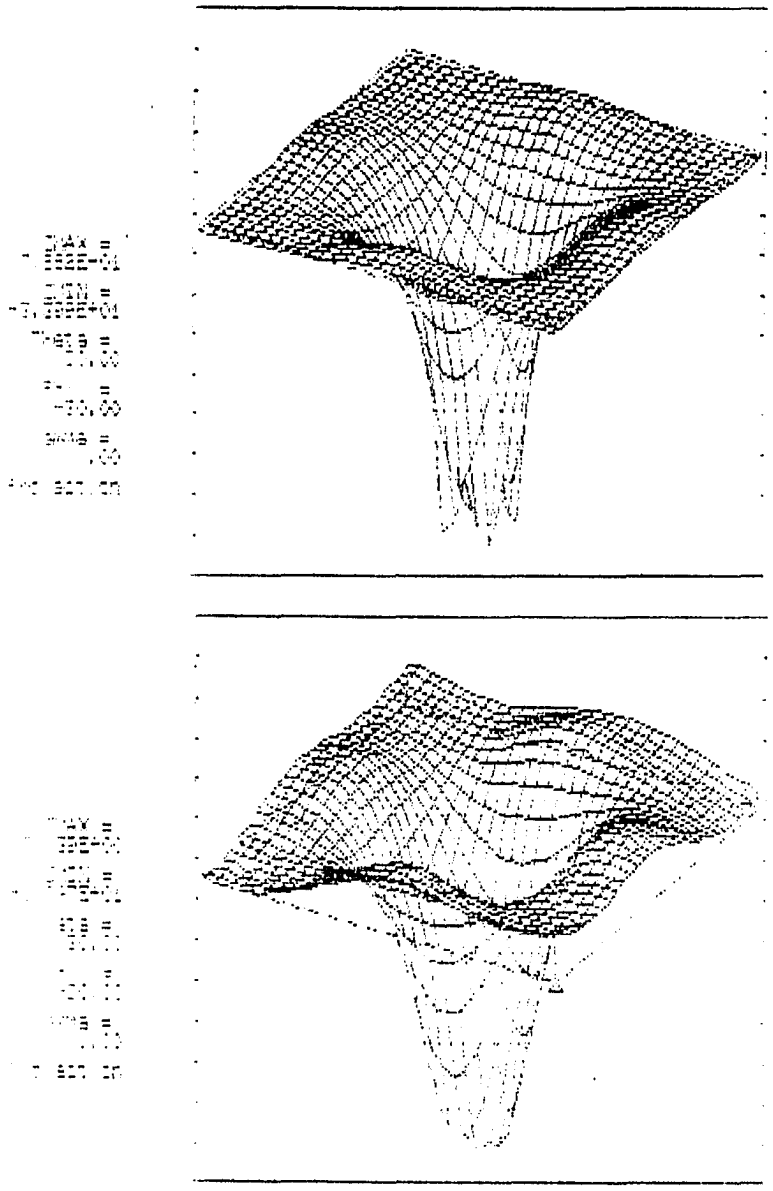

Figure 5.10: Theoretical and experimental pressure canceled at center (in dB scale) on cancellation plane at 100 Hz using configuration of Figure 5.8 and driving functions (8.2871, 30.9280) m/s for primary source, (-1.3887, -3.8042) m/s for four secondary sources. top: theoretical, bottom: experimental.

phase mismatch of the excitation functions of primary and secondary sources.

The results for noise cancellation around a ring region were shown in Figures 5.11 and 5.12 for a frequency of 100 Hz. It was noted that the numerical simulation predicted only 36 dB maximum noise cancellation. However, the experiments showed 42.5 dB maximum noise reduction. The difference between experimental and numerical simulation results was possibly due to the experimental signals being very small near the region of cancellation on the plane. Therefore, the signal measured at those points were not very reliable. This might be the reason why the noise reduction level was extremely good in the neighborhood of the cancellation region. Despite the discrepancy for the maximum noise reduction, the match between numerical simulation and the experimental measurements was extremely good.

The same experimental procedures were performed on the same configuration of source distribution with 1000 Hz and 2000 Hz. Figures 5.13 and 5.14 show the results of noise cancellation at the center region at 1000 Hz both numerically and experimentally. In addition, the results for noise cancellation around a ring region at 1000 Hz are shown in Figures 5.15-16. It should be noted that better noise cancellation levels were observed in the experimental measurements than in the numerical simulations. However, the noise reduction patterns for the test cases presented here matched very well numerically and experimentally. On the other hand, Figures 5.17-18 presented the results of noise cancellation around the center region of the cancellation plane at 2000 Hz while Figures 5.19-20 denoted the noise cancellation around a ring region at the same frequency. It should be noted that the experimental results always returned better noise cancellation levels than the numerical simulation did. The main reason

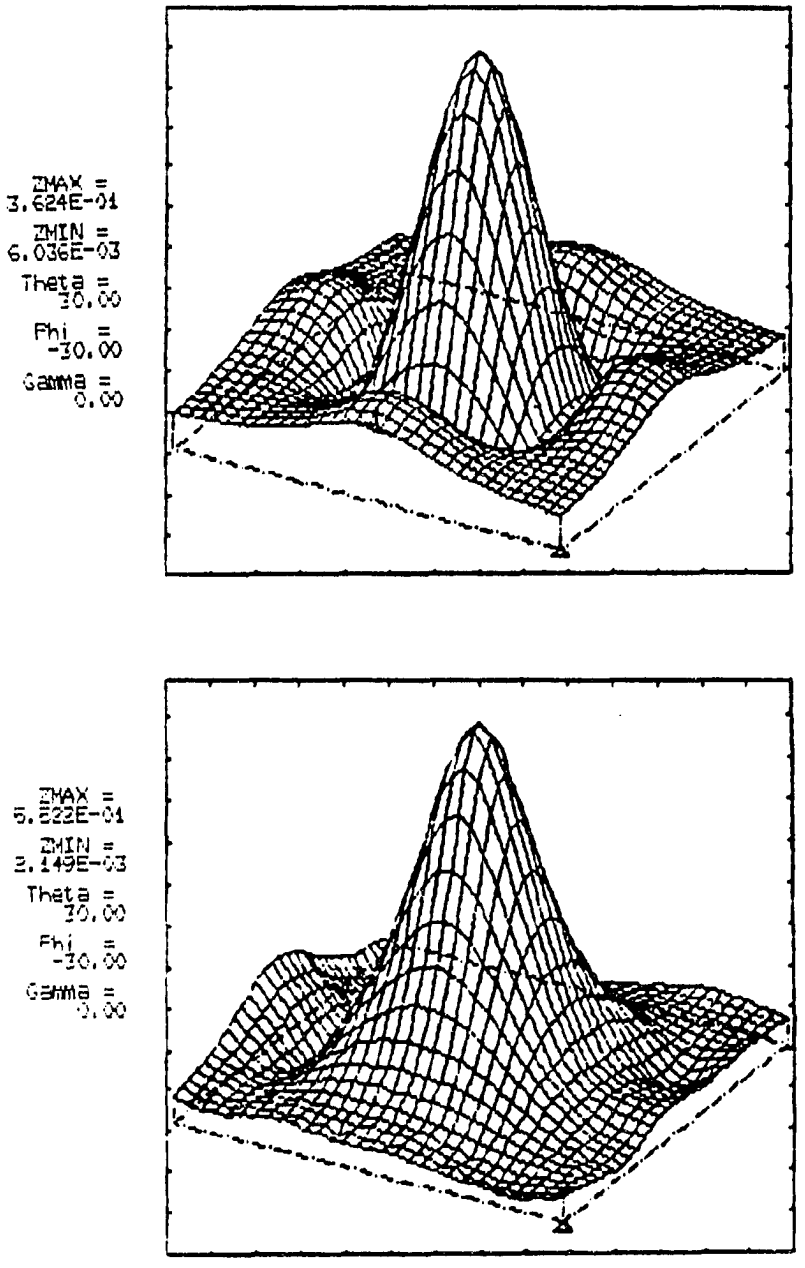


Figure 5.11: Theoretical and experimental pressure canceled around ring on cancellation plane at 100 Hz using configuration of Figure 5.8 and driving functions (8.2871, 30.9280) m/s for primary source, (3.4984, 9.6117) m/s for secondary sources. top: theoretical, bottom: experimental.

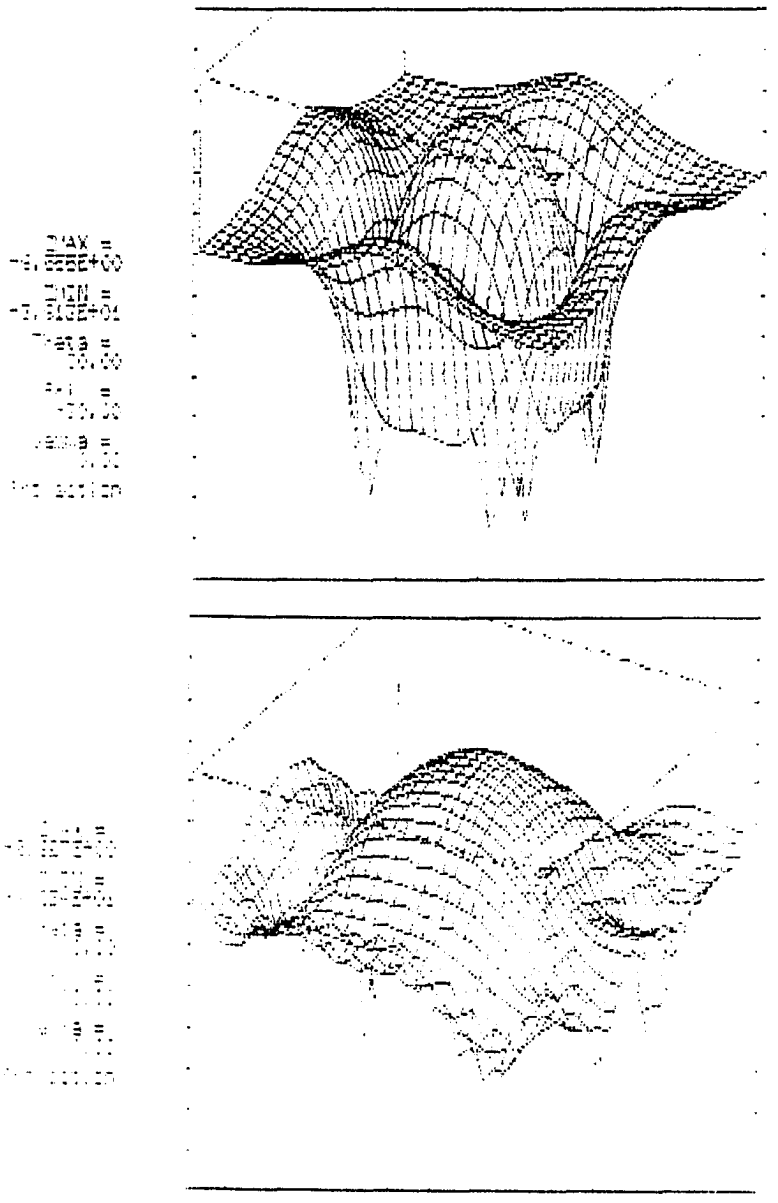

Figure 5.12: Theoretical and experimental pressure canceled around ring (in dB scale) on cancellation plane at 100 Hz using configuration of Figure 5.8 and driving functions (8.2871, 30.9280) m/s for primary source, (3.4984, 9.6117) m/s for secondary sources. top: theoretical, bottom: experimental.

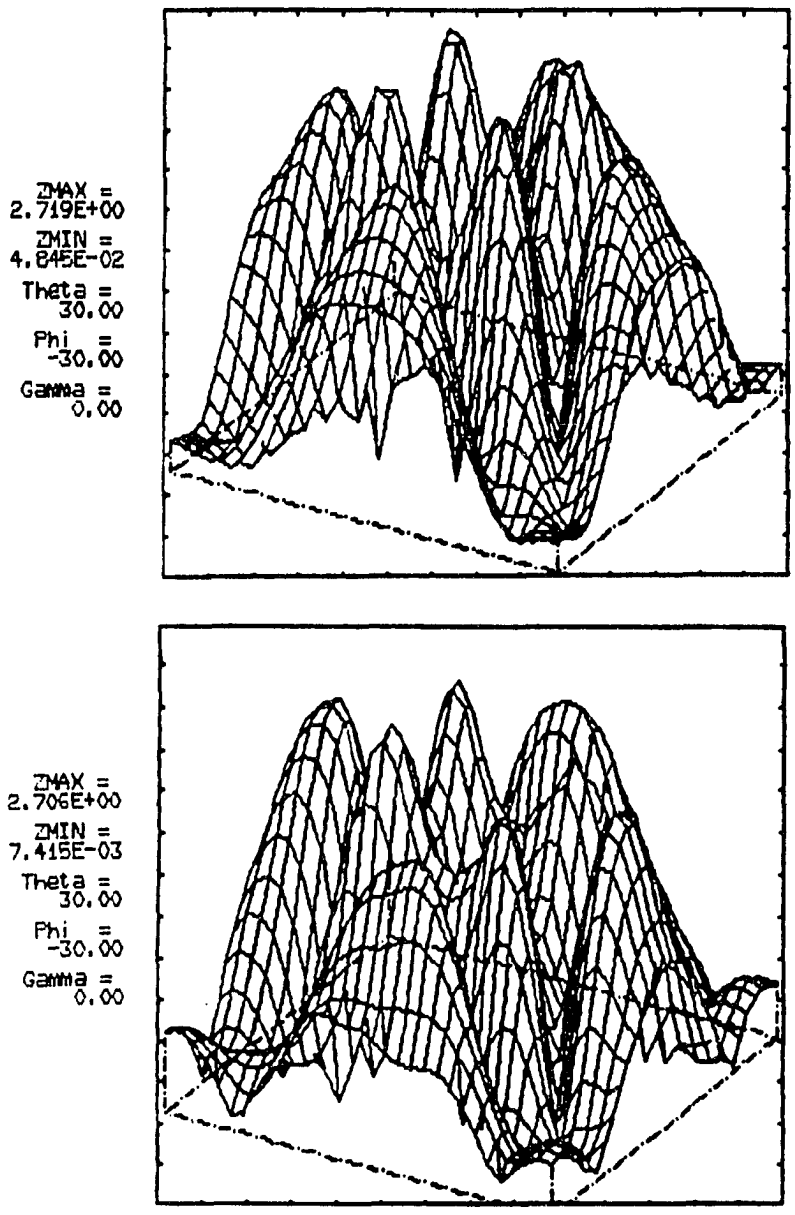


Figure 5.13: Theoretical and experimental pressure canceled at center on cancellation plane at 1000 Hz using configuration of Figure 5.8 and driving functions (-2.4763, 7.1931) m/s for primary source, (9.4537e-2, 1.7661e-2) m/s for four secondary sources. top: theoretical, bottom: experimental.

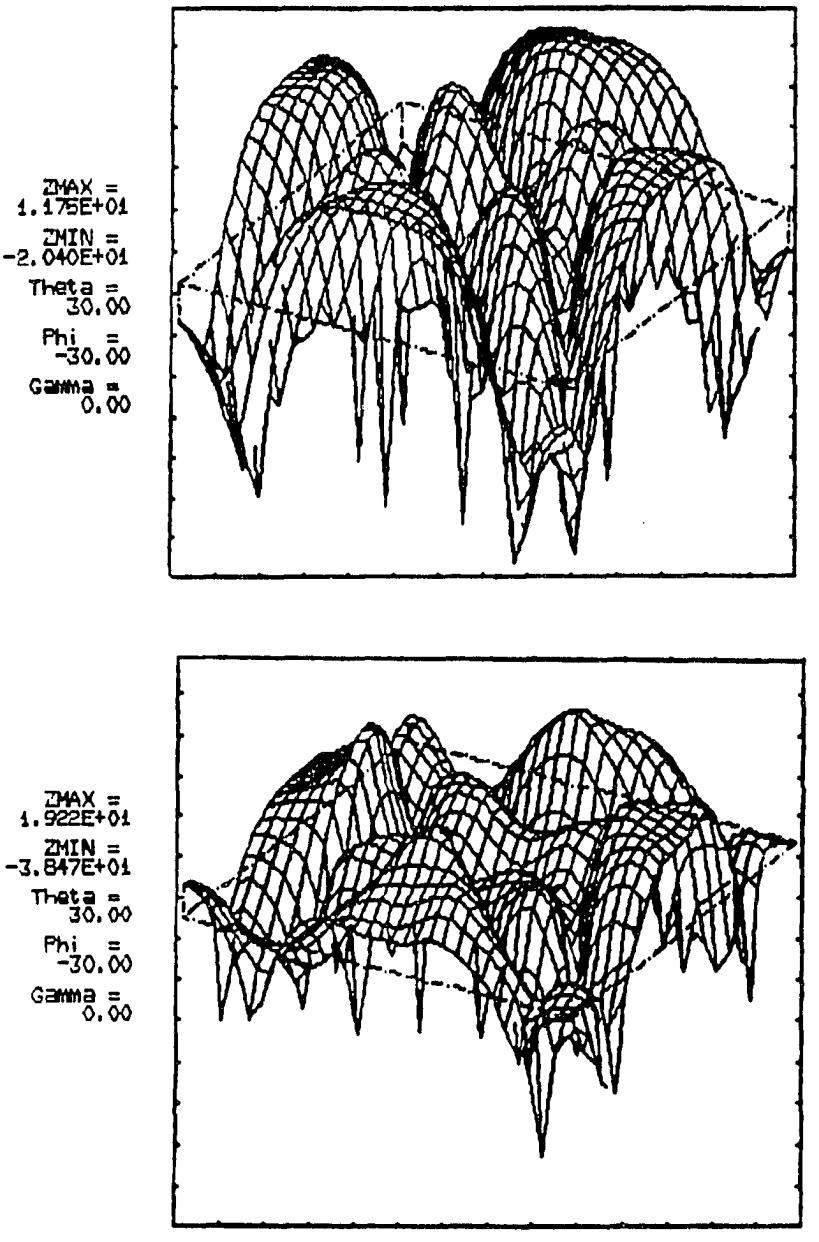


Figure 5.14: Theoretical and experimental noise reduction at center (in dB scale) on cancellation plane at 1000 Hz using configuration of Figure 5.8 and driving functions (-2.4763, 7.1931) m/s for primary source, (9.4537e-2, 1.7661e-2) m/s for four secondary sources. top: theoretical, bottom: experimental.

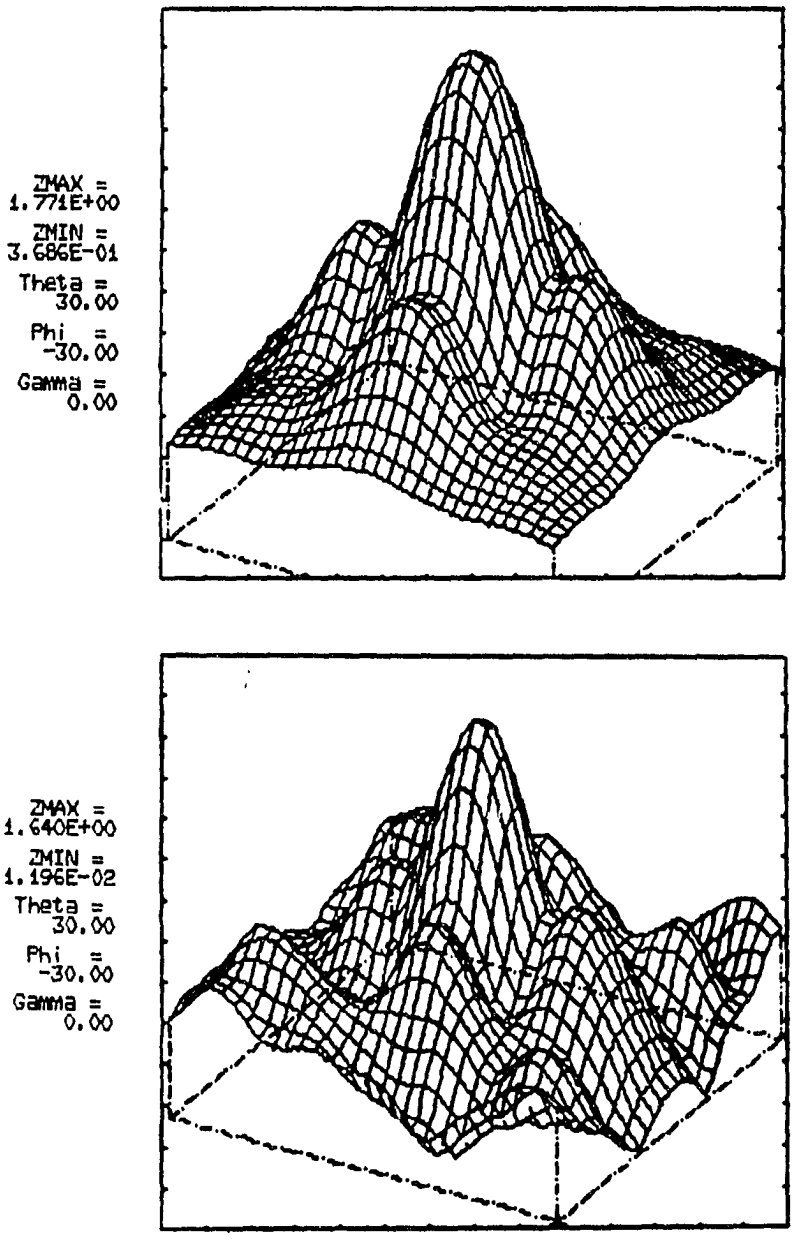


Figure 5.15: Theoretical and experimental pressure canceled around ring on cancellation plane at 1000 Hz using configuration of Figure 5.8 and driving functions (-2.4763, 7.1931) m/s for primary source, (0.2814, -0.1645) m/s for secondary sources. top: theoretical, bottom: experimental.

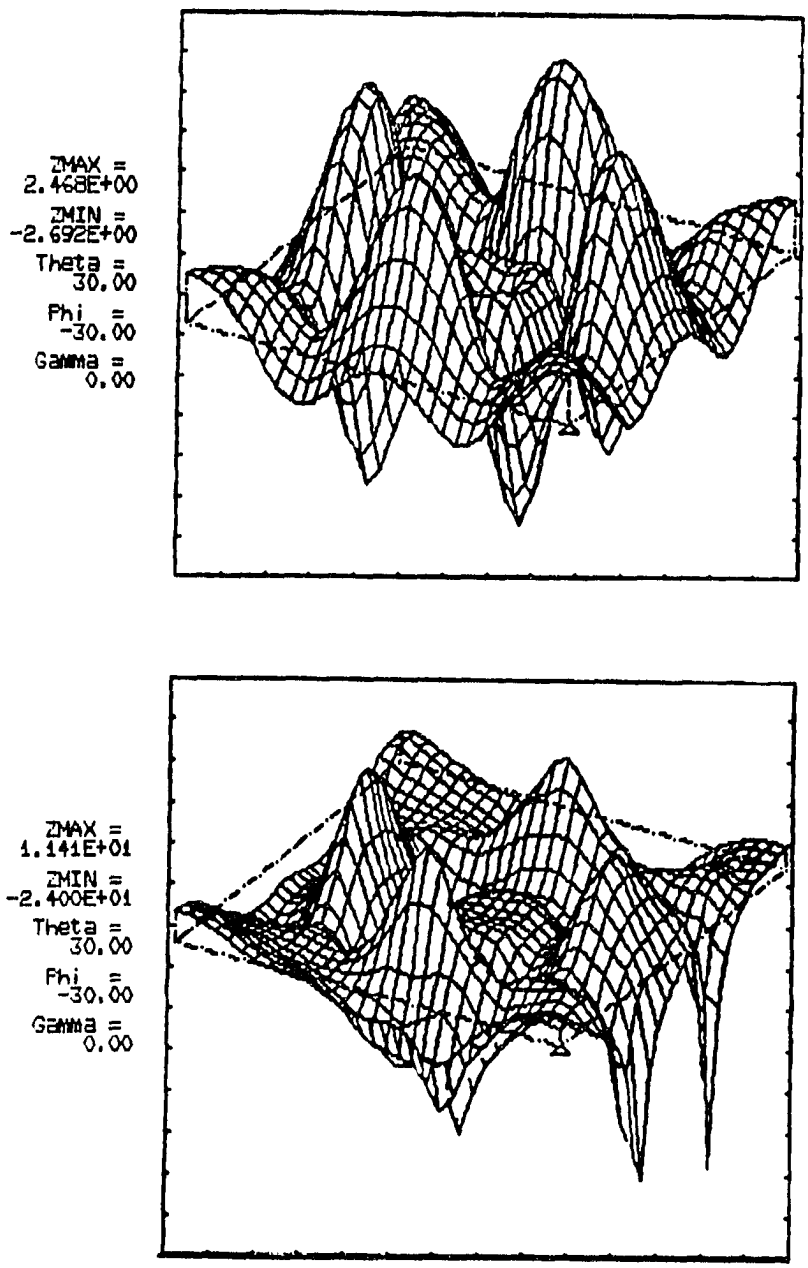


Figure 5.16: Theoretical and experimental noise reduction around ring (in dB scale) on cancellation plane at 1000 Hz using configuration of Figure 5.8 and driving functions (-2.4763, 7.1931) m/s for primary source, (0.2814, -0.1645) m/s for secondary sources. top: theoretical, bottom: experimental.

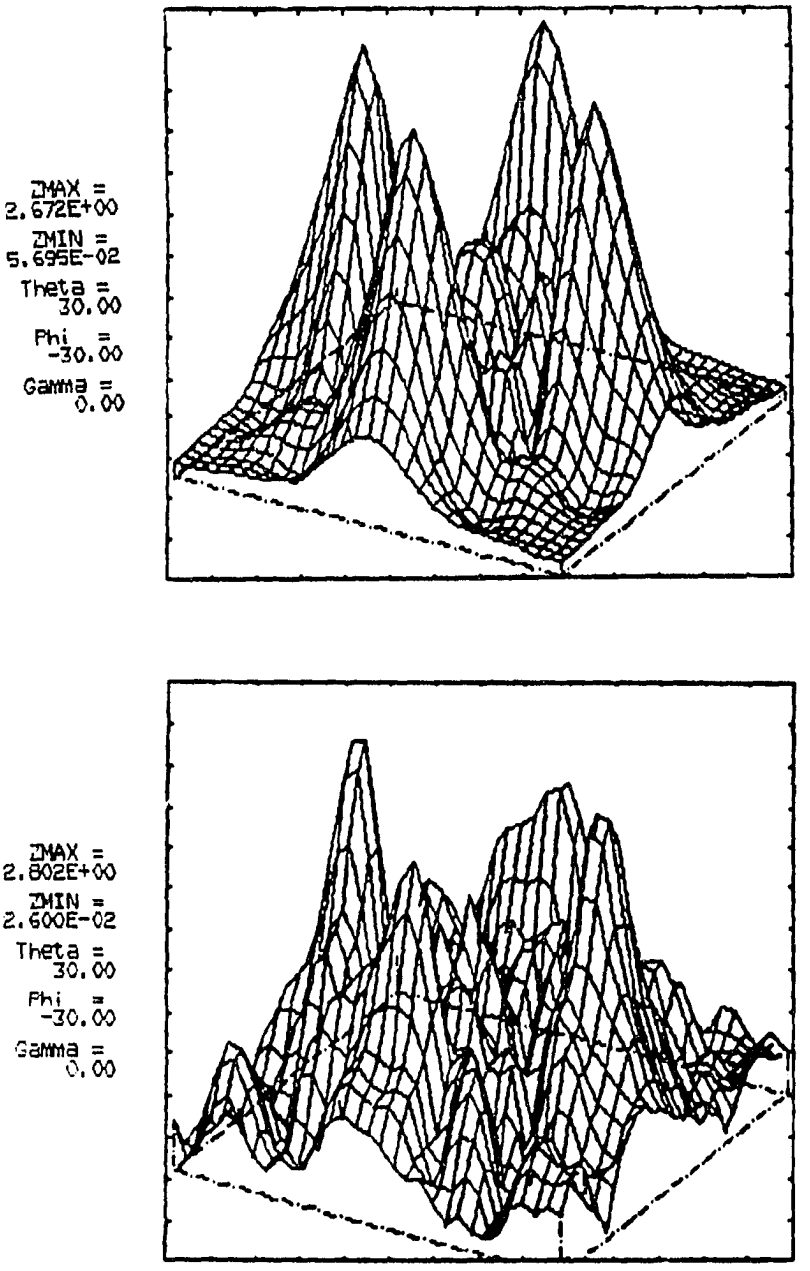


Figure 5.17: Theoretical and experimental pressure canceled at center on cancellation plane at 2000 Hz using configuration of Figure 5.8 and driving functions (-2.3025, 1.5417) m/s for primary source, (-1.8619, 1.6640) m/s for secondary sources. top: theoretical, bottom: experimental.

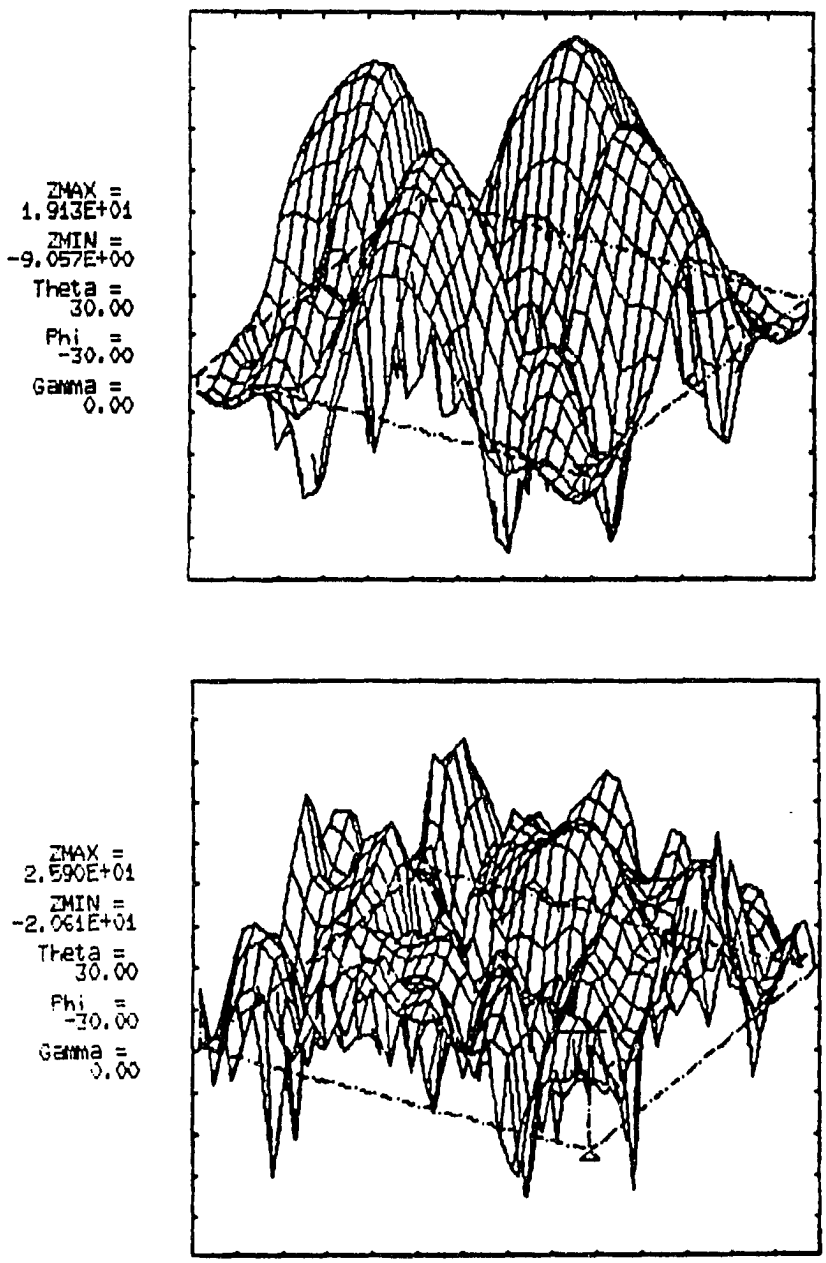


Figure 5.18: Theoretical and experimental noise reduction at center (in dB scale) on cancellation plane at 2000 Hz using configuration of Figure 5.8 and driving functions (-2.3025, 1.5417) m/s for primary source, (-1.8619, 1.6640) m/s for secondary sources. top: theoretical, bottom: experimental.

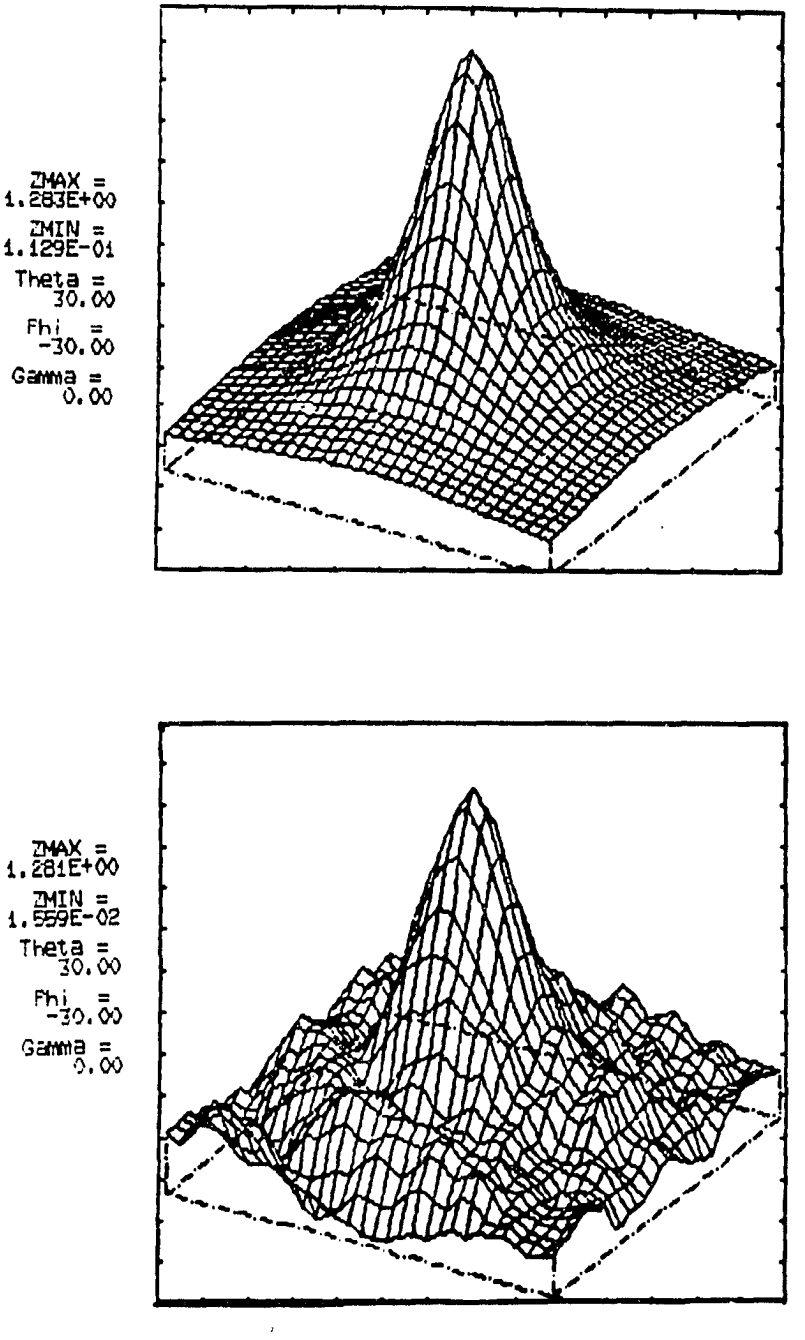


Figure 5.19: Theoretical and experimental pressure canceled around ring on cancellation plane at 2000 Hz using configuration of Figure 5.8 and driving functions (-2.3025, 1.5417) m/s for primary source, (-3.7888e-2, 5.7698e-3) for secondary sources. top: theoretical, bottom: experimental.

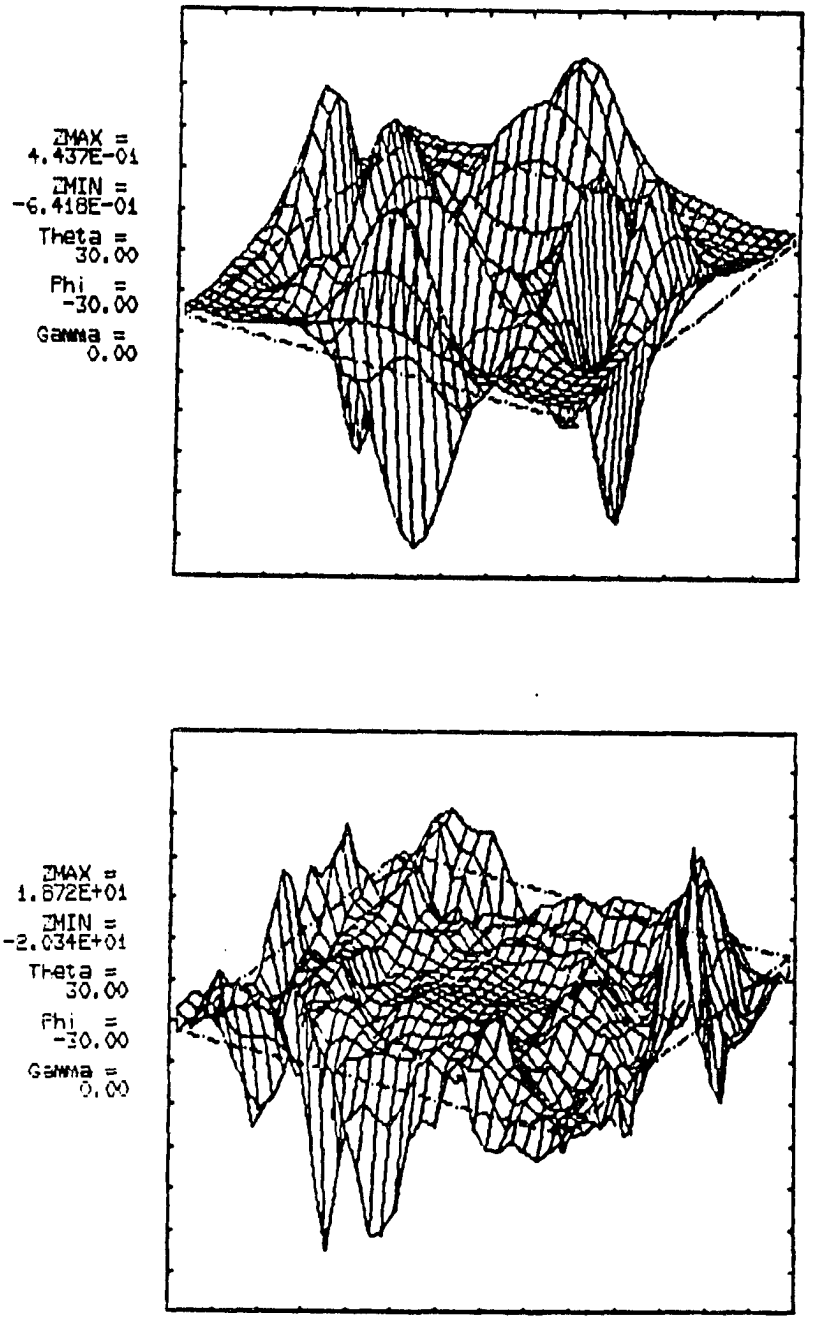


Figure 5.20: Theoretical and experimental noise reduction around ring (in dB scale) on cancellation plane at 2000 Hz using configuration of Figure 5.8 and driving functions (-2.3025, 1.5417) m/s for primary source, (-3.7888e-2, 5.7698e-3) for secondary sources. top: theoretical, bottom: experimental.

for the discrepancies shown here was because that the speaker sources were far from piston theory. The surface velocity of the speaker sources was not uniformly distributed at high frequencies. However, it was assumed that the surface velocity of the source was uniform in piston theory which was incorporated in the noise cancellation technique. Therefore, the piston theory was no longer adequate for the speaker source at high frequencies. It is not surprising that the noise cancellation patterns were not very similar between numerical simulations and the experimental measurements unless proper modifications were made to the noise cancellation technique in order to adopt the non-uniform surface velocity of the speakers. However, the noise cancellation in designated regions was still achieved for all the test cases conducted in this research.

In general, the noise cancellation technique provided satisfactory results of noise reduction in designated areas for the speaker sources when uniform surface velocity was assumed. The experimental results prove that active noise cancellation by BEM is feasible. However, the piston theory has to be modified to accommodate a non-uniform surface velocity distribution when high frequency noise cancellation is required using speaker sources.

## 5.3 Noise Source with Variable Velocity Distribution

A ribbed aluminum plate with dimensions $71.2cm \times 60cm$ was used to simulate the noise source with variable surface velocity. The aluminum plate was ribbed along its short side at 17.75 cm from one end of the plate. The surface velocity of the plate was not analytically predictable because of the rib attached to the plate. Therefore, the surface velocity of the plate had to be measured experimentally.

The aluminum plate was mounted in an $8' \times 8.5' \times 0.25$" plywood baffle inside the anechoic chamber. The plate was sinusoidally driven by a 10-lb shaker attached at a point (15 cm, 13.5 cm) from its center such that the plate radiated undesirable acoustic noise into the upper half of the chamber. Four 10" speakers were used as secondary sources to cancel the noise from the plate provided that proper excitation functions for each speaker were carefully controlled. The secondary sources were mounted around half of the plate because the total surface area of the secondary sources was too small to cancel the acoustic noise on a large cancellation plane produced by the primary source which had a relatively large surface area. Therefore, it was desired that the secondary sources should cancel the acoustic noise on a smaller cancellation plane. Consequently, the plane at 5 cm above the baffle plane with the dimensions $120cm \times 60cm$ was chosen to be the cancellation plane where 496 field points were specified. The experimental setup was similar to that shown in Figure 5.8 except for the plate source and the locations of the speaker sources.

The surface velocity of the plate was measured at 441 points distributed uniformly over the plane $70cm \times 69cm$ out of the entire plate using a Polytec laser vibrometer model OFV1102 with reflective paint coated uniformly over the entire surface of the plate. The surface velocity of the very edge of the plate was neglected because of the low signal-to-noise ratio. The distribution of the surface velocity of the ribbed plate is shown in Figure 5.21. However, only 181 points out of 441 measured points were used to evaluate the acoustic pressure on the cancellation plane. The actual pressure on the cancellation plane was experimentally measured and compared with the result from the numerical simulation. It showed very good agreement between the experimental and numerical results as shown in Figure 5.22.

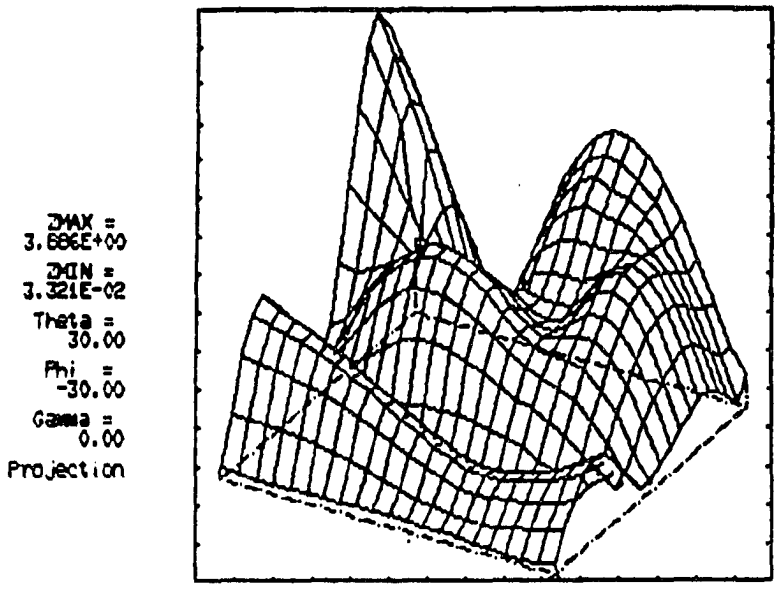


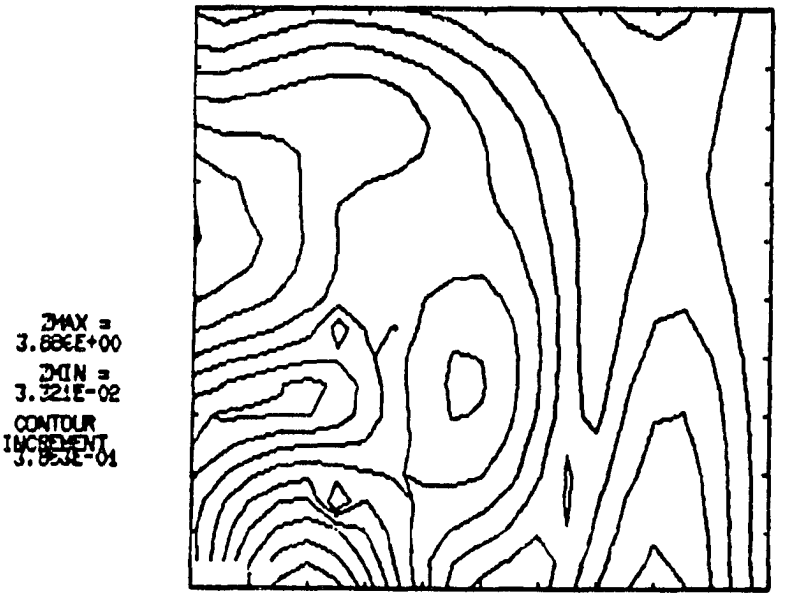


Figure 5.21: Plate surface velocity measured by laser at 150 Hz.

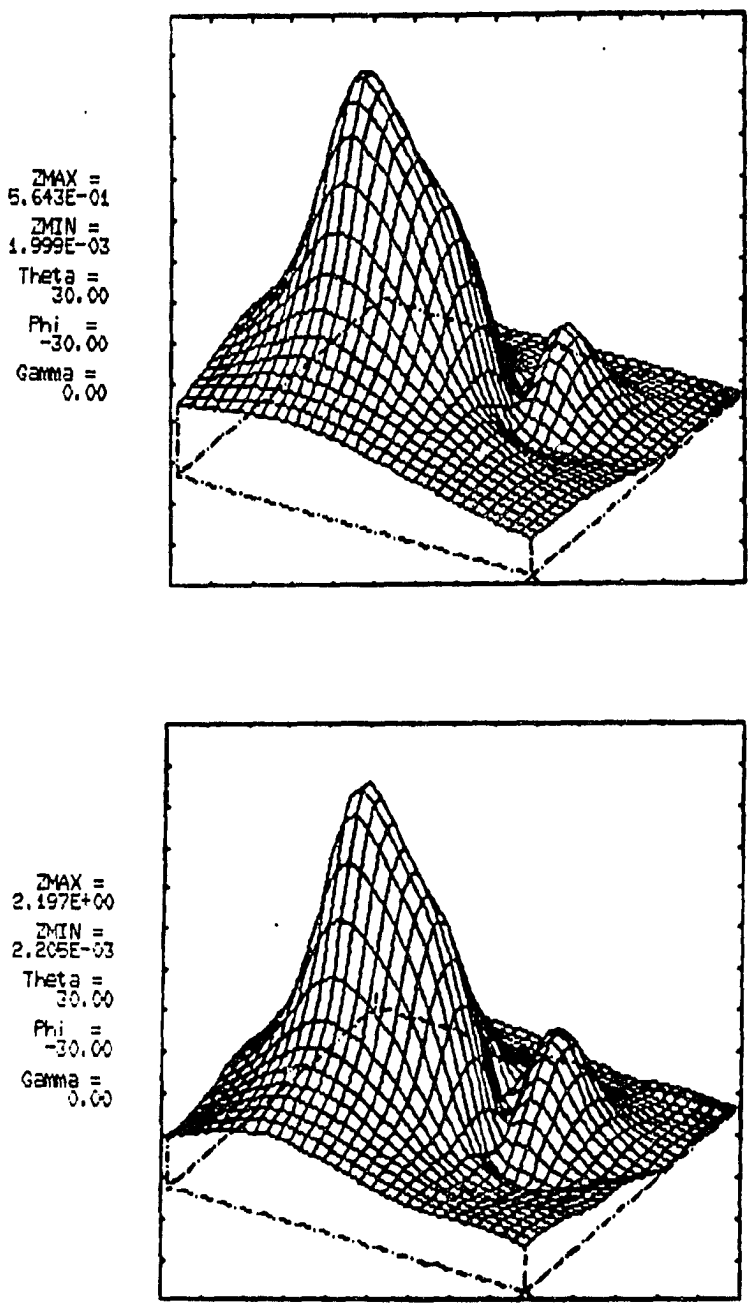


Figure 5.22: Theoretical and experimental pressure magnitude on cancellation plane at 150 Hz generated by a ribbed plate. top: theoretical, bottom: experimental.

However, the acoustic pressure on the cancellation plane was not symmetric due to the plate being ribbed on one side. It was also shown that the acoustic pressure on the ribbed side was smaller in magnitude than the other side which was not ribbed.

The locations of the secondary sources were chosen arbitrarily as shown in Figure 5.23. The speakers were discretized into 196 nodal points and 64 surface elements with the assumption that they behaved like baffled pistons. The noise cancellation technique was applied to the configuration described above at 150 Hz where the (2,3) mode of the plate was observed. The solutions returned by the numerical simulation were the surface velocities of the secondary sources for that particular source distribution configuration. It is obvious that the surface velocity of the secondary sources varied significantly from one another because the primary source was a ribbed plate. The two secondary sources near the ribbed side of the plate required much smaller surface velocities than those of the other two secondary sources near the unribbed side of the plate. The acoustic pressure on the cancellation plane produced by the four speakers with the evaluated surface velocities was calculated. In addition, the acoustic pressure on the same plane was measured by a quarter-inch microphone and the data acquisition system described in a previous section with designated input voltages to each speaker in order to evaluate the equivalent function between the surface velocity of the speakers and the input voltages to the speakers. The equivalent function evaluated here is different from those evaluated in the previous section because of different frequencies and configuration of the secondary sources are used. It should be noted that the digital/analog converter had to be expanded to five channels because five independent signals were required for the ribbed plate and four speakers. In addition, five power amplifiers were needed for the five signals respectively.

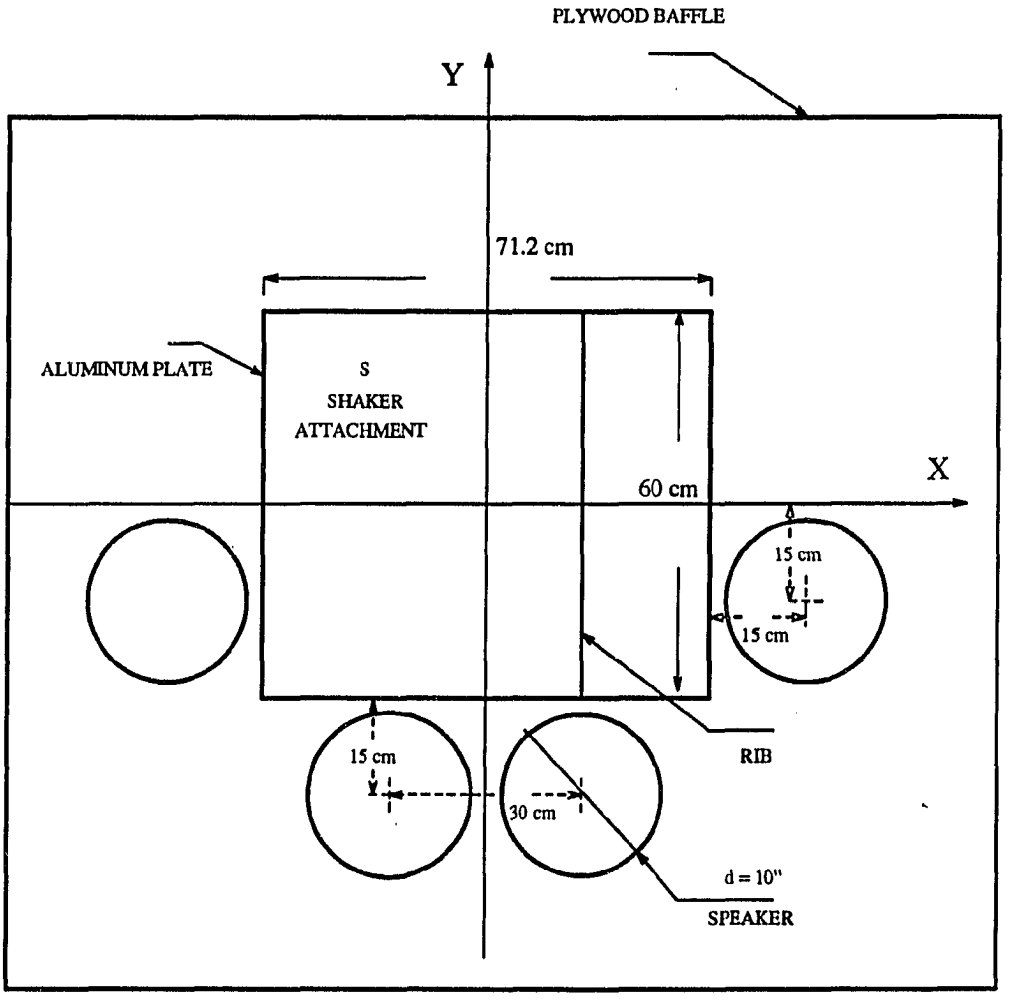


Figure 5.23: The configuration of plate noise cancellation.

Calibration of magnitudes and phases for the five power amplifiers was done before the experiment was conducted and the mismatchs among them were recorded. The numerical simulation and measurement of the acoustic pressure on the cancellation plane for the four speakers are presented in Figure 5.24. It should be noted that the measurement showed higher peaks than the results from the numerical solution near the second speaker. However, the magnitude of the acoustic pressure near the fourth speaker was smaller for the experimental result than the numerical one. In general, the acoustic pressure on the cancellation plane showed satisfactory agreement between the experimental and numerical results.

The acoustic pressure on the cancellation plane was evaluated numerically with the ribbed plate and the four speakers activated simultaneously. The surface velocity of the ribbed plate was kept unchanged from the laser measurement while the surface velocities of the speakers were obtained from the noise cancellation technique. The result from the numerical simulation of the noise cancellation is shown in Figure 5.25. On the other hand, the input voltages for the speakers were calculated according to the equivalent function evaluated previously to account for the required surface velocities of the speakers calculated from the noise cancellation technique. The phase of each input voltage to the speaker was generated by the Masscomp 5400 computer relative to the input voltage to the ribbed plate. The result from the experimental measurement of the noise cancellation was also presented in Figure 5.25. It could be shown that the agreement between these two results was excellent except for some minor discrepancies due to the experimental error. In addition, the noise reduction level was obtained by comparing the acoustic pressure on the cancellation plane before and after the secondary sources were added. The numerical simulation and

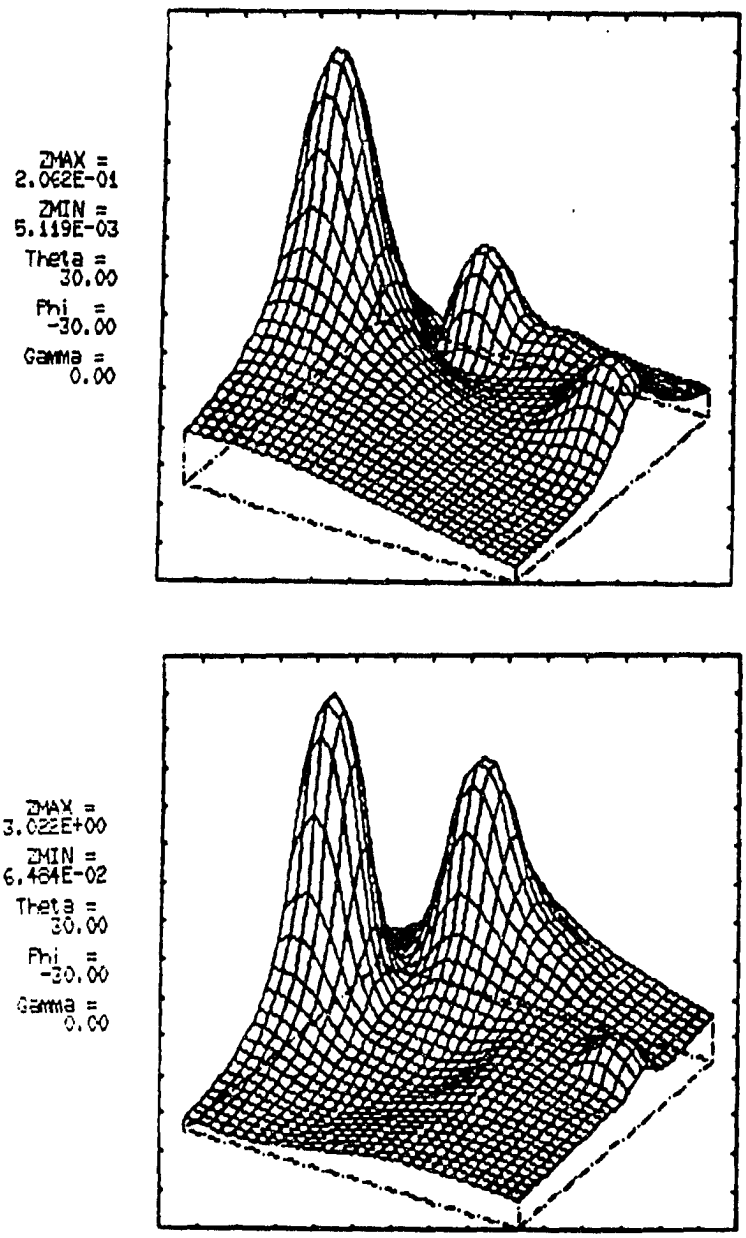


Figure 5.24: Theoretical and experimental pressure magnitude (in Pascal) from four 10" speakers on cancellation plane at 150 Hz using configuration of figure 5.23 and the source driving functions for speakers: (0.2412, -0.9762), (-0.4916, 0.3621), (-0.1323, -5.8970e-2), (-0.2586, -0.2061). top: theoretical, bottom: experimental.

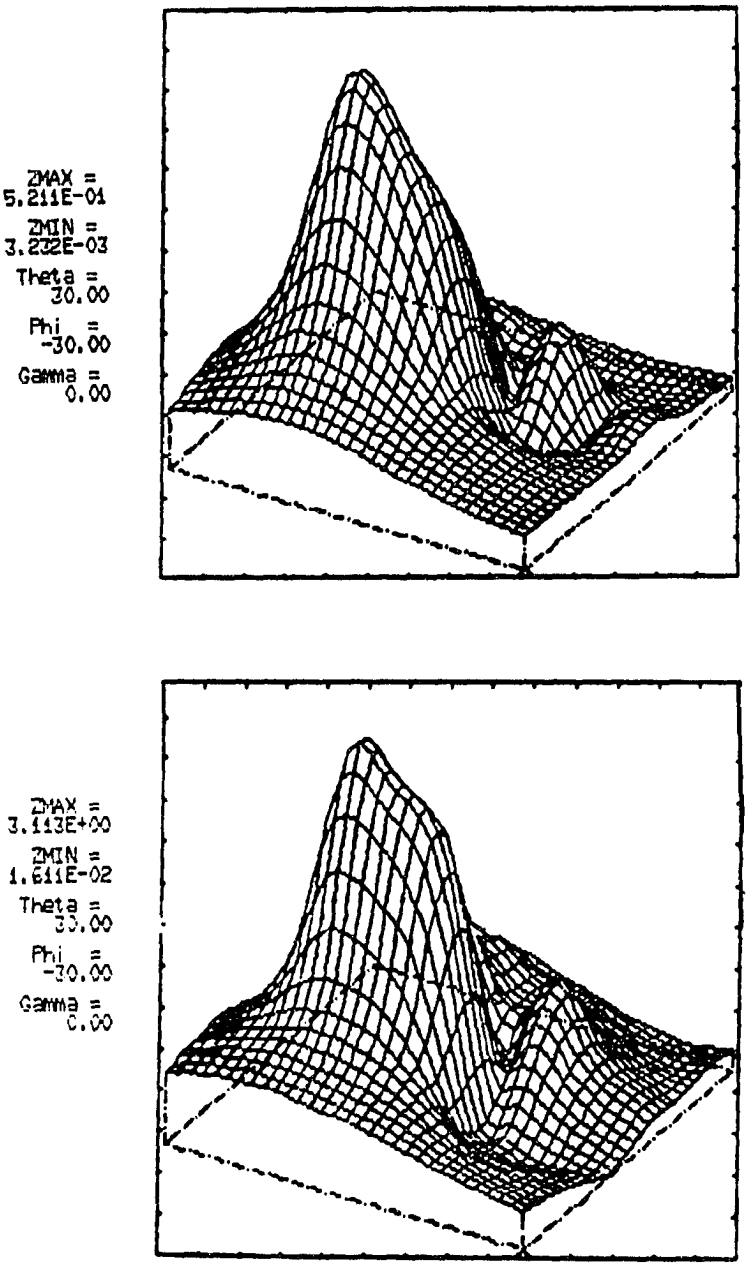


Figure 5.25: Theoretical and experimental noise cancellation (in Pascal) at 5 cm above plate at 150 Hz using configuration of Figure 5.23 and the source driving functions: plate: 2.3 volt, speakers: 0.274 volt $-76.12^{\circ}$, 0.162 volt $143.62^{\circ}$, 0.038 volt $204.03^{\circ}$, 0.087 volt $218.55^{\circ}$. top: theoretical, bottom: experimental.

measurement showed satisfactory agreement as presented in Figure 5.26. Therefore, it can be concluded that the experiments verified the numerical simulation satisfactorily. It should be noted that the noise reduction from the above measurements is not necessarily the best noise reduction one could achieve. A set of numerical simulations would have to be performed for different distribution patterns of the secondary sources in order to obtain the best noise reduction on the cancellation plane. However, the experiments showed that the best noise reduction is achievable when the locations of the secondary sources are identified from the data bank of the numerical simulations.

## 5.4 Discussion

The validity of the noise cancellation technique is verified experimentally in this chapter. Two different types of noise sources were chosen: a 6" speaker was used to simulate the noise source with uniform surface velocity while a ribbed aluminum plate driven by a shaker was used to simulate the noise source with nonuniform surface velocity distributions. Four 10" speakers were used as secondary sources to cancel the acoustic noise produced by the noise sources. The locations of the secondary sources were chosen arbitrarily because the purpose of the experiments was to verify the numerical simulation of the noise cancellation technique. Consequently, the validity of the noise cancellation technique would be justified as long as the results from the experiments showed satisfactory agreement with those from the numerical simulations. Therefore, the noise reduction level showed from the experiments was not necessarily the best noise reduction one could have achieved.

The theory for a baffled piston was used for the speaker sources no matter whether the speaker was used for primary or secondary sources. The surface veloc-

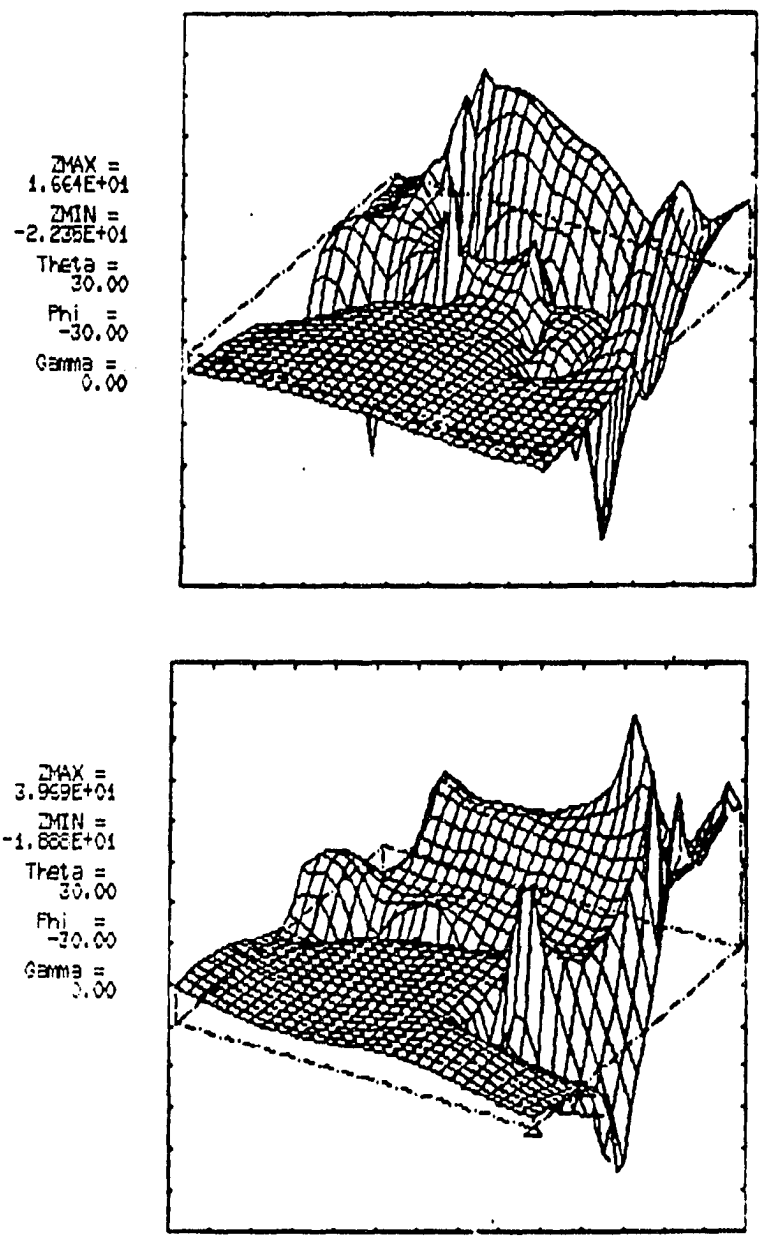


Figure 5.26: Theoretical and experimental noise reduction (in dB scale) 5 cm above the plate at 150 Hz using configuration of Figure 5.23 and the source driving functions: plate: 2.3 volt, speakers: 0.274 volt $-76.12^{\circ}$, 0.162 volt $143.62^{\circ}$, 0.038 volt $204.03^{\circ}$, 0.087 volt $218.55^{\circ}$. top: theoretical, bottom: experimental.

ity of the speaker was not directly measurable. Therefore, the equivalent function between the surface velocity of the speaker and the input voltage to the speaker was evaluated for each speaker source respectively. Consequently, the speaker sources could be controlled to give the desired acoustic field inside the anechoic chamber. The experiments were performed for three different frequencies: 100 Hz, 1000 Hz and 2000 Hz for the noise source with uniform surface velocity. However, it was found that the speaker sources displayed better results when lower frequencies were used. The speaker source behaved less similarly to the piston source when the excitation frequencies increased. Therefore, a few discrepancies could be identified from the results of noise cancellation at high frequencies. However, satisfactory results were displayed for all the frequencies performed in the experimental noise cancellation. The noise cancellation technique was applied to evaluate the excitation functions for the secondary sources. The excitation functions for the secondary sources were generated by Masscomp 5400 computer and supplied to the speakers through a multi-channel digital/analog converter. The experimental results showed that the acoustic pressure on the cancellation plane would be reduced in the least square sense due to the addition of the secondary sources.

On the other hand, it is impossible to derive the surface velocity of a ribbed plate analytically. Therefore, the surface velocity of the plate was measured directly by a laser vibrometer when the plate was used as the primary noise source. Four 10" speakers were located around half the plate to cancel the acoustic noise on a designated cancellation plane. The cancellation technique was applied such that the acoustic pressure on the cancellation plane would be reduced. The noise reduction level from the experimental measurement agreed well with the numerical simulation.

From the experimental results shown in this chapter, it is concluded that the noise cancellation technique performs well numerically and experimentally. The best noise reduction on any designated area can be achieved from the numerical data bank which was obtained from performing numerical simulations for various secondary sources configurations. The experimental results in this chapter guarantee the success of the numerical simulation. Consequently, the purpose of noise reduction in the designated area is accomplished.

# 6. CONCLUSION

## 6.1 Summary

The feasibility of active noise cancellation in a half-space was investigated by using the boundary element method. The work can be divided into three major sections. (I). The Helmholtz equation was converted into a boundary integral equation. The half-space Green's function bounded by a finite impedance plane was derived. The formulation was tested for many acoustic radiation cases. The numerical results were compared with either analytical solutions or experimental results to gauge the accuracy of the numerical simulations. It was found that the numerical simulations predicted the acoustic field inside the half space accurately with no more than 3 % of error for all performed test cases.

(II). Two methods, namely, iterative control and coupled equation methods, were proposed to achieve noise cancellation in designated areas when the acoustic field from the primary noise source in the half-space was identified. Four secondary sources were placed symmetrically around the primary source. The noise cancellation condition over a specified area within the half space was enforced in a least-square sense, and a system of linear equations is then solved to obtained the strengths of the secondary sources. One major difficulty in solving this system of equations was that the coefficient matrix was ill-conditioned. In this situation, the method of singular

value decomposition was successfully employed.

The practical application of the noise cancellation technique was also evaluated. The number and size of the secondary sources were determined in advance such that the boundary element formulation would not become nonlinear. The numerical simulations of noise cancellation using boundary element method were conducted for various configurations of secondary sources. The solution returned by the noise cancellation technique provided the excitation function for the secondary sources for each configuration. The acoustic field in the half space was calculated with the addition of the secondary sources driven by the evaluated excitation functions. Thus, the noise reduction patterns as well as the maximum noise reductions in the half space could be identified. A data bank of the noise reduction patterns and maximum noise reduction levels was constructed for various source configurations. Consequently, the noise cancellation in designated areas can be accomplished by referring to the data bank for arbitrary situations.

(III). The noise cancellation technique was verified experimentally by using two different types of primary noise sources. A primary noise source with uniform surface velocity was simulated by a 6" speaker where the theory for a baffled piston was applied. In addition, a ribbed aluminum rectangular plate driven by a shaker was used to simulate a primary noise source with nonuniform surface velocity. The primary noise sources mounted in a rigid baffle were placed inside an anechoic chamber in which the undesired acoustic noise was to be canceled. The acoustic pressure on the designated cancellation plane was measured by computer aided data acquisition system together with the 2-D scanning system before and after the addition of the secondary sources. Consequently, the noise reduction pattern as well as the maximum

noise attenuation could be evaluated. It is shown that the noise cancellation technique provided more than 30 dB noise reduction. Therefore, the capability of the noise cancellation technique is justified.

It should be noted that the results shown in this research indicated that the noise attenuation for low frequency was better than that of the high frequency. However, the noise attenuation for high frequency would have been better if a theory other than for a baffled piston was used for the secondary sources. In other words, the surface velocity of the secondary sources is not necessary to be uniformly distributed. As a matter of fact, the distribution of the surface velocity can be any arbitrary function which can describe the motion of the secondary sources at a particular frequency. That is the reason why the experimental noise attenuation for speaker sources was better than the numerical prediction for high frequencies. Nevertheless, the rapid phase change of the acoustic pressure for high frequency makes active noise control more difficult to achieve. It is also noted that the numerical evaluation in this research is linear. Consequently, the solution of the boundary element formulation is unique. It indicates that the excitation functions for secondary sources will change linearly without affecting the noise attenuation level when the boundary condition of the primary noise source changes linearly. Therefore, it is not necessary to re-evaluate the excitation functions of the secondary sources when the boundary condition of the primary noise source changes uniformly.

The investigation in this research of noise cancellation is based on single frequency analysis. The investigation of noise cancellation techniques for multi-frequency situations is also feasible. Nevertheless, the noise cancellation technique must be evaluated for each frequency respectively. The results are manipulated for each frequency

to provide noise attenuation for multi-frequency cases.

## 6.2 Future Development

Even though the noise cancellation technique is analytically applicable for a finite impedance plane, experiments involving a finite impedance plane have not been performed. Future researchers may provide the experimental verifications for those cases. In addition, the extension of the noise cancellation technique from a uniform impedance plane to a nonuniform impedance plane is also an interesting topic for further development.

The noise cancellation technique proposed in this research required a number of numerical simulations such that a reference data bank of the noise reduction patterns and noise attenuation levels could be determined for different source configurations. It was because the number, size and locations of secondary sources were determined in advance to avoid nonlinear formulation in using the boundary element method. Therefore, a number of numerical simulations for various source configuration were inevitable. However, a nonlinear boundary element formulation could be done to avoid time-consuming multiple numerical simulations. For instance, suppose N secondary sources are used to cancel the acoustic noise generated by the primary noise source in the case presented previously in this thesis. There will be 2N parameters regarding the locations of the secondary sources and N parameters for the boundary conditions of the secondary sources. The nonlinear boundary element formulation is set up with respect to both boundary integral equation and field equation to primary and secondary sources. The solver package is used to determine those unknown parameters such that the locations and the boundary conditions of the secondary

sources are known simultaneously from the returned solutions of the numerical simulation. Therefore, it is more user friendly for operators to apply the nonlinear boundary element formulation. The nonlinear formulation has been proven to be successful for two dimensional potential problems. However, the extension of a nonlinear boundary element formulation to three dimensional arbitrary sources needs further investigation.

Even though the nonlinear boundary formulation has advantages over the linear formulation, it may create some problems. The nonlinear boundary formulation has to iterate implicitly to obtain the source configuration of best noise cancellation. Therefore, high computation cost is anticipated for the nonlinear iterations. In addition, the solution returned by the nonlinear formulation may indicate overlap among source locations which causes problems in applying the noise cancellation technique. Furthermore, the solution from the nonlinear formulation may not be unique. It is realized that the noise attenuation in a designated area can be achieved by either strong sources far away from the designated area or weak sources near it. Therefore, it is expected that non-unique solutions will appear when a nonlinear boundary formulation is used. It is unable to evaluate which formulation is more advantageous at this point. Further investigations of nonlinear formulations are encouraged.

The noise cancellation technique is capable of attenuating the acoustic noise generated by the primary noise source even when the boundary condition of the noise source changes linearly. However, the technique will be too slow to catch up with the rapid change of the boundary condition of the primary noise source when a large system is involved. Therefore, the noise cancellation technique has to incorporate with an adaptive noise control technique in order to cancel the acoustic

noise adaptively. It will be an attractive topic for the future researchers to couple those two techniques together.

# BIBLIOGRAPHY

[1] Lueg, P. *Process of Silencing Sound Oscillations.* U. S. Patent # 2,043,416, 1936.

[2] Baker, B. B. and Copson, E. T. *The Mathematical Theory of Huygen's Principle.* Oxford University Press, 1939.

[3] Munjal, M. L. and Eriksson, L. J. "An Analytical One-Dimensional, Standing-Wave Model of a Linear Active Noise Control System in a Duct." *Journal of the Acoustic Society of America* 84 (1988): 1086-1093.

[4] Tichy, J., Warnaka, G. E. and Poole, L. A. "A Study of Active Control of Noise in Ducts." *Journal of Vibration, Acoustics, Stress and Reliability in Design* 106 (1984): 399-404.

[5] Eghtesadi, Kh., Hong, W. K. W. and Leventhall, H. G. "Energy Conservation by Active Noise Attenuation in Ducts." *Noise Control Engineering Journal* 112 (1986): 90-94.

[6] Maxwell, R. G., Sjosten, P. and Lindqvist, E. A. "Active Noise Control of Pure Tunes in Ducts for Non-Plane Waves: A Case Study." *Inter-Noise* 89 (1989): 447-450.

[7] Burgess, J. C. "Active Adaptive Sound Control in a Duct: A Computer Simulation." *Journal of Acoustical Society of America* 70 (1981): 715-726.

[8] Snyder, S. D. and Hansen, C. H. "Active Noise Control in Ducts: Some Physical Insights." *Journal of Acoustical Society of America* 86 (1989): 184-194.

[9] Silcox, R. J., Lester, H. C. and Abler, S. B. "Evaluation of Active Noise Control in a Cylindrical Shell." *Journal of Vibration, Acoustics, Stress and Reliability in Design* 111 (1989): 337-342.

[10] Dorling, C. M., Eatwell, G. P., Hutchins, S. W., Ross, C. F. and Sutcliffe, S. G. C. "A Demonstration of Active Noise Reduction in an Aircraft Cabin." *Journal of Sound and Vibration* 128 (1989): 358-360.

[11] Salikuddin, M. and Ahuja K. K. "Application of Localized Active Control to Reduce Propeller Noise Transmitted Through Fuselage Surface." *Journal of Sound and Vibration* 133 (1989): 467-481.

[12] Koopmann, G. H., Neise, W. and Chen, W. "Active Noise Control to Reduce the Blade Tone Noise of Centrifugal Fans." *Journal of Vibration, Acoustics, Stress and Reliability in Design* 110 (1988): 377-383.

[13] Angevine, O. L., Gupta, P. K. and Rushden, F. A. "Active Acoustic Absorbers for Low-Frequency Hum." 99th Meeting of the Acoustic Society of America, University Park, Pennsylvania, 1980.

[14] Elliott, S. J. and Nelson, P. A. "An Adaptive Algorithm for Multichannel Active Control." *Proceedings of the Institute of Acoustics* 8 (1986): 135-147.

[15] Elliott, S. J., Stothers, I. M. and Nelson, P. A. "A Multiple Error LMS Algorithm and its Application to the Active Control of Sound and Vibration." *IEEE Transactions on Acoustics Speech and Signal Processing* 186 (1987): 1124-1127.

[16] White, A. D. and Cooper, D. G. "An Adaptive Controller for Multivariable Active Noise Control." *Applied Acoustics* 17 (1984): 99-109.

[17] Ross, C. F. "Application of Digital Filtering to Active Control of Sound." *Acoustica* 51 (1982): 135-140.

[18] Stevens, J. C. and Ahuja, K. K. "Recent Advances in Active Noise Control." *Journal of American Institute of Aeronautics and Astronautics* 29 (1991): 1058-1067.

[19] Pierce, A. D. *Acoustics: An Introduction to Its Physical Principles and Applications.* New York: McGraw-Hill Book Company, 1981.

[20] Bathe, K. *Finite Element Procedures in Engineering Analysis.* New Jersey: Prentice-Hall Inc., 1982.

[21] Ingard, U. "On the Reflection of a Spherical Sound Wave from an Infinite Baffle." *Journal of Acoustical Society of America* 23 (1951): 329-335.

[22] Kinsler, L. E., Frey, A. R., Coppens, A. B. and Sanders, J. V. *Fundamentals of Acoustics.* New York: J. Wiley & Sons, 1982.

[23] Bennink, D. D. "Modeling of Ultrasonic Scattering Experiments with Applications to System and Transducer Characterization." *Ph. D. Dissertation.* Iowa State University, Ames, Iowa, 1989.

[24] Dongarra, J. J., Moler, C. B., Bunch, J. R. and Steward, G. W. *Linpack: Users' Guide.* New York: Society for Industrial and Applied Mathematics, 1982.

[25] Johnson, L. W. and Riess, R. D. *Numerical Analysis.* Massachusetts: Addison-Wesley Publishing Company, 1982.

[26] Press, W. H., Flannery, B. P., Teukolsky, S. A. and Vetterling, W. T. *Numerical Recipes.* Cambridge: Cambridge University Press, 1986.

# APPENDIX A. INTEGRATION FOR WEAKLY SINGULAR KERNEL

Consider the integration with kernel $K(r(x,\zeta))$, that is

$$\int_S K(r(x,\zeta))\, dS(\zeta) \tag{A.1}$$

If the kernel $K(r(x,\zeta))$ is weakly singular, that is, of order $\frac{1}{r}$, the integration has to be modified.

For the quadrilateral elements used in this research, there are either 8 node quadralaterals or 6 node triangles in each element as shown in Figure A.1. The collocation point x is either a corner node or a mid-side node of the element. For a corner node, the square is divided into two triangles diagonally with the distance $r(x,\zeta)$ expressed as $r(\rho,\theta)$ in the local polar coordinates. The integral $\int_S K(r(x,\zeta))\, dS(\zeta)$ over the element is expressed into integrals over the two sub-triangles.

$$\begin{aligned}
&\int_S K(r(x,\zeta))\, dS(\zeta) \\
&= \int_S K(r(x,\zeta))\, J(\zeta_1,\zeta_2)\, d\zeta_1 d\zeta_2 \\
&= \int_{-1}^{1}\int_{-1}^{1} F(x,\zeta_1,\zeta_2)\, d\zeta_1 d\zeta_2 \\
&= \sum_{\triangle=1,2} \int_0^{\frac{\pi}{4}} \left\{ \int_0^{2sec\theta} F(x,\rho,\theta)\, \rho d\rho \right\} d\theta \\
&= \int_0^{\frac{\pi}{4}} \tilde{F}(x,\theta)\, d\theta
\end{aligned} \tag{A.2}$$

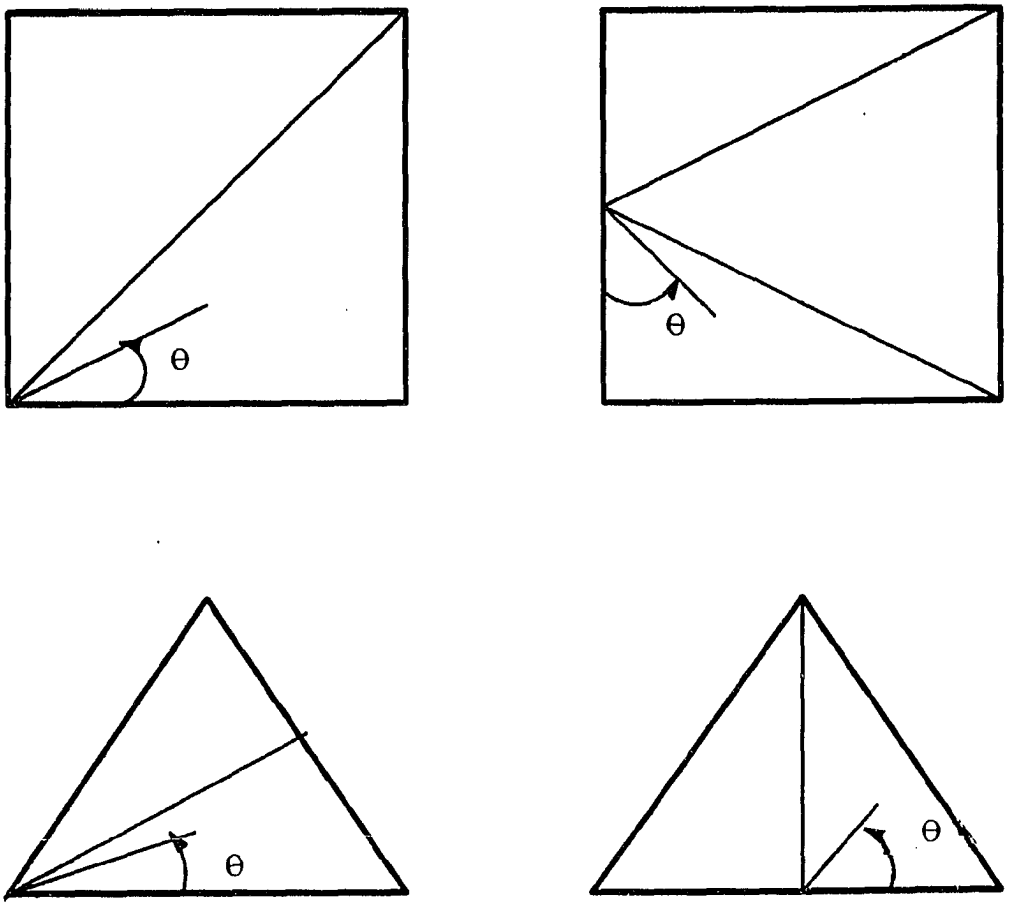


Figure A.1: The transformation to local polar coordinates for quadrilateral elements

The element area is now $\rho d\rho d\theta$ where $\rho$ is of order r as r approaches zero. It is known that the integration under this transformation is non-singular.

If the collocation point x is a mid-side node of a quadrature, the mapped square is divided into three triangles. The same procedures are taken to transform the singular kernel into a non-singular one.

If the collocation point x is either a corner node or a mid-side node of a triangular element, the triangular element is divided into two sub-triangles and the same procedures described above are applied again to each sub-triangle. Consequently, the singular kernel of the integration becomes a non-singular kernel when the transformation to local polar coordinates is done.

## APPENDIX B. PRESSURE-RELEASED PISTON

The on-axis acoustic pressure for a pressure released piston is evaluated as follows:

$$\phi(Q) = \int_S \left[ G(P,Q) \frac{\partial \phi(P)}{\partial n} - \phi(P) \frac{\partial G(P,Q)}{\partial n} \right] dS \tag{B.1}$$

where $G(P,Q) = \frac{e^{ikr_1}}{4\pi r_1} - \frac{e^{ikr_2}}{4\pi r_2}$

and $\frac{\partial G(P,Q)}{\partial n} = \frac{-1+ikr_1}{r_1^2} e^{ikr_1} \frac{z_s - z}{r_1} - \frac{-1+ikr_2}{r_2^2} e^{ikr_2} \frac{z_s + z}{r_2}$

On the surface of the piston, one has $z_s = 0$ and $r_1 = r_2 = r$ which leads to

$$G(P,Q)|_{z_s=0} = \frac{e^{ikr}}{4\pi r} - \frac{e^{ikr}}{4\pi r} = 0$$

and

$$\frac{\partial G(P,Q)}{\partial n}|_{z_s=0} = -2 \frac{-1+ikr}{r} e^{ikr} \frac{z}{r}$$

Therefore, equation (B.1) becomes

$$\phi(Q) = 2z \int_S \phi(P) \frac{-1+ikr}{r} \frac{e^{ikr}}{r^2} dS \tag{B.2}$$

Let $\phi(P) = \phi = constant$, then the on axis pressure is

$$\phi(Q) = -2z\phi \int_S \frac{1-ikr}{r^3} e^{ikr} dS \tag{B.3}$$

Consider the geometry shown in Figure B.1 where $r = \sqrt{r'^2 + \sigma^2}$ and $dS = 2\pi\sigma d\sigma$, the above equation becomes

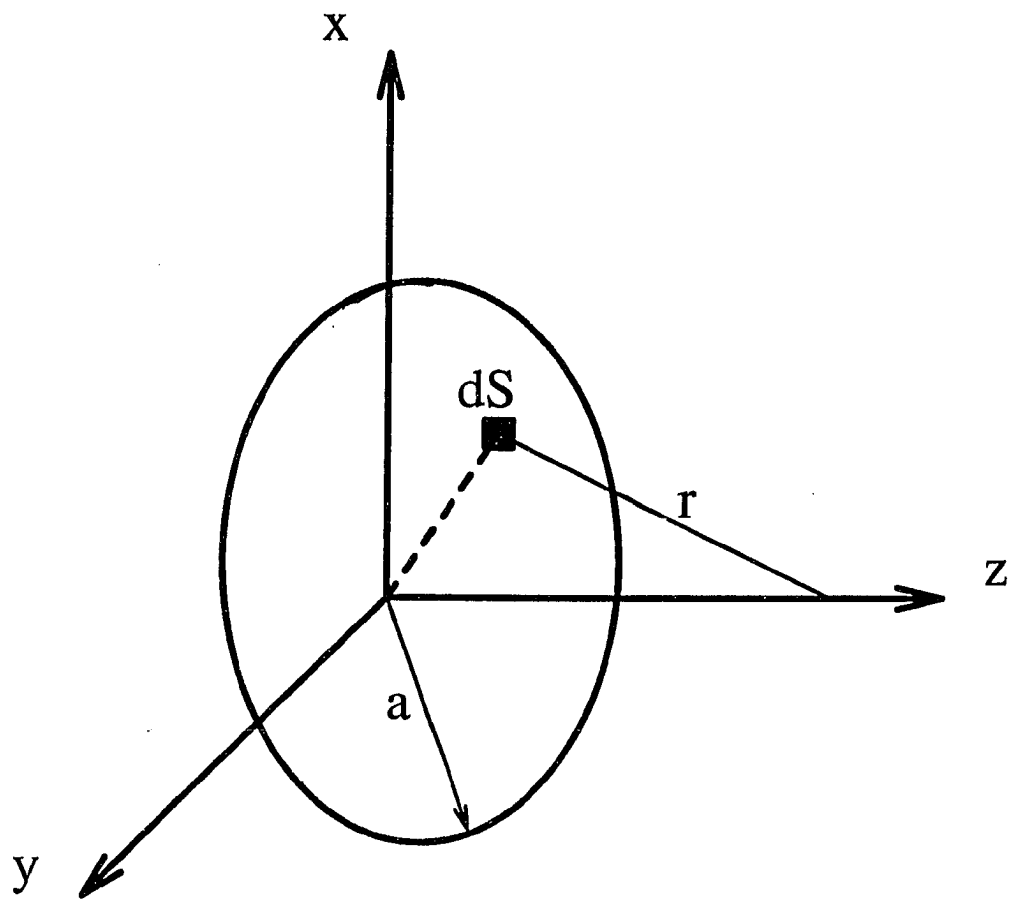


Figure B.1: Geometry of pressure-released piston

$$\begin{aligned}
\phi(Q) &= -2z\phi \int_S \frac{1-ik\sqrt{\acute{r}^2+\sigma^2}}{\left(\acute{r}^2+\sigma^2\right)^{\frac{3}{2}}} e^{ik\sqrt{\acute{r}^2+\sigma^2}} dS \\
&= -2z\phi \int_0^a \frac{1-ik\sqrt{\acute{r}^2+\sigma^2}}{\left(\acute{r}^2+\sigma^2\right)^{\frac{3}{2}}} e^{ik\sqrt{\acute{r}^2+\sigma^2}} 2\pi\sigma d\sigma \\
&= -2\pi z\phi \int_0^{a^2} \frac{1-ik\sqrt{\acute{r}^2+\sigma^2}}{\left(\acute{r}^2+\sigma^2\right)^{\frac{3}{2}}} e^{ik\sqrt{\acute{r}^2+\sigma^2}} d\sigma^2 \\
&= -2\pi z\phi \left[ \int_0^{a^2} \frac{e^{ik\sqrt{\acute{r}^2+\sigma^2}}}{\left(\acute{r}^2+\sigma^2\right)^{\frac{3}{2}}} d\sigma^2 - ik \int_0^{a^2} \frac{e^{ik\sqrt{\acute{r}^2+\sigma^2}}}{\acute{r}^2+\sigma^2} d\sigma^2 \right] \qquad \text{(B.4)}
\end{aligned}$$

The two integrals in above equation are now considered individually. First, consider

$$\int_0^{a^2} \frac{e^{ik\sqrt{\acute{r}^2+\sigma^2}}}{\left(\acute{r}^2+\sigma^2\right)^{\frac{3}{2}}} d\sigma^2 = \int_{\acute{r}^2}^{\acute{r}^2+a^2} \frac{e^{ik\sqrt{zeta}}}{\zeta^{\frac{3}{2}}} d\zeta$$

where $\zeta = \acute{r}^2 + \sigma^2$

Integration by parts with the substitutions of $du = \frac{d\zeta}{\zeta^{\frac{3}{2}}}, u = -2\zeta^{\frac{-1}{2}}, v = e^{ik\sqrt{\zeta}}$ and $dv = ike^{ik\sqrt{\zeta}} \frac{1}{2\sqrt{\zeta}}$, Then,

$$\begin{aligned}
&\int_{\acute{r}^2}^{\acute{r}^2+a^2} \frac{e^{ik\sqrt{\zeta}}}{\zeta^{\frac{3}{2}}} d\zeta \\
&= \frac{-2}{\sqrt{\zeta}} e^{ik\sqrt{\zeta}} \Big|_{\acute{r}^2}^{\acute{r}^2+a^2} - \int_{\acute{r}^2}^{\acute{r}^2+a^2} \frac{-2}{\sqrt{\zeta}} ike^{ik\sqrt{\zeta}} \frac{1}{2\sqrt{\zeta}} d\zeta \\
&= \frac{-2}{\sqrt{\acute{r}^2+a^2}} e^{ik\sqrt{\acute{r}^2+a^2}} - \left( \frac{-2}{\acute{r}} e^{ik\acute{r}} \right) + ik \int_{\acute{r}^2}^{\acute{r}^2+a^2} \frac{e^{ik\sqrt{\zeta}}}{\zeta} d\zeta \\
&= -2 \left( \frac{e^{ik\sqrt{\acute{r}^2+a^2}}}{\sqrt{\acute{r}^2+a^2}} - \frac{e^{ik\acute{r}}}{\acute{r}} \right) + ik \int_0^{a^2} \frac{e^{ik\sqrt{\acute{r}^2+\sigma^2}}}{\sqrt{\acute{r}^2+\sigma^2}} d\sigma^2 \qquad \text{(B.5)}
\end{aligned}$$

Consequently, the on-axis acoustic pressure of the pressured-released piston is expressed as

$$
\begin{aligned}
&\phi(Q) \\
&= -2\pi z\phi \left[ -2 \left( \frac{e^{ik\sqrt{\acute{r}^2+a^2}}}{\sqrt{\acute{r}^2+a^2}} - \frac{e^{ik\acute{r}}}{\acute{r}} \right) + ik \int_0^{a^2} \frac{e^{ik\sqrt{\acute{r}^2+\sigma^2}}}{\sqrt{\acute{r}^2+\sigma^2}} d\sigma^2 \right. \\
&\left. -ik \int_0^{a^2} \frac{e^{ik\sqrt{\acute{r}^2+\sigma^2}}}{\sqrt{\acute{r}^2+\sigma^2}} d\sigma^2 \right] \\
&= 4\pi z\phi \left[ \frac{e^{ik\sqrt{\acute{r}^2+a^2}}}{\sqrt{\acute{r}^2+a^2}} - \frac{e^{ik\acute{r}}}{\acute{r}} \right]
\end{aligned}
\tag{B.6}
$$